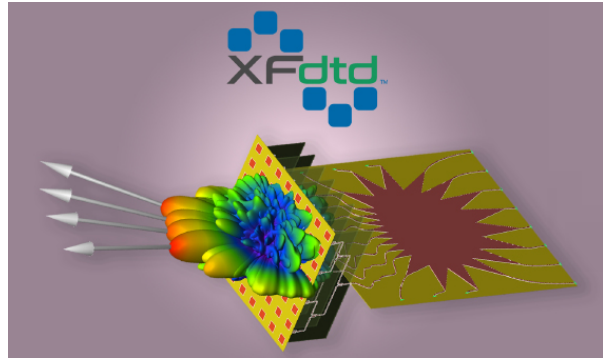


## Using EM Simulation for 5G Device Design and Network Planning

*A Collection of Application Examples Featuring Remcom's EM Simulation Software*

### Introduction

5G is pushing the boundaries of wireless communications and wireless device design. New innovations are needed in order to accommodate increased requirements for Enhanced Mobile Broadband, Massive Machine-Type Communications, and Ultra-Reliable, Low Latency Communications.

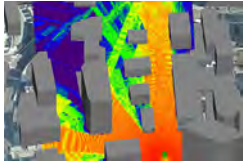


Remcom's simulation products provide a complete solution, from system and antenna design, through performance assessment in realistic, simulated environments, and planning for deployment in 5G networks. Our mission is to provide accurate solutions, optimized for performance to help our customers reliably predict how their systems will behave in the real world. Through active research and development, we have been developing new products and adding capabilities to stay at the forefront of modeling and simulation technology for 5G and other advances in wireless communications.

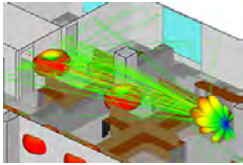
We hope you enjoy this collection of application examples written by Remcom's engineers. They demonstrate how Remcom's software can be used to solve challenges related to 5G and MIMO use cases such as MIMO and array design, 5G urban small cells, fixed wireless access, indoor WiFi and mmWave, beamforming, and more.



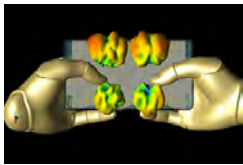
## Table of Contents



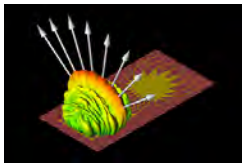
**Example 1: 5G Massive MIMO Outdoor Communications Analysis**



**Example 2: mmWave Channel Modeling with Diffuse Scattering in an Office Environment**



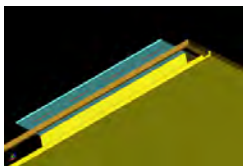
**Example 3: Simulation of MIMO Handset Antenna Array Performance with Varying Hand Positions**



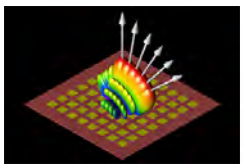
**Example 4: EM Simulation of 28 GHz Series-Fed Patch Antenna Array for 5G**



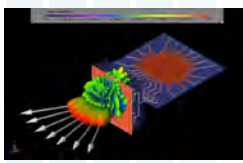
**Example 5: Throughput of a 5G New Radio FD-MIMO System in an Urban Area Using Custom Beamforming**



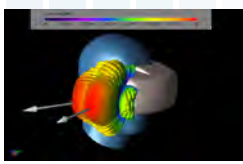
**Example 6: Combined 5G/4G Antenna Analysis in a Smartphone using EM Simulation**



**Example 7: Beamforming for an 8x8 Planar Phased Patch Antenna Array for 5G at 28 GHz**



**Example 8: Design and Simulation of 28 GHz Beamforming System and Antenna Array for 5G Network Base Stations**



**Example 9: 5G Antenna Array Simulation for mmWave Wireless Virtual Reality Headsets**

## Example 1: 5G Massive MIMO Outdoor Communications Analysis

*Summary: In this example the signal transmission between a massive MIMO base station and a mobile device located in downtown Rosslyn is analyzed using Wireless InSite's MIMO capability.*

To demonstrate the concept of MIMO simulation assessment, Wireless InSite's MIMO capability has been used to set up a small cell scenario in a dense urban environment in Rosslyn, Virginia (Figure 1). The base station is positioned atop a post on a median at a major intersection at a height of 10 meters above street level. For the purpose of comparison, the base station has been defined with two alternative configurations: (1) a single dipole antenna, and (2) a large MIMO antenna. Both use a carrier frequency of 28 GHz.

The imported city model and the terrain contain a total of approximately 3,800 faces. The buildings and terrain are assigned concrete material properties with conductivity of 0.484 S/m and permittivity of 5.31. Figure 2 shows a close-up of the massive MIMO antenna, defined as an 8x8 cross-polarized dipole array. The gain pattern of the first element is displayed in the array view. A mobile device is defined to move along a route through the city and is shown approaching the base station location from the west, and then turning to move away from it to the north.



*Figure 1: Rosslyn 3D building and terrain data are set up for SISO and MIMO analysis within Wireless InSite.*

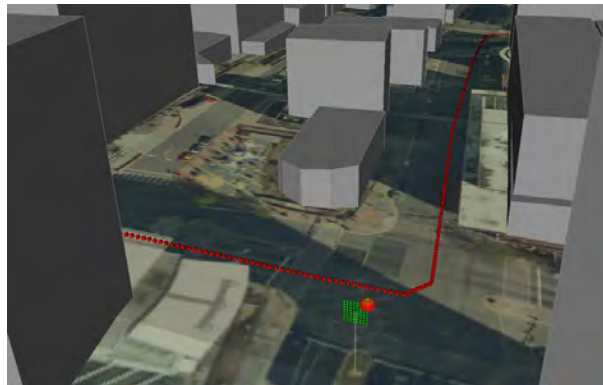


*Figure 2: The 128-element Massive MIMO array is located on a Tx point several feet above the ground with a moving Rx set in the downtown area.*

## Example 1: 5G Massive MIMO Outdoor Communications Analysis

Wireless InSite MIMO contains an array builder which allows users to design an n-element sized MIMO array. This tool also gives users control over individual elements of the array such as positioning, antenna pattern, and rotation. Figure 3 shows the 128-element array within the array builder. For simplicity, this array has been built with dipole antennas, placed at half-wavelength spacing, and arranged with both vertically-polarized and horizontally-polarized elements placed at each of the 64 positions shown. However, it should be noted that the software can handle many different types of analytical patterns and can also utilize imported patterns generated by high-fidelity array simulations from a full-wave solver, such as Remcom's XFDTD.

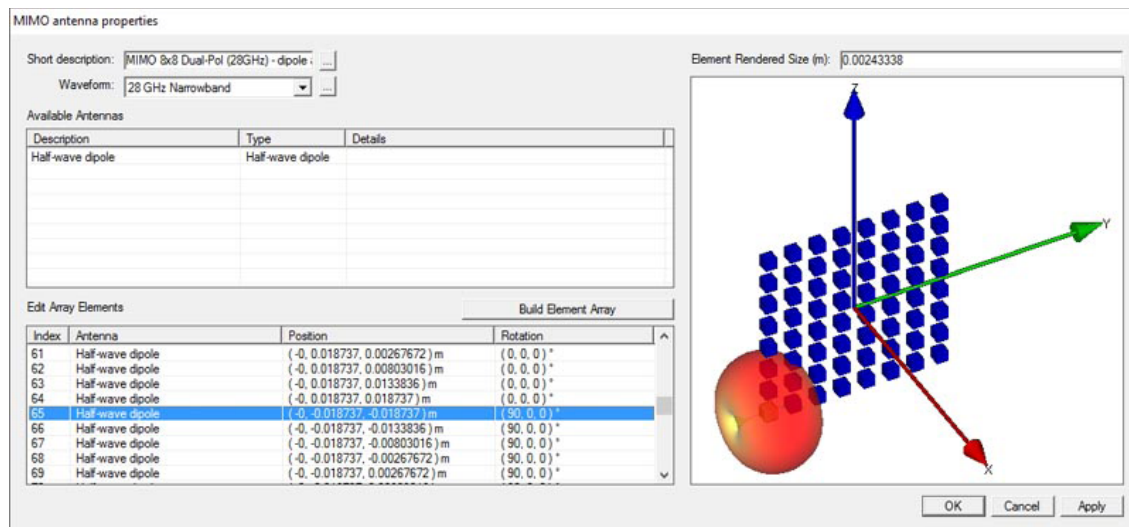


Figure 3: The 128-element Massive MIMO array was built in Wireless InSite's powerful array builder.

Wireless InSite's study area properties allows users to configure and control various aspects of the physics and ray-tracing calculations. Figure 4 shows the study area setup dialogue for the massive MIMO simulation. The study area is defined to use Wireless InSite's GPU-accelerated X3D ray model, with ray-tracing defined to include propagation paths with up to six reflections and one diffraction, omitting transmissions to limit calculations to the outdoors.

Simulations using the single antenna and the MIMO antenna are then performed. Wireless InSite provides user-requested outputs such as received power, propagation paths, time of arrival/departure, etc.

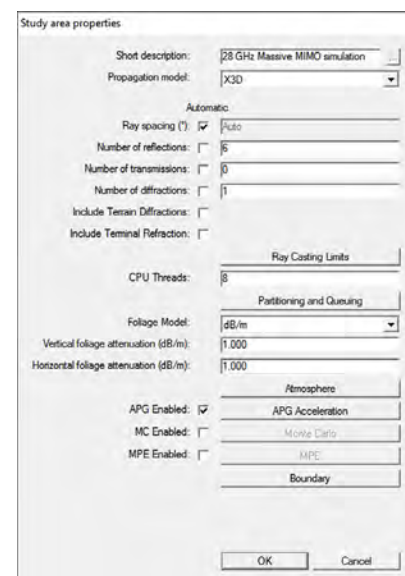


Figure 4: The Study Area Properties window gives the user control over which propagation model to run and the number of interactions.

## Example 1: 5G Massive MIMO Outdoor Communications Analysis

A typical result from the analysis of a single transmitting antenna is the power received by a mobile device, either in the form of a coverage map over an area or displayed as a function of distance along a route. Figure 5 provides a field map showing the coverage in the vicinity of the base station. Figure 6 shows a plot of the power received by the mobile device along its route (shown in red in views of the scene). As shown in the second figure, the power increases along the route as the mobile device approaches the base station and falls off as it moves away, dropping dramatically when it turns the corner and goes out of line-of-sight. Rapid fading in the received power along the route is due to multipath interactions (reflections and diffractions) with buildings.

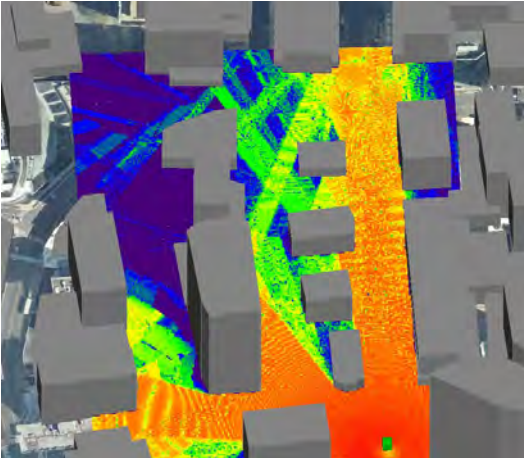


Figure 5: Field map showing the coverage over an area of the scene.

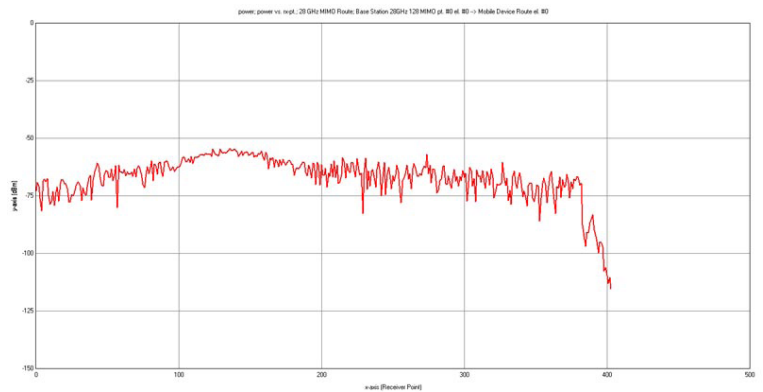


Figure 6: Power received by mobile device along route from base station with single antenna.

Another output that is relevant for both single antennas and MIMO systems is the complex impulse response, which is a measure of multipath. The complex impulse response measures the power of arriving multipath signals as a function of either their time of arrival or phase. Figure 7 shows the top 25 propagation paths between the base station and mobile device at a point approximately 240 meters along its route. The complex impulse response at this location for the single antenna base station is shown in Figure 8.

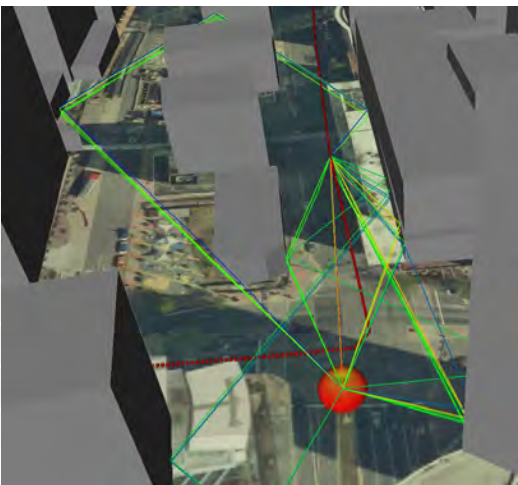


Figure 7: Top 25 propagation paths from base station to mobile device at one point along its route.

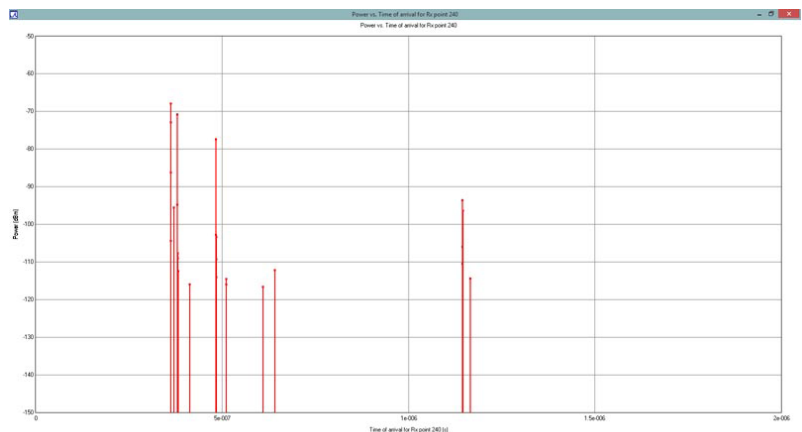


Figure 8: Complex Impulse Response for mobile device at position shown above.

## Example 1: 5G Massive MIMO Outdoor Communications Analysis

Wireless InSite MIMO allows users to write out H-matrix, Complex Impulse Response, and Delay Spread using a channel data results browser shown in Figure 9. The image shows settings for plotting received power as a function of receiver number for the Rosslyn MIMO scenario for all combinations of transmitting and receiving antenna elements in the MIMO system. Figure 10 shows the received power at the mobile device along its route, overlaying results for all transmitter elements.

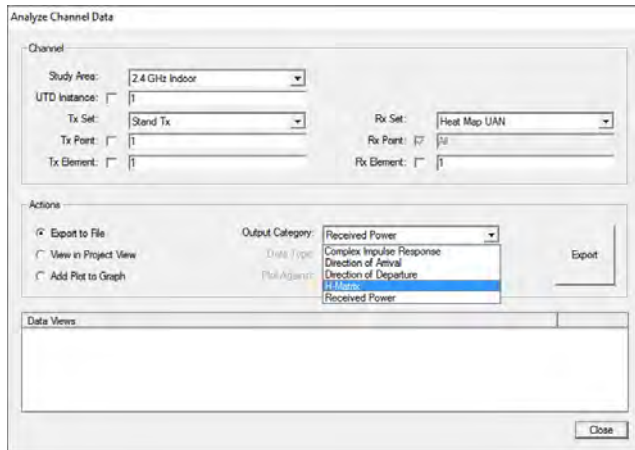


Figure 9: The “Analyze Channel Data” results browser was created for the Wireless InSite MIMO module. This browser allows users to output H-matrix, Complex Impulse Response, Delay Spread and Received Power.

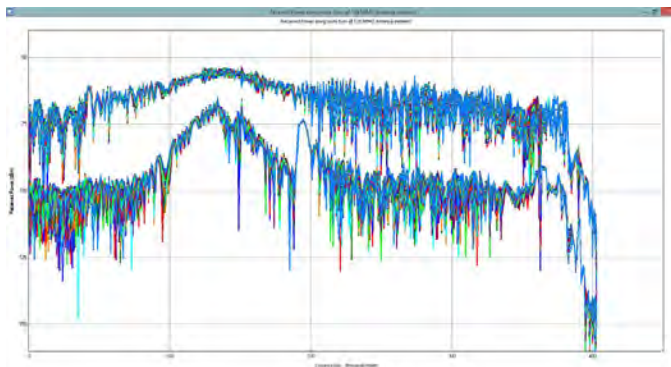


Figure 10: Power received by mobile device along route from all 128 transmitting elements of MIMO base station.

One of the key output results from a MIMO simulation is the complex channel matrix, or H-matrix. The H-matrix encodes the multipath propagation characteristics from every transmitter element to every receiver element and is commonly used in beamforming, channel capacity, and other MIMO system-level analyses. Wireless InSite’s channel data results browser allows a user to export the H-matrix to a .csv file, where additional post-processing analysis can determine how channel multipath may impact the performance of the MIMO system.

[Click to see the web version of this example](#)

[Request project files for this example](#)

Table of Contents

## Example 2: mmWave Channel Modeling with Diffuse Scattering

*Summary: The millimeter wave frequencies being planned for 5G systems pose challenges for channel modeling. At these frequencies, surface roughness impacts wave propagation, causing scatter in non-specular directions that can have a large effect on received signal strength and polarization. To accurately predict channel characteristics for millimeter wave frequencies, propagation modeling must account for diffuse scattering effects. Wireless InSite's diffuse scattering capability is based on Degli-Esposti's work.*

The millimeter wave frequencies being planned for 5G systems pose challenges for channel modeling. At these frequencies, surface roughness impacts wave propagation, causing scatter in non-specular directions that can have a large effect on received signal strength and polarization. To accurately predict channel characteristics for millimeter wave frequencies, propagation modeling must account for diffuse scattering effects. Wireless InSite's diffuse scattering capability is based on Degli-Esposti's work. It includes three models that provide alternative scattering patterns and account for partial cross-polarization of the scattered fields. It also allows the user to optionally sum scattered contributions assuming coherent phase, so that phase effects over closely-spaced antennas (e.g., MIMO) can be accounted for.

This example uses Wireless InSite's diffuse scattering capability to perform simulations of an indoor wireless network and compares to some measurements detailed in [1]. The scenario, shown in Figure 1, is a portion of the 9th floor of an office building, which includes walls, pillars, windows, cubicle partitions, desks, and cabinets. The transmitter is located at ceiling level in a large, open room. The receivers are located at several points in the room and down the hallway.



Figure 1a

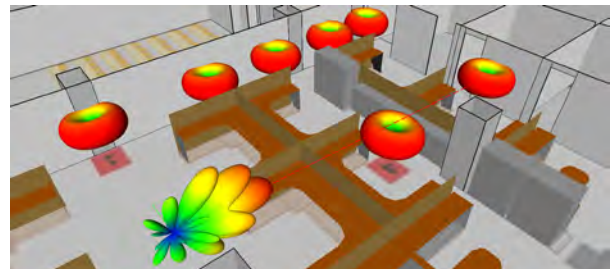


Figure 1b

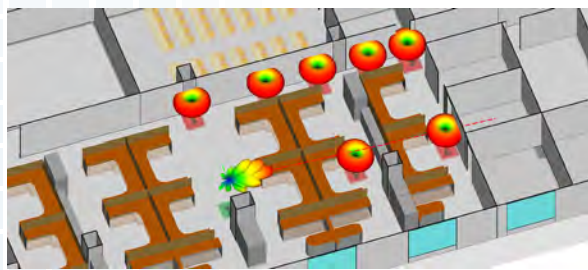


Figure 1c

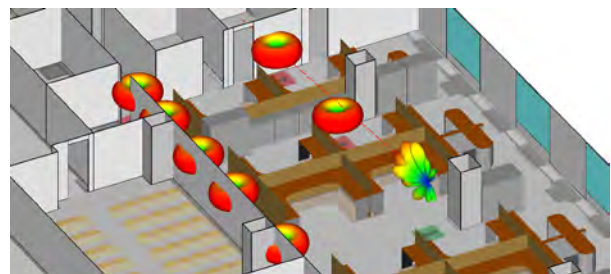


Figure 1d

Figure 1: Various positions of transmitting horn antenna aligned with various receiver points

## Example 2: mmWave Channel Modeling with Diffuse Scattering

We focus on the measurements done at 73.5 GHz in the large room nearest the transmitter. The transmitter is modeled using a horn antenna pattern with  $15^\circ$  beam width and 20 dBi gain that is rotated to point at each receiver location. The receivers are mounted 1.5m above the floor in several locations, both within line-of-sight, and beyond line-of-sight from the transmitter. Each receiver is modeled with both a vertical and horizontal  $45^\circ$  beamwidth Omnidirectional antenna.

The diffuse scattering effects of the floor, drywall walls, pillars, filing cabinets, cubicle partitions, and desk supports are modeled using the directive model described in [4, 5, 6]. With this model, scattered energy is centered around the specular reflection angle with no back scatter. The Scattering Factor,  $S$ , represents the fraction of the incident electric field that is scattered diffusely. Valid values range from 0, no diffuse scattering, to 1, all diffuse scattering. The cross-polarization fraction  $K_{\text{xpol}}$  represents the fraction of diffuse power that becomes cross-polarized relative to the incident ray's polarization. Valid values range from 0 to 0.5. Lastly, the parameter  $\alpha$  controls the shape of the forward-scattering lobe. Valid values are integers between 1 and 10, with 10 being the narrowest. Figure 2 shows how energy is scattered when using the directive diffuse scattering model.

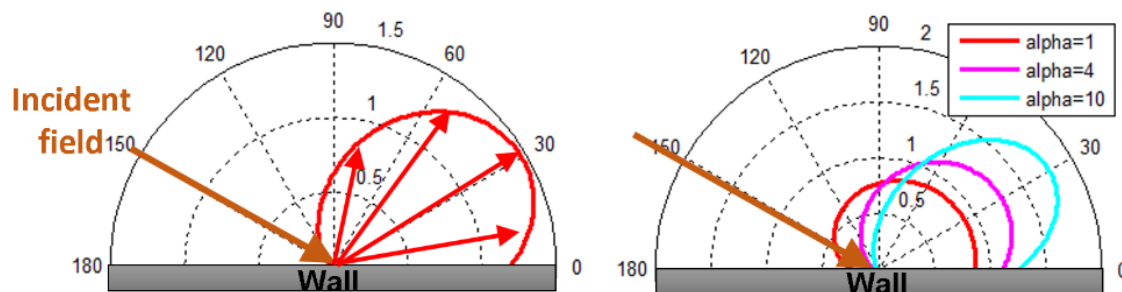


Figure 2: Directive diffuse scattering model

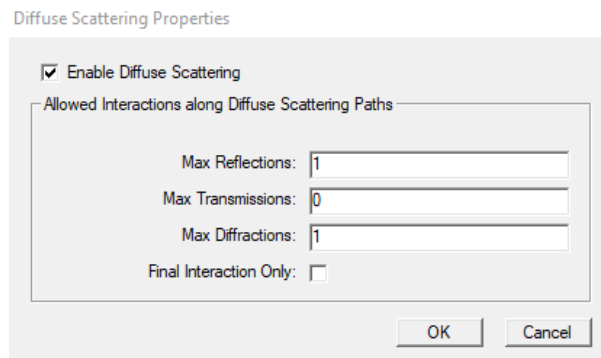
Recommended values for the Scattering Factor at 60 GHz range from 0.1 to 0.5 [2]. Table 1 shows the Scattering Factor used for each of the diffuse scatter enabled materials in this example. Material properties for the drywall, concrete (floor, ceiling and pillars), glass windows, and desktops are taken from [2]. The cubicle partitions are assumed to be Fiber Reinforced Plastic (FRP) honeycomb core, and their properties are extrapolated from [3]. The filing cabinets and other metal structures are assumed to have handles, beveled edges, and other structures that can contribute to scattering. Cross-pol fraction and  $\alpha$  were left at the Wireless InSite default values of 0.4 and 4 respectively.

## Example 2: mmWave Channel Modeling with Diffuse Scattering

Material	Scattering Factor
Concrete	0.4
Drywall (3-layered drywall)	0.2
Support column (PEC beam with drywall exterior)	0.2
Cabinets, desk supports and filing cabinets (metal)	0.2
Partitions (FRP honeycomb core)	0.5

Table 1: Scattering Factor for various building materials

Two study areas are created to allow for easy comparison of non-diffuse scatter results and results with diffuse scattering. For the non-diffuse scattering interactions the settings are 3 reflections, 1 transmission and 1 diffraction. For the diffuse scattered paths, we allow 1 reflection, no transmissions and 1 diffraction. The ability to allow interactions along the diffuse scattering paths is unique to Wireless InSite.



Diffuse Scattering Properties window in the X3D study area

To replicate the measurement procedures described in [1], it is necessary to align the transmitter's antenna with the intended receiver, and consider only the intended, paired channels. This was done by creating seven transmitters at the location for transmitter 1, each with the horn antenna rotated to align with the intended receiver location. Figure 3 shows the antenna alignment for receiver locations 1, 4 and 5.

The aligned pairs are most efficiently run by selecting and making active; for example, TX1 to RX1, RX1 and RX1-xpol, running the simulation, then moving on to TX1 to RX2, RX2, and RX2-xpol, etc. Running the simulations in this manner requires a little over a minute for each specular case, and about four minutes for each diffuse scatter simulation.

## Example 2: mmWave Channel Modeling with Diffuse Scattering

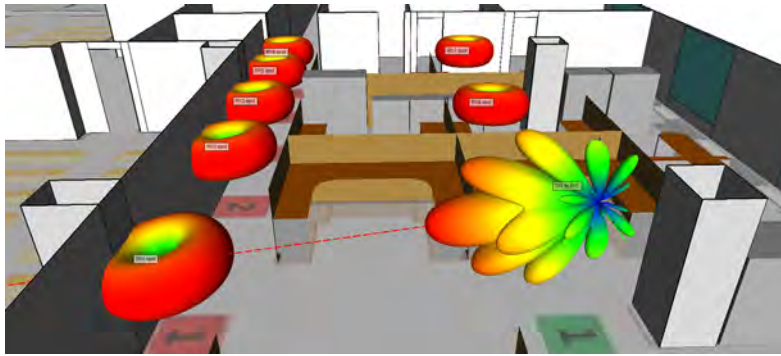


Figure 3a

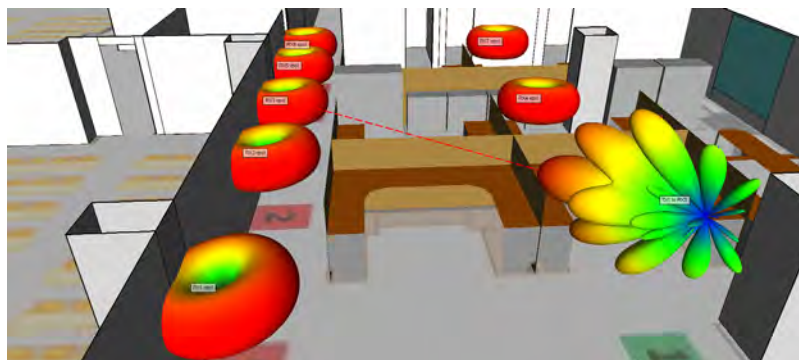


Figure 3b

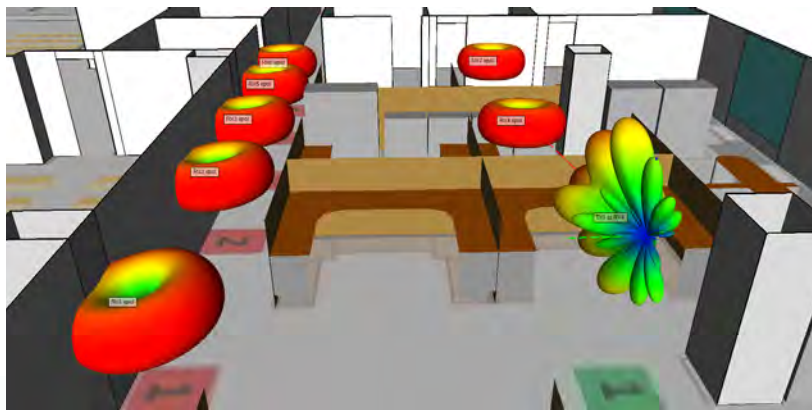


Figure 3c

Figure 3: Various positions of transmitting horn antenna aligned with various receiver points

Figures [4a] and [4b] show the top 100 paths between the matched TX- RX pair for the receiver location 7. The red paths are the strongest, with weaker paths rendered in greens and blues. The specular paths in Figure [4a] show the highest power paths are typically within the main beam, with many lower powered reflections and transmissions off and through the walls. Figure [4b] includes paths with diffuse scattering interactions. One can see the wide spread of paths scattering backwards off the wall behind the receiver. Other non-specular interactions off the pillars and partitions are also apparent. The range in power of these paths is less dynamic than for the specular-only paths.

## Example 2: mmWave Channel Modeling with Diffuse Scattering

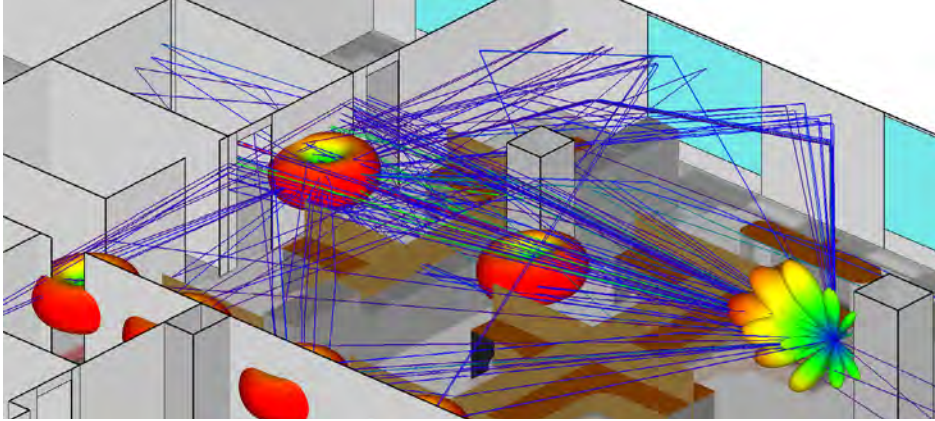


Figure 4a: Specular propagation paths to RX7

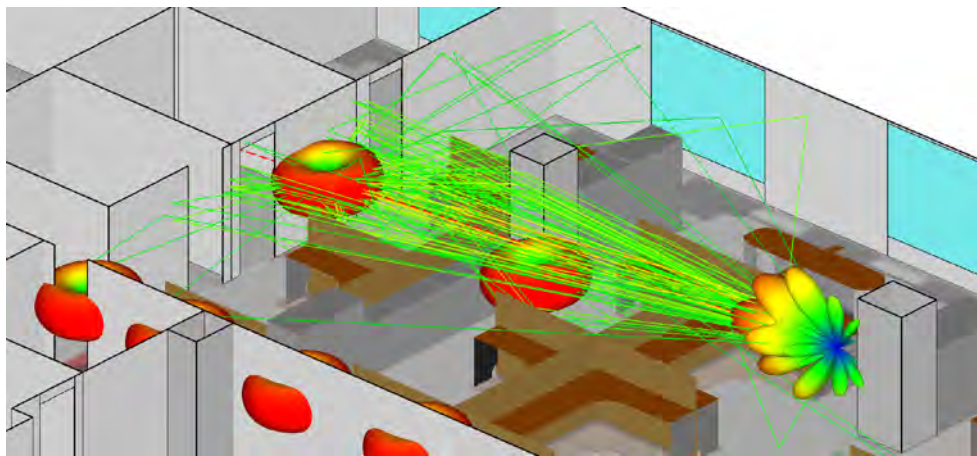


Figure 4b: Paths include diffuse scatter to RX7

Alternatively, the Complex Impulse Response (CIR) shows the power of each path as a function of its arrival time. Figures [5a] and [5b] show the CIR for RX7, for co-pol and cross-pol respectively. The specular-only results are plotted in blue, while the red results include diffuse scattering effects. The diffuse scatter results show more smearing, with arrival times occurring very close together, while the specular results are more discrete and spread out.

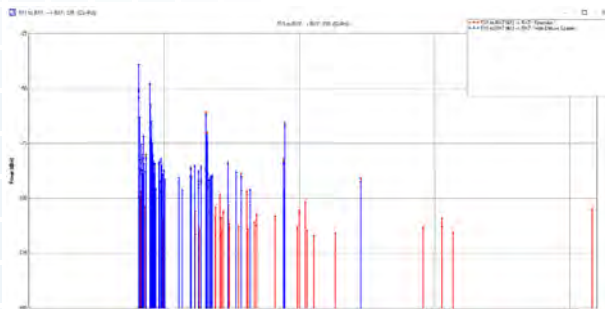


Figure 5a: Co-polarized Complex Impulse Response for RX7 with and without diffuse scattering

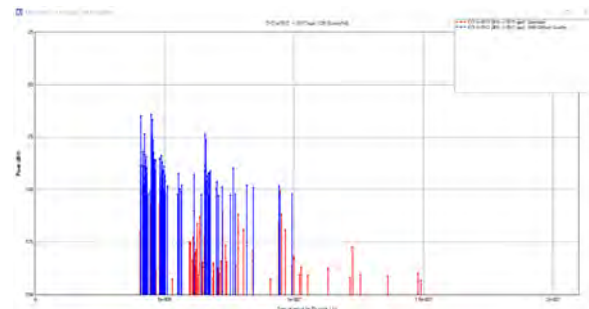


Figure 5b: Cross-polarized Complex Impulse Response for RX7 with and without diffuse scattering

## Example 2: mmWave Channel Modeling with Diffuse Scattering

The relevant path loss output files for comparison to measured data are listed in Table 2. A copy of these has been saved to the Aligned Antennas folder within the project. In addition, the simulated path loss results have been collected into four files for simpler plotting: Aligned\_specular\_CoPol.plt, Aligned\_specular\_XPol.plt, Aligned\_DS\_CoPol.plt, and Aligned\_DS\_XPol.plt

TX ID	TX Description	Co-pol RX ID	Co-pol RX Description	Output File Identifier	Cross-pol RX ID	Cross-Pol RX Description	Output File Identifier	Tx-Rx Range (m)
1	TX1 to RX1	11	RX1	t001_01.r011	21	RX1 xpol	t001_01.r021	6.40074
2	TX1 to RX2	12	RX2	t001_02.r012	22	RX2 xpol	t001_02.r022	7.66491
3	TX1 to RX3	13	RX3	t001_03.r013	23	RX3 xpol	t001_03.r023	9.57271
5	TX1 to RX4	14	RX4	t001_04.r014	24	RX4 xpol	t001_04.r024	7.2047
5	TX1 to RX5	15	RX5	t001_05.r015	25	RX5 xpol	t001_05.r025	11.8046
6	TX1 to RX6	16	RX6	t001_06.r016	26	RX6 xpol	t001_06.r026	13.7054
7	TX1 to RX7	17	RX7	t001_07.r017	27	RX7 xpol	t001_07.r027	12.1624

Table 2

Plot files for the measured results presented in [1] are located in the measurement folder. They can be plotted against the Wireless InSite data by importing their plots.

Figures [6a] and [6b] below show Wireless InSite predictions for path loss vs. distance for the seven receiver locations for the co-polarized (V-V) case and the cross-polarized (V-H) case. The red line shows path loss for specular paths only, and the blue line represents path loss with diffuse scattering. The measured results presented in [1] are shown in green. These plots show that diffuse scattering has a much greater impact on the cross-polarized results and is critical for providing accurate predictions.

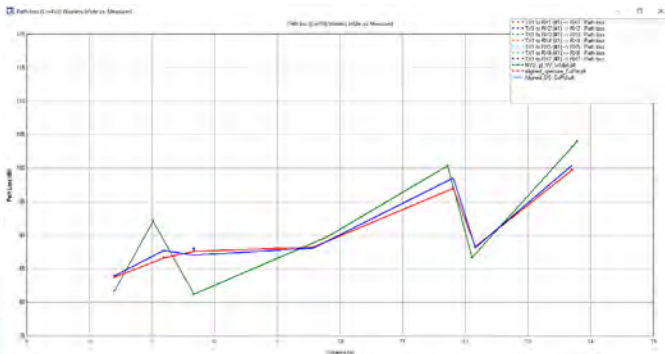


Figure 6a: Co-polarized TX/RX path loss - simulation with and without diffuse scattering compared to measured

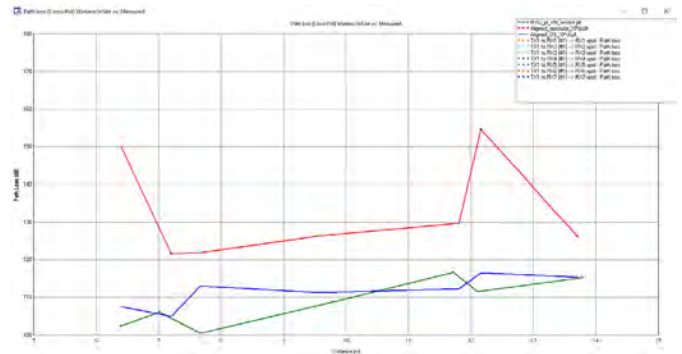


Figure 6b: Cross-polarized TX/RX path loss - simulation with and without diffuse scattering compared to measured

## Example 2: mmWave Channel Modeling with Diffuse Scattering

### References:

- [1] G. MacCartney, T.S. Rappaport, S. Sun, and S. Deng, "Indoor Office Wideband Millimeter-Wave Propagation Measurements and Channel Models at 28 and 73 GHz for Ultra-Dense 5G Wireless Networks," IEEE Access, Vol. 3, Dec 7, 2015, pp. 2388 - 2424
- [2] Effects of building materials and structures on radiowave propagation above about 100 MHz, Recommendation ITU-R P.2040-1, July 2015.
- [3] A. Von Hippel, and W. B. Westphal, Tables of Dielectric Materials, Volume V, Final Report, Laboratory for Insulation Research, Massachusetts Institute of Technology, Cambridge, MA, April 1957.
- [4] Degli-Esposti, V., F. Fuschini, E.M. Vitucci, and G. Falciasecca, "Measurement and Modeling of Scattering from Buildings", IEEE Transactions on Antennas and Propagation, Vol. 55, No. 1, January 2007, pp. 143-153.
- [5] Degli-Esposti, V., "A Diffuse Scattering Model for Urban Propagation Prediction", IEEE Transactions on Antennas and Propagation, Vol. 49, No. 7, July 2001, pp. 1111-1113.
- [6] Degli-Esposti, V., V.-M. Kolmonen, E.M. Vitucci, and P. Vainikainen, "Analysis and Modeling on co- and Cross-Polarized Urban Radio Propagation for Dual-Polarized MIMO Wireless Systems", IEEE Transactions on Antennas and Propagation, Vol. 59, No. 11, November 2011, pp. 4247-4256.
- [7] J. Pascual-Garcia, et. al., "On the Importance of Diffuse Scattering Model Parameterization in Indoor Wireless Channels at mm-Wave Frequencies," IEEE Access, February 8, 2016, © 2016 IEEE.

[Click to see the web version of this example](#)

[Request project files for this example](#)

Table of Contents

## Example 3: Simulation of MIMO Handset Antenna Array Performance

*Summary: Performance of a 12-port handset antenna array operating in LTE bands 42/43 (3400-3800 MHz) and band 46 (5150-5925 MHz) is analyzed in XFDTD for varying hand hold positions on the device. The results computed include S-parameters, Gain, Efficiency and Envelope Correlation Coefficient.*

A proposed design for a 12-port 5G massive MIMO mobile terminal was presented for operating in sub-6 GHz range, specifically LTE band 42 (3400-3600 MHz), band 43 (3600-3800 MHz), and band 46 (5150-5925 MHz) [1]. This device was shown to have good performance for 8x8 MIMO operation in bands 42/43 and 6x6 MIMO operation in band 46 by using several different antenna designs spaced around the edges of a mobile handset PCB. Here the performance of the antenna is simulated in XFDTD first with the handset alone and then in various configurations of either one or two hand grasping. The performance criteria evaluated are the return loss, isolation between antennas, the efficiency, gain, and the envelope correlation coefficient (ECC) which is an indicator of the diversity performance of antenna pairs.

### Antenna Layout

The device is shown in Figure 1 where the 12 antenna elements are visible and labeled around the edges of the PCB. At the top and bottom left are dual band inverted PI-shaped antennas which operate in all bands under consideration. These antennas are sometimes labeled as IA in the figures that follow and are numbered as Antennas 1 and 2. Along both sides of the antenna are six longer inverted L-shaped open slot antennas (LA) for the lower (LTE 42/43) bands and four shorter inverted L-shaped open slot antennas (SA) for LTE band 46. The antennas alternate between LA and SA down the sides with three LA and two SA antennas per side. The numbering of antennas is 3 through 7 on the right (numbers 3, 5, and 7 are LA) and 8 through 12 on the left (with 8, 10, and 12 being LA). The dual band antennas are designed with a longer and shorter arm for the lower and higher frequency bands. In Figure 2, Antenna 1 is shown with conduction currents flowing at 3.6 GHz onto the longer arm and at 5.5 GHz on the shorter arm. Two elements of the LA and SA antennas are shown in Figure 3 for comparison purposes.

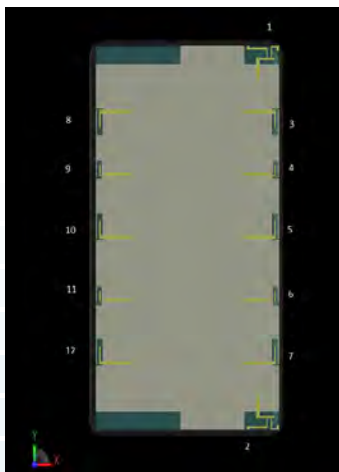


Figure 1: A CAD view of the device in the XFDTD software interface is shown where the screen and all antennas lie in the XY plane. The antenna elements are numbered 1 through 12 around the edge of the device.

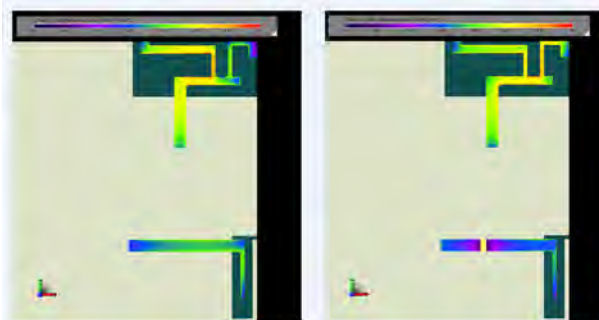


Figure 2: At the left of the figure are shown the conduction currents computed by XFDTD on the longer portion of antenna element 1 at 3.6 GHz in the LTE band 42/43 range. On the right are the conduction currents on the shorter arm of antenna element 1 at 5.5 GHz in the LTE band 46 range.

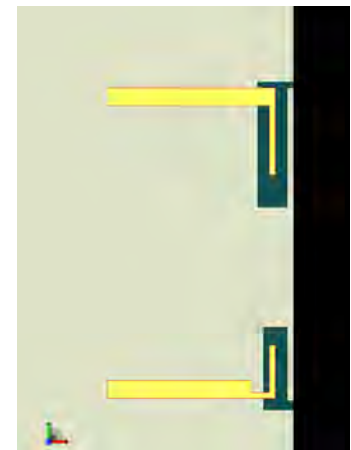


Figure 3: At the top of this view of the XFDTD interface is one of the longer arm open slot (LA) antennas for 3.6 GHz operation on the edge of the device. At the bottom is a shorter arm open slot (SA) antenna for 5.5 GHz use.

# Example 3: Simulation of MIMO Handset Antenna Array Performance

## Simulation in Free Space

As one measure of performance, the S-parameters of various antennas will be considered to show the return loss and isolation of the antennas. In Figure 4, the return loss for antennas 1 and 2 (the top and bottom IA antennas) is shown along with the S21 between them. As can be seen, the antennas have good return loss values in the lower LTE 42/43 bands and the higher LTE 46 band. S21 remains low over both bands, which is expected since the antennas are on extreme ends of the PCB. The return loss of all the LA antennas in LTE bands 42/43 is shown in Figure 5. Figure 6 shows the return loss of the SA antennas in band 46 along with the isolation between adjacent SA antennas and between adjacent SA and IA antennas. The isolation between adjacent LA antennas (and between adjacent LA and IA antennas) for the lower frequency bands is shown in Figure 7. In all cases the results are within the design tolerances of return loss under -6 dB (3:1 VSWR) and isolation -11 dB or better.

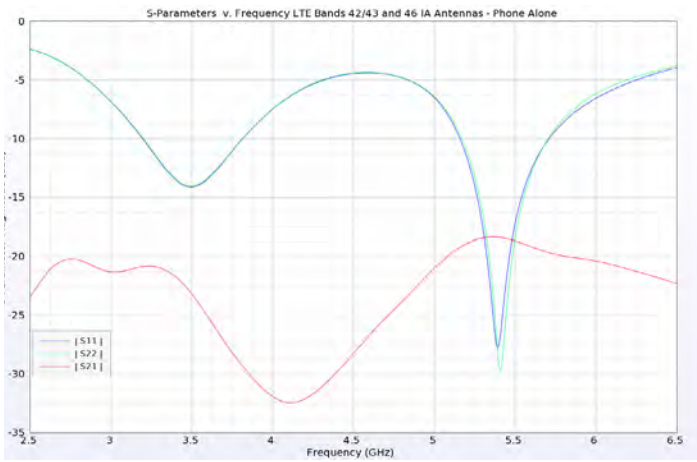


Figure 4: The S-parameters for antennas 1 and 2 are shown over all bands of operation of the device. There are two distinct operating regions: around 3.6 GHz and around 5.5 GHz. For both, the return loss is well below required levels while the isolation determined by S21 is down around -18 dB.

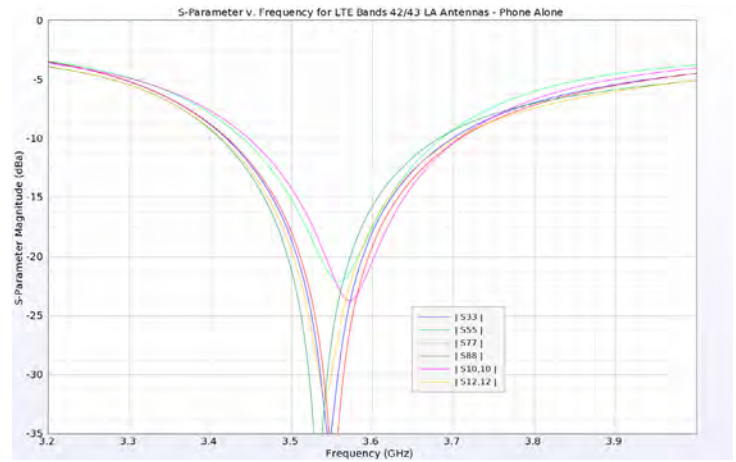


Figure 5: The return loss for all antennas in the lower band (LTE 42/43) are shown and have very good results.

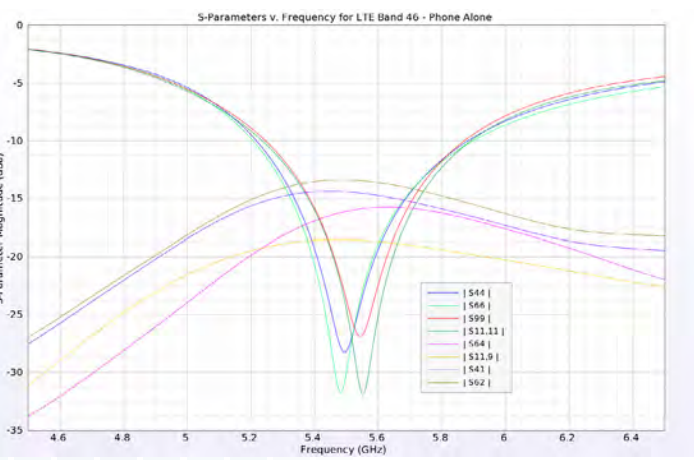


Figure 6: The return loss and isolation of select elements is shown for the higher band (LTE 46) with good results.

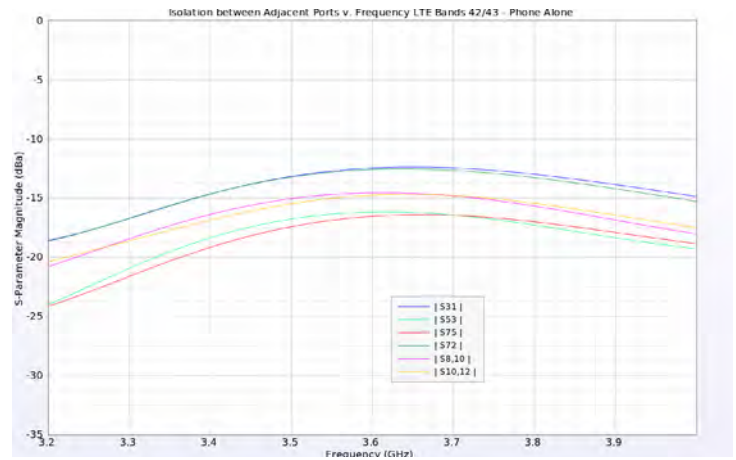


Figure 7: The isolation between select elements in LTE bands 42/43 are shown.

## Example 3: Simulation of MIMO Handset Antenna Array Performance

The antenna performance is determined by viewing the efficiency and gain of the various elements over their bands of operation. In Figure 8 the efficiency of the LTE Band 42/43 antennas is shown and is reasonable for the IA antennas (1 and 2) and moderate for the LA antennas (3, 5, 7, 8, 10, and 12). In the LTE 46 band, the antenna performance is better, with efficiencies above 50% as shown in Figure 9. Gain is plotted in the XY plane (the plane of the device screen) for various combinations of antennas. In each case, the antenna gain patterns are designed to radiate away from the center of the device. In Figure 10, the gain for the IA antennas at LTE bands 42/43 are shown and can be seen to have a maximum gain at a 45 degree angle from the antenna which is toward the corner of the device screen. In Figure 11, the gain for the LA antennas in the LTE 42/43 band on the right side of the phone is shown and, in each case, the maximum gain is along the X axis, away from the screen center. In Figure 12, the gain for the SA antennas on the right side of the phone in LTE band 46 is shown with similar characteristics.

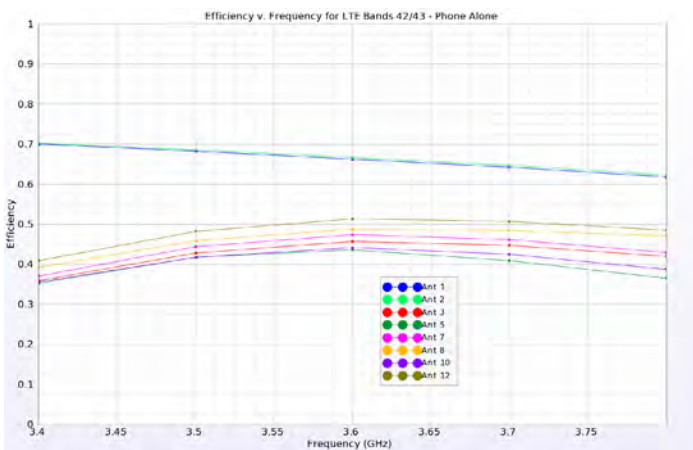


Figure 8: The efficiencies for antennas in the LTE band 42/43 are shown. The two IA antennas at the ends of the phone (1 and 2) show higher efficiency over 60% while the LA antennas on the sides of the phone have lower efficiencies between 35 and 50%.

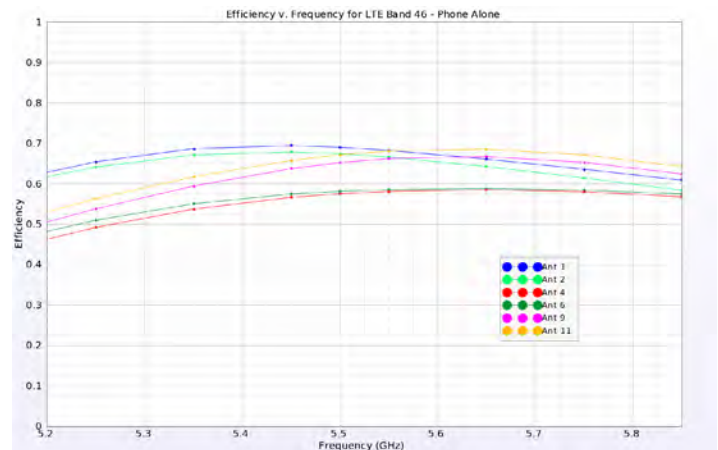


Figure 9: The efficiencies for all antennas in the higher LTE 46 band are above about 50% and show good performance.

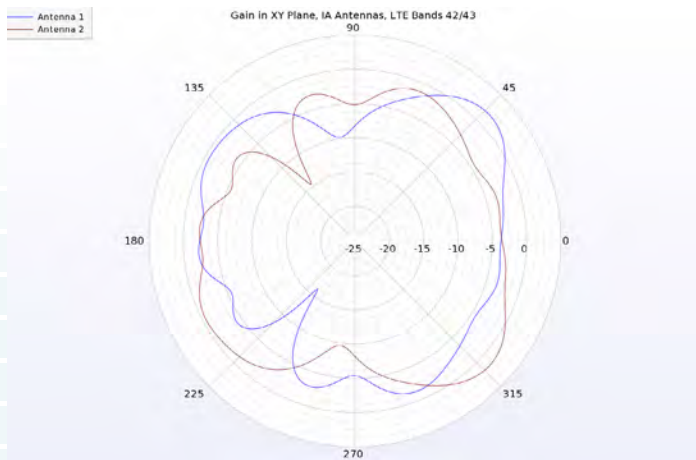


Figure 10: The gain patterns in the XY plane for the two IA antennas show peak gains toward the respective corners of the device.

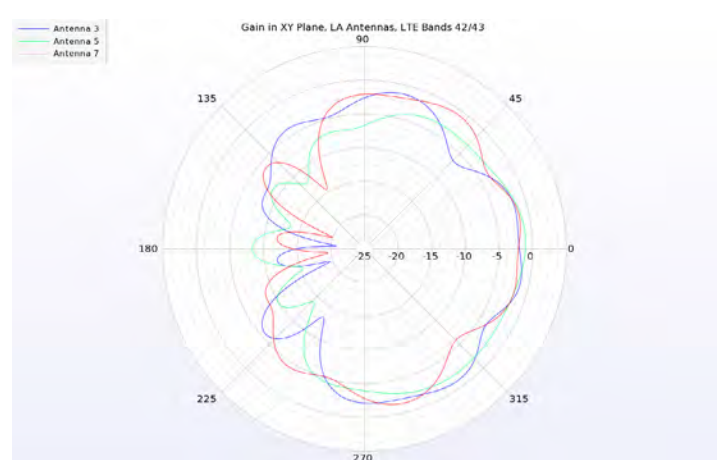


Figure 11: The LA antennas have peak gain toward the outer edge of the device. In this case, the antennas on the right side of the device are shown with peak gain in the +X direction.

## Example 3: Simulation of MIMO Handset Antenna Array Performance

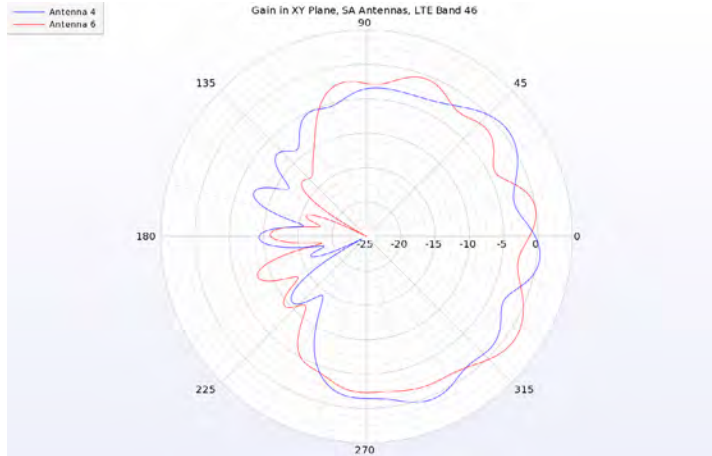


Figure 12: The SA antennas have peak gain toward the outer edge of the device similar to the LA antennas. Here antennas 4 and 6 are shown with peak gain in the +X direction.

To evaluate the diversity performance of antenna pairs, an important measure beyond the isolation is the envelope correlation coefficient (ECC). This measure is useful for determining how well a device will work for diversity and multiplexing applications where it is important that individual antennas perform independently from others. The basic criterion for ECC is a value less than 0.5. The ECC for various antenna pairs in the LTE 42/43 band and LTE 46 band are compared in Figures 13 and 14, respectively. All plots are well below the 0.5 limit with the maximum correlation being between Antennas 8 and 10 in the LTE 42/43 band at about 0.15.

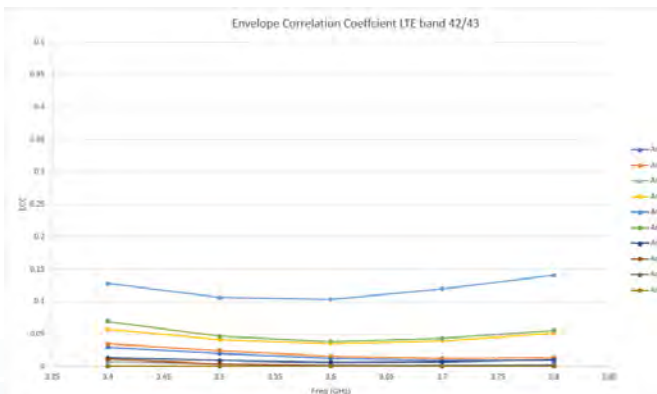


Figure 13: The Envelope Correlation Coefficient (ECC) for the LTE band 42/43 antennas is quite good with a peak value of 0.15.

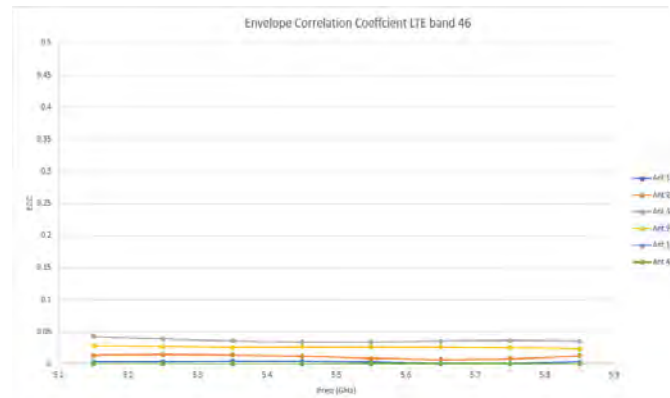


Figure 14: The Envelope Correlation Coefficient (ECC) for the LTE band 46 antennas is very good with no two antennas higher than 0.05.

### Simulation with Hands

To further test the phone operation in more realistic conditions, hand models are introduced in both single hand and two hand configurations, as shown in Figure 15. The positions are for left and right hand holds, two hands at the side mode, and two hands with thumbs typing configuration. Depending on the hand position, certain antennas will be covered and the performance will be affected. However, since there are multiple antennas on both sides of the device, in most situations there are still several antennas available with good performance.

## Example 3: Simulation of MIMO Handset Antenna Array Performance

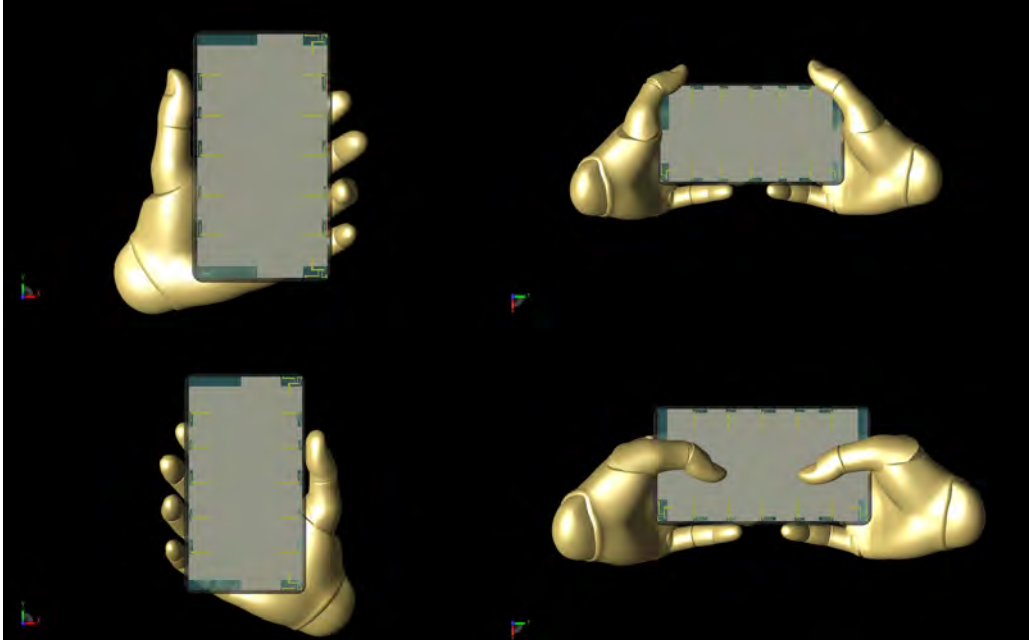


Figure 15: Shown are the four positions of the Poseable Hand model used in the study, which were positioned using controls within XFtd. Clockwise from top left: left hand hold, two hands at sides, two hands typing, and right hand hold.

The S-parameter performance remains good for all hand positions, although in some cases the return loss is significantly affected. For example, in Figure 16 the return loss for the LTE band 42/43 antennas is shown for the left and right hold positions and there is a noticeable difference versus the phone alone return loss shown in Figure 5. Similarly, the SA antennas operating in the LTE band 46 are also changed by the left and right hand hold positions as shown in Figure 17. For the two hand hold positions, there is less disruption to the S-parameters for the same antennas since the hands are not directly covering the antennas, as shown in Figures 18 and 19.

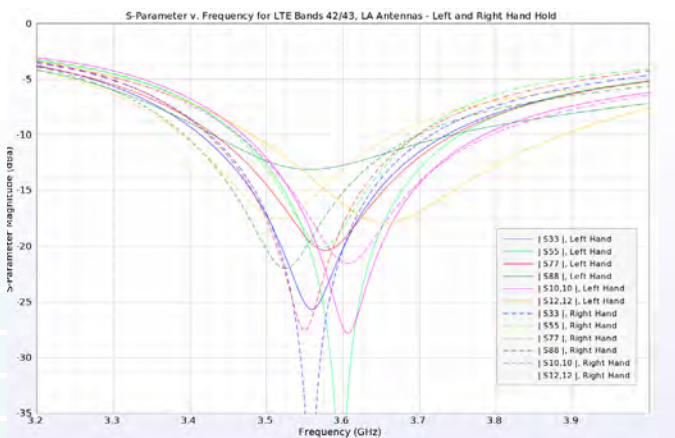


Figure 16: With the left and right hands holding the phone, the return loss results for the LTE band 42/43 antennas are changed but still good enough.

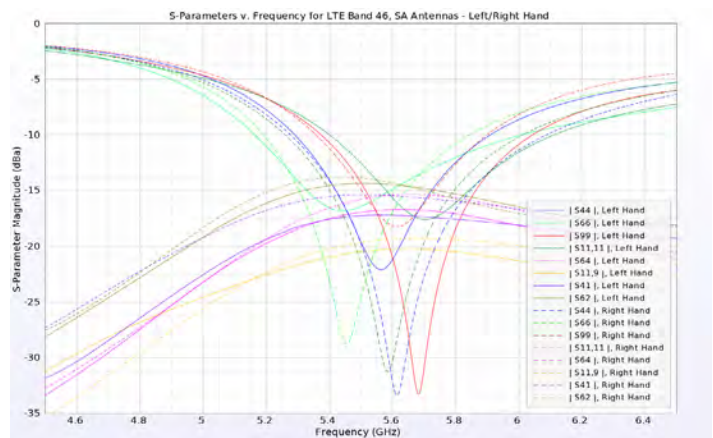


Figure 17: With the left and right hands holding the phone, the return loss and isolation remain acceptable for the LTE band 46 antennas.

## Example 3: Simulation of MIMO Handset Antenna Array Performance

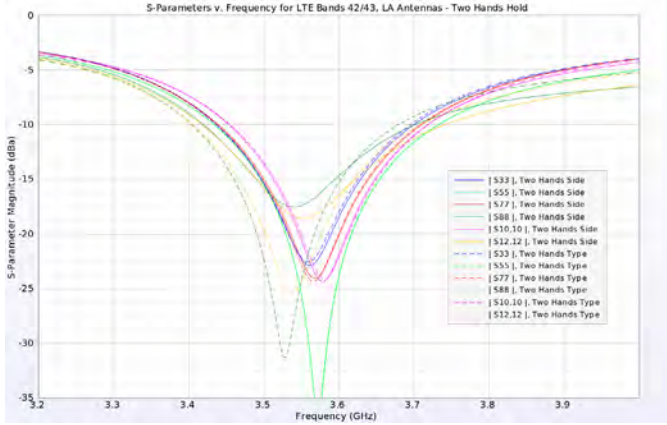


Figure 18: In the two hand configurations, the return loss in the LTE 42/43 band is only slightly changed and remains acceptable.

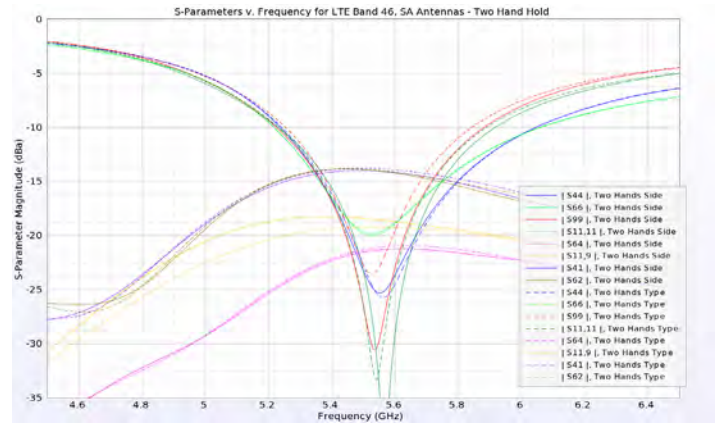


Figure 19: At the higher LTE band 46, the two hand configurations have only slight impacts on the return loss and isolation.

As can be expected, the efficiency is greatly affected by the presence of the hands. The patterns are disrupted and power is lost in the hand tissue resulting in worse performance. An extreme example is shown in Figure 20 for the case of the two hands at the sides in LTE bands 42/43 where the peak efficiency is only around 35%. Other cases studied had better performance.

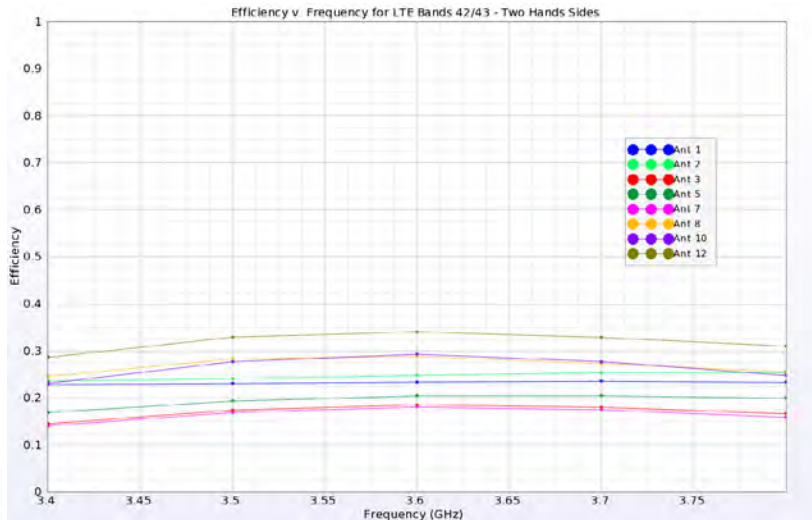


Figure 20: Efficiency is greatly affected by the hands on the phone. Here the efficiency for LTE bands 42/43 for the two hands at sides case is shown with no antenna above 35% efficiency.

The gain patterns are understandably impacted by the hand positions on the phone. Figure 21 shows the three-dimensional patterns of the six LA antennas at LTE bands 42/43 in the case of the phone alone. When the left hand is holding the phone, as shown in Figure 22, some of the patterns, particularly antenna 10 by the thumb, are greatly impacted and show much less gain. For the higher frequency LTE band 46 SA antennas on the sides, there are fairly uniform patterns when the device is alone, such as in Figure 23. With the hands at the sides and the finger next to the two bottom antennas, as in Figure 24, the patterns on the bottom antennas (4 and 6) are reduced compared to the top antennas (9 and 11). For the two hand typing configuration and the same antennas, the top antennas show an increase in gain due to the presence of the thumbs in the middle of the screen as shown in Figure 25. In summary, the peak gains for all configurations are detailed in Tables 1 and 2.

### Example 3: Simulation of MIMO Handset Antenna Array Performance

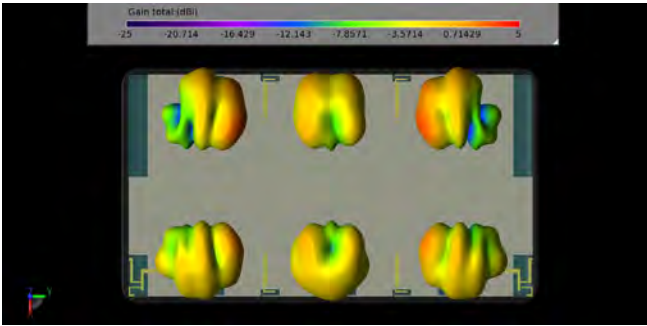


Figure 21: Three-dimensional gain patterns of the six LA antennas are shown at 3.6 GHz (LTE bands 42/43) for the case of the device alone in free space. Each antenna is radiating a pattern with peak gain to the outer edges of the device as desired.

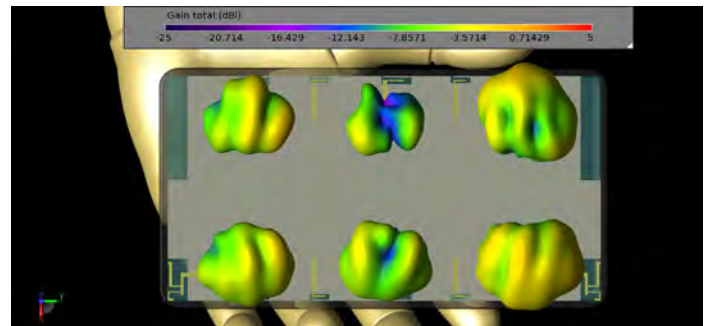


Figure 22: With the left hand holding the phone in LTE band 42/43, the gain patterns are modified and the center pattern under the thumb (antenna 10) is greatly reduced in gain.

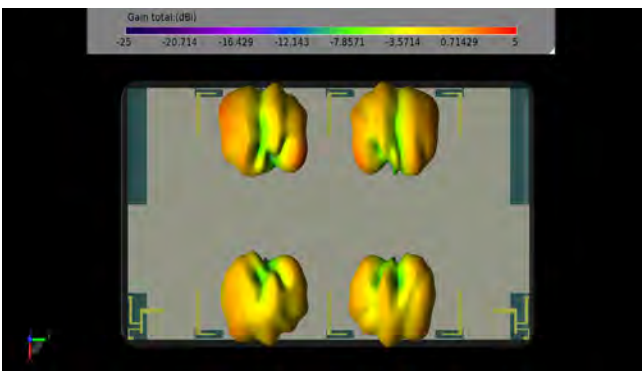


Figure 23: In LTE band 46, the three-dimensional gain patterns are shown with peak gain toward the outside of the device.

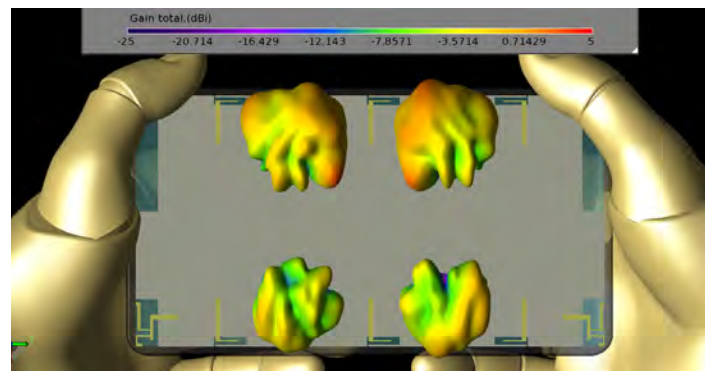


Figure 24: In the two hands at side position in LTE band 46, the gain patterns at the bottom of the phone (antennas 4 and 6) are disturbed by the presence of the fingers and are reduced compared to the upper patterns.

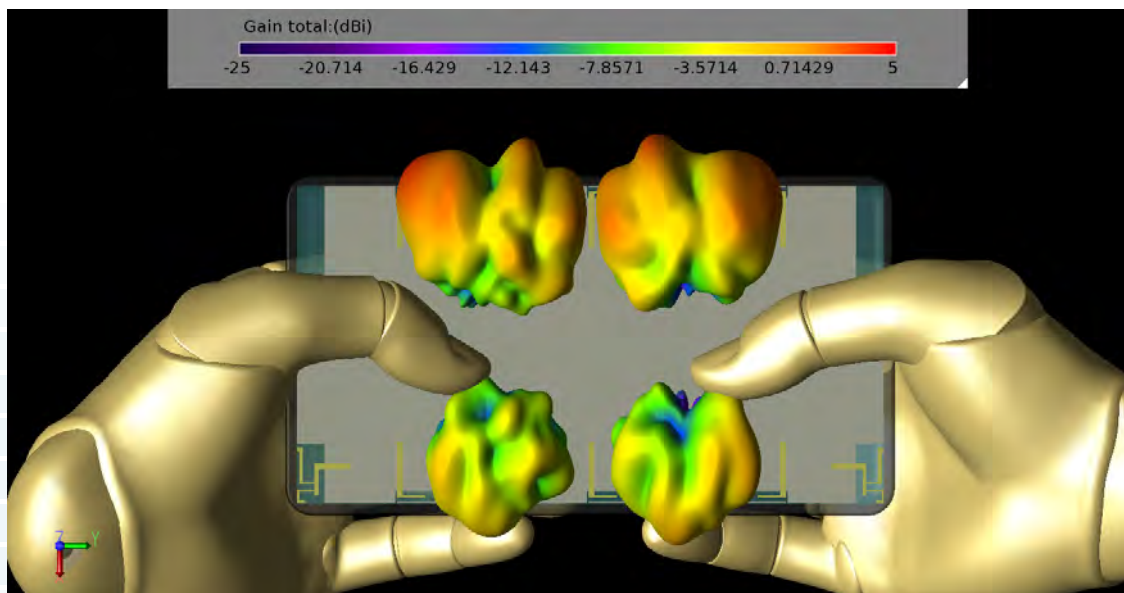


Figure 25: In the two hand typing configuration in LTE band 46 the upper patterns (antennas 9 and 11) are enhanced by the impact of the thumbs with give a reflector effect.

## Example 3: Simulation of MIMO Handset Antenna Array Performance

LTE 42/43	Antenna 1 3.6 GHz	Antenna 2 3.6 GHz	Antenna 3 3.6 GHz	Antenna 5 3.6 GHz	Antenna 7 3.6 GHz	Antenna 8 3.6 GHz	Antenna 10 3.6 GHz	Antenna 12 3.6 GHz
Alone	1.865	2.124	1.513	-0.153	1.633	2.774	-0.211	2.939
Left Hand	1.816	1.101	-0.832	-3.129	-1.778	-1.319	-3.64	-1.241
Right Hand	1.408	2.86	0.788	1.108	0.96	-0.478	-1.815	0.18
2 Hand Side	1.116	1.261	-1.122	-1.535	-1.764	0.841	-1.523	1.475
2 Hand Type	1.081	0.907	-1.193	-1.758	-1.58	2.058	0.329	2.296

Table 1: The peak gains for each antenna at 3.6 GHz (LTE bands 42/43) are shown for the five configurations.

LTE 46	Antenna 1 5.5 GHz	Antenna 2 5.5 GHz	Antenna 4 5.5 GHz	Antenna 6 5.5 GHz	Antenna 9 5.5 GHz	Antenna 11 5.5 GHz
Alone	4.753	4.921	0.72	1.262	2.27	2.837
Left Hand	2.894	2.612	-0.583	-0.491	0.218	-0.828
Right Hand	3.87	4.096	1.541	2.735	0.714	0.88
2 Hand Side	1.587	2.571	-0.11	-1.209	2.133	2.812
2 Hand Type	2.755	3.256	0.33	-1.215	3.097	3.74

Table 2: The peak gains for each antenna at 5.5 GHz (LTE band 46) are shown for the five configurations.

As can be expected, the ECC results are also affected by the presence of the hands. In all cases though, the ECC remains well below the 0.5 threshold as desired. The worst-case ECC results are for the left and right hand hold positions in the LTE band 42/43 antennas where the ECC can reach as high as 0.4 as shown in Figures 26 and 27. All cases in LTE band 46 remain with an ECC below 0.2.

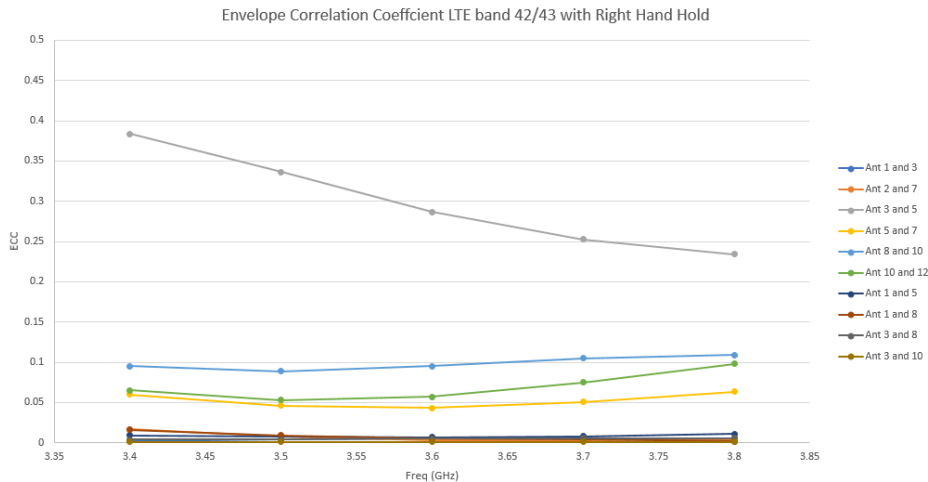


Figure 26: The worst-case ECC is shown for the right hand hold case at LTE bands 42/43 where the correlation between antennas 3 and 5 reaches as high as 0.4. This is still below the threshold of 0.5.

## Example 3: Simulation of MIMO Handset Antenna Array Performance

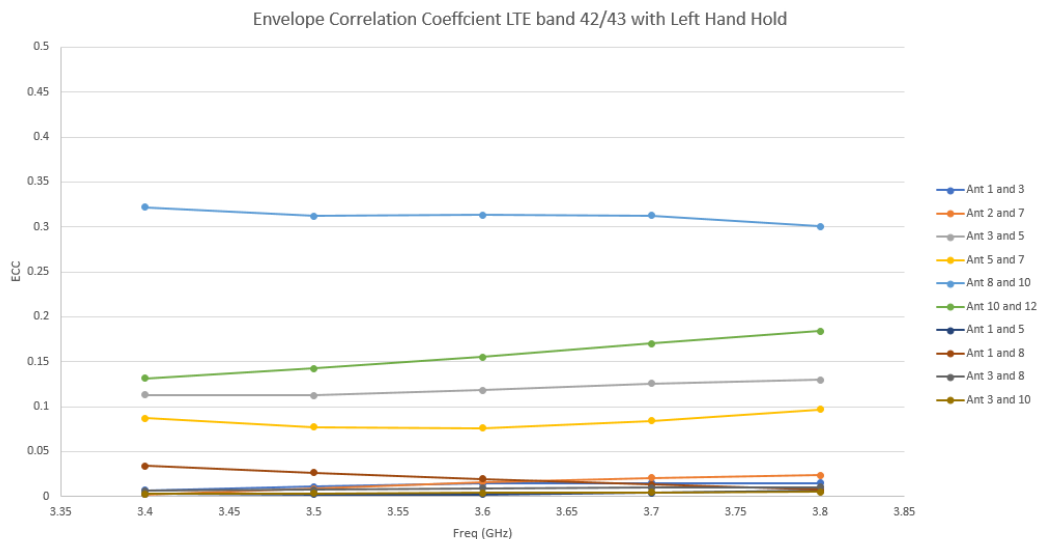


Figure 27: In the left hand hold position at LTE bands 42/43, the ECC is highest for antennas 8 and 10 with a peak level around 0.33.

The 12-port antenna can be seen to deliver very good performance with a variety of use configurations. While some hand placements degrade the performance of antennas that are covered, there are other antennas available to maintain operation.

### Reference:

[1] Yixin Li, Chow-Yen-Desmond Sim, Yong Luo, and Guangli Yang, "12-Port 5G Massive MIMO Antenna Array in Sub-6GHz Mobile Handset for LTE Bands 42/43/46 Applications," IEEE Access vol. 6, pp. 344-354, 2018.

[Click to see the web version of this example](#)

Table of Contents

## Example 4: EM Simulation of 28 GHz Series-Fed Patch Antenna Array for 5G

*Summary: Series-fed patch elements forming an array are simulated to demonstrate antenna performance and beamforming including S-parameters, gain, and effective isotropic radiated power (EIRP) at 28 GHz. Beam steering is performed in one plane by adjusting the phasing at the input ports to each of eight elements.*

Part of the discussion for next generation wireless communication is the ability to rapidly steer beams from antenna arrays at higher frequencies. In this example, a proposed antenna [1] is comprised of eight series-fed patch elements, each containing eight patches that are connected in such a way to produce both standing wave and traveling wave behavior. The array produces a single beam which may be swept in the horizontal axis of the array by varying the phasing of the signals at the inputs of the elements.

The array is evaluated for standard performance metrics such as S-parameters and gain as well as for effective isotropic radiated power (EIRP). EIRP is effectively the input power supplied to an antenna multiplied by the gain of that antenna. It indicates the total power that an isotropic antenna would have to radiate to match the signal strength of the main beam of the evaluated antenna. Simulations in this paper are performed using XFDTD® EM Simulation Software.

The final array is built from eight separate 1x8 series-fed patch elements such as that shown in Figure 1. The characteristics of a single element will be examined first before discussing the array. Each patch is 3.539 mm x 3.539 mm and is separated 3.539 mm. The last patch in the line has a notch cutout of 0.6269 mm x 2.727 mm in the connecting side. The microstrip lines connecting the patches are 0.494 mm in width. The initial feed line is 2.215 mm long and 0.72 mm wide. The total length of the element is 55.3 mm. The antenna is on a substrate with a dielectric constant of 2.2, a loss tangent of 0.0009 and a thickness of 0.254 mm.

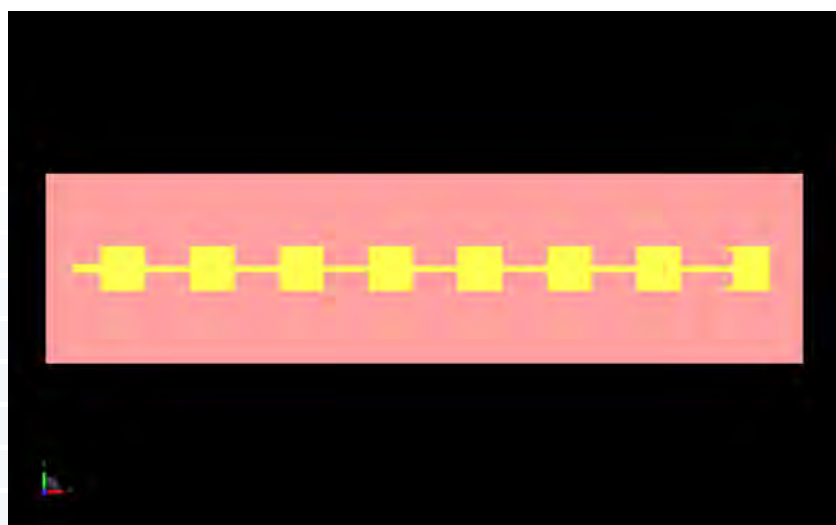


Figure 1: CAD representation of a single 1x8 patch element viewed from the top.

## Example 4: EM Simulation of 28 GHz Series-Fed Patch Antenna Array for 5G

The geometry is gridded into an FDTD mesh using the PrOGrid feature in XFDTD. Each element of the geometry has Automatic Fixed Points enabled to perfectly align the corners of the structures with the FDTD grid. The minimum feature size for Good Conductors is set to be the width of the microstrip line between patches and that is defined to have at least eight FDTD cells across it. The dielectric substrate is defined to have at least five FDTD cells of thickness using the Poor Conductor minimum feature size setting. The overall number of cells per wavelength is set to 60 to ensure good results.

The input for the element is a voltage source which is initially excited by a broadband signal covering from 26 to 30 GHz for S-parameter results. Following a simulation for computing the S-parameters, the return loss is found to have a weak response due to a poor match. This is corrected by adding a matching circuit consisting of a series inductor and parallel capacitor (0.22 nH and 0.09 pF). The matched input return loss produces a null near 28 GHz (Figure 2). The far field gain pattern for the single element (Figure 3) indicates a strong central lobe normal to the patches with peak gain of 16.77 dBi. The peak side lobe is seen to be down about 13 dB from the main lobe as shown in Figure 4.

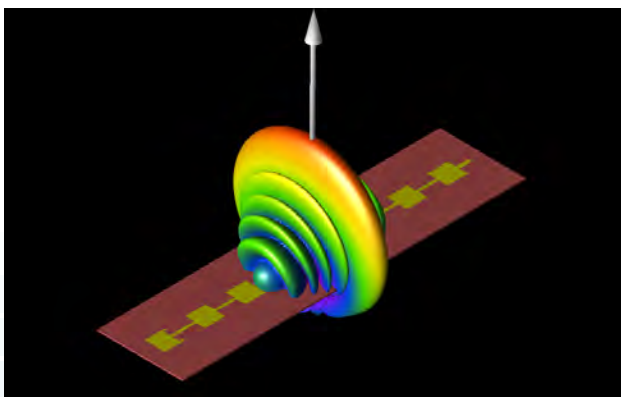


Figure 3: The far-field gain pattern of the 1x8 element has a strong central beam that is focused in one dimension and circular in other. The peak gain is just under 17 dBi.

To create the array, eight of the single 1x8 elements are spaced 5.352 mm apart to form an array that measures 55.3 mm x 41 mm as shown in Figure 5. To generate broadband S-parameter data, a pulse excitation is applied to each of the eight input ports.

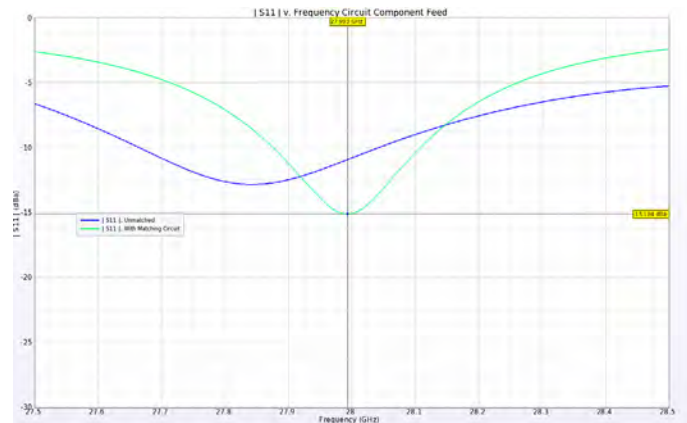


Figure 2: The Return Loss for the 1x8 element is slightly out of tune when fed with a 50-ohm source. By adding a simple LC matching circuit, the device is tuned to 28 GHz.

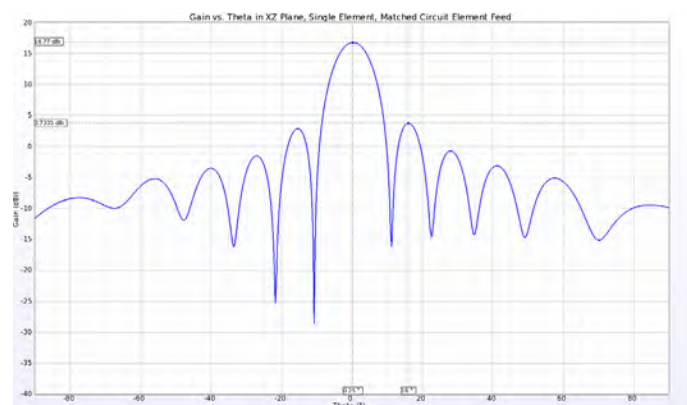


Figure 4: In the XZ dimension (E-plane) the antenna pattern has main beam with gain of 16.77 dBi and a peak side lobe level of 3.73 dBi.

## Example 4: EM Simulation of 28 GHz Series-Fed Patch Antenna Array for 5G

A matching circuit similar to that used for the single element is applied to all input ports of the array. The return loss for all eight ports is seen to be very similar as shown in Figure 6, while the isolation between adjacent ports is below -15 dB for each (Figure 7).

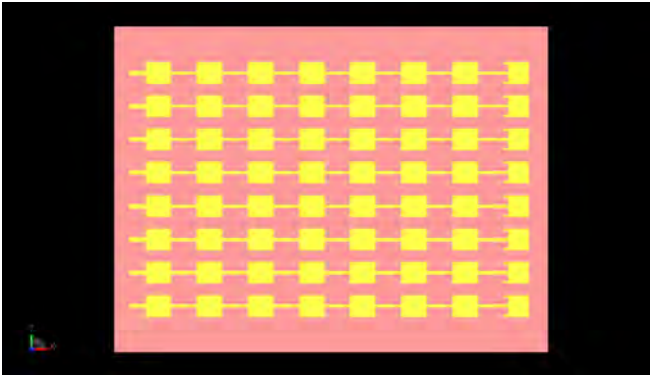


Figure 5: Shown is a CAD representation of the combination of eight of the 1x8 elements into an array. The elements are spaced 5.352 mm apart, center to center.

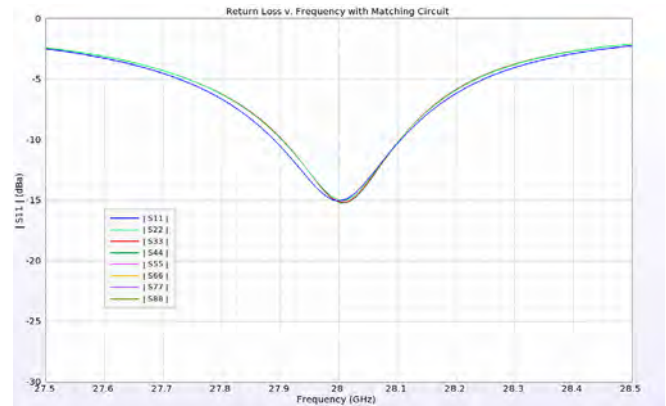


Figure 6: The Return Loss of each port is shown to be tuned for 28 GHz after the addition of simple LC matching circuits to each feed.

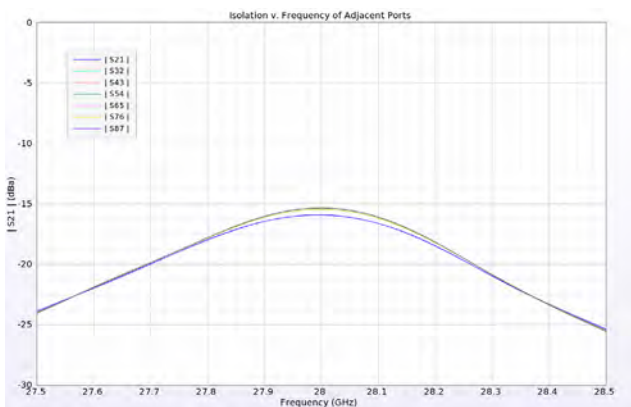


Figure 7: The isolation between adjacent ports is shown to be less than -15 dB for all possible combinations.

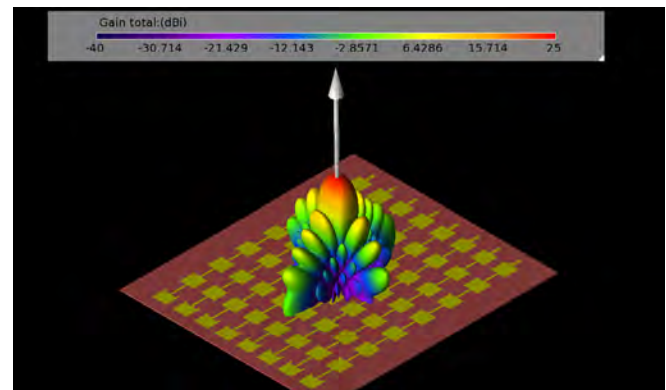


Figure 8: The gain pattern for the array when all inputs are fed in phase results in a strong central beam with gain of 24 dBi.

Depending on the phasing of the signals at each of the input ports, a number of different beams may be defined. When all ports are fed in phase, the beam normal to the array plane is formed with the maximum gain of 24 dBi (Figure 8). Due to the nature of this geometry the beams may only be steered in one plane, parallel to the line of input ports. To adjust the phasing, the Butler Matrix equation is used to compute the inter-element phase difference. It is defined as:

$$\alpha_i = [(2i - 1) - M]/M * \pi$$

where  $\alpha_i$  is the phase difference between elements,  $i$  is the beam number or input port number of the Butler Matrix, and  $M$  is the number of ports. In this case, the phasing for beams 1-8 is -157.5 deg, -112.5 deg, -67.5 deg, -22.5 deg, 22.5 deg, 67.5 deg, 112.5 deg, and 157.5 deg.

## Example 4: EM Simulation of 28 GHz Series-Fed Patch Antenna Array for 5G

The phase shift is applied across the input ports, so the first port will have a shift of 0 deg, the second -157.5 deg, the third -315 deg, etc. for the case of beam 1. These phase shifts are applied with a sinusoidal input at 28 GHz. The resulting beams in the YZ (E-plane) are shown in Figure 9 as a series of line plots with main lobe directions of +/- 55 degrees, +/- 37 degrees, +/- 21.5 degrees, and +/- 7 degrees. In three dimensions, beams 1 through 4 may be seen in Figures 10 - 13. All eight beams are shown in one three-dimensional image in Figure 14.

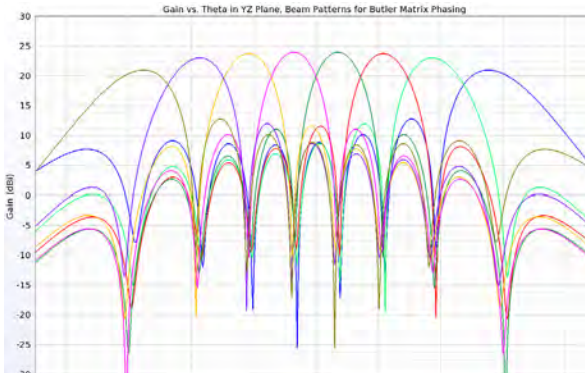


Figure 9: After applying Butler Matrix phase shifts to each port, a directed beam is formed. Shown are eight possible beams.

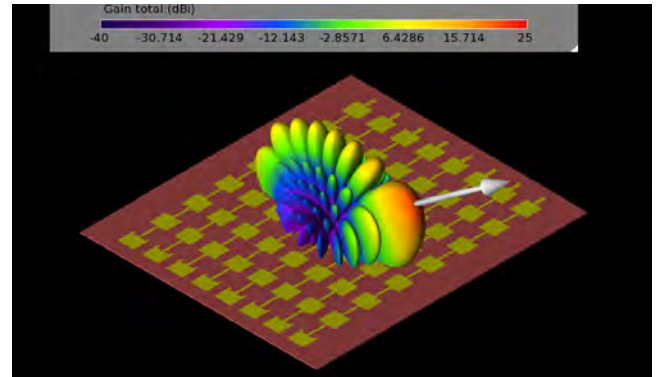


Figure 10: The gain pattern formed from the Butler Matrix phasing for beam #1 (-157.5 degrees per port) has a broad beam with maximum gain at 55 degrees.

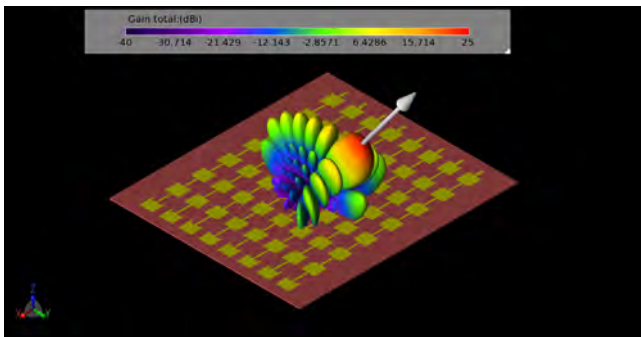


Figure 11: The gain pattern formed from the Butler Matrix phasing for beam #2 (-112.5 degrees per port) has a more focused beam with maximum gain at 37 degrees. The white arrow indicates the direction of the peak gain.

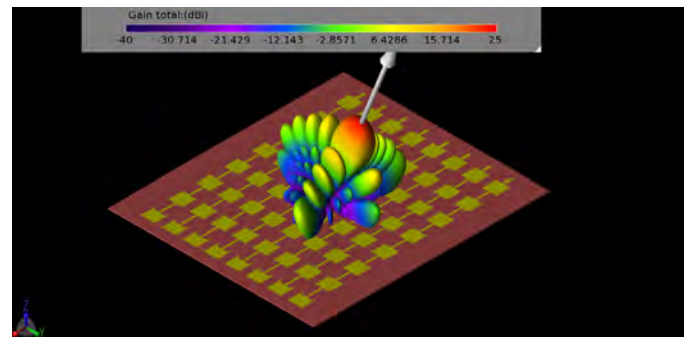


Figure 12: The gain pattern formed from the Butler Matrix phasing for beam #3 (-67.5 degrees per port) has maximum gain at 21.5 degrees.

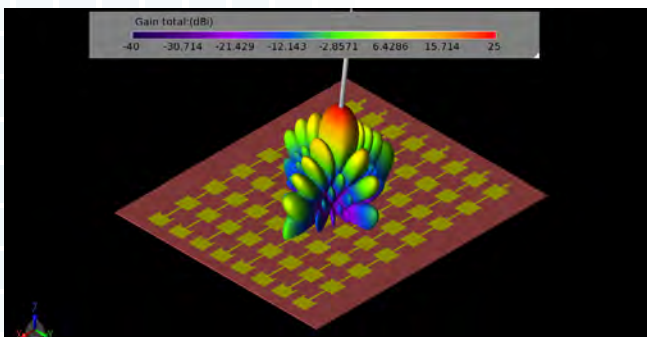


Figure 13: The gain pattern formed from the Butler Matrix phasing for beam #4 (-22.5 degrees per port) has maximum gain at 7 degrees.

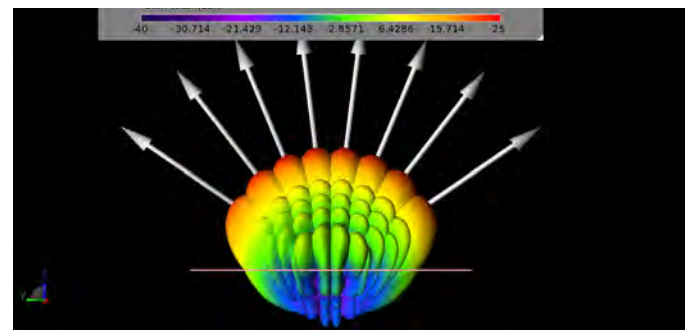


Figure 14: Shown is a side view of the eight beams produced by the Butler Matrix phasing equation. Each beam represents a separate simulation.

## Example 4: EM Simulation of 28 GHz Series-Fed Patch Antenna Array for 5G

This array has been shown to form eight beams with the Butler Matrix phasing; however, a further analysis of the total gain over all possible phasing combinations is possible by computing the Cumulative Distribution Function of the Effective Isotropic Radiated Power. This plot shows the fractional area of the three-dimensional far-field sphere that the array covers for a given amount of input power. For this array, the CDF of EIRP plot (Figure 15) shows that for an input power of 23 dBmW, the array has positive gain over about 27.4% of the far-zone sphere. This represents the scanning area where the beams have positive gain, which is limited by the ground plane under the array that blocks 50% of the radiation volume. The upper hemisphere of the far zone region is scanned by the beams in only one axis due to the design of the array, so therefore the scanned region is relatively limited. The plot also shows that the peak EIRP is about 46.4 dBmW.

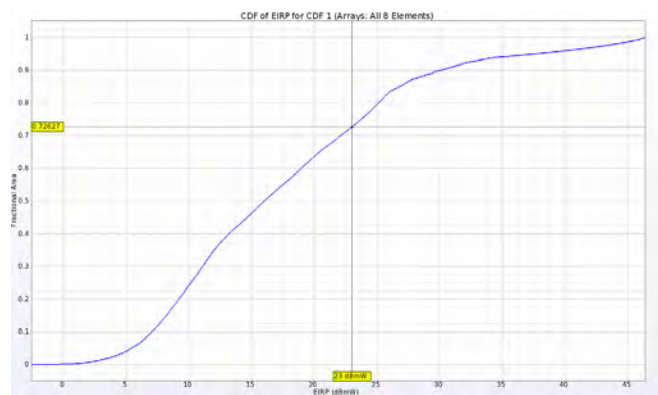


Figure 15: The plot of the cumulative distribution function of the EIRP shows that for 23 dBmW of input power, about  $(1 - .726)$  or 27.4% of the three-dimensional far field sphere will have positive gain.

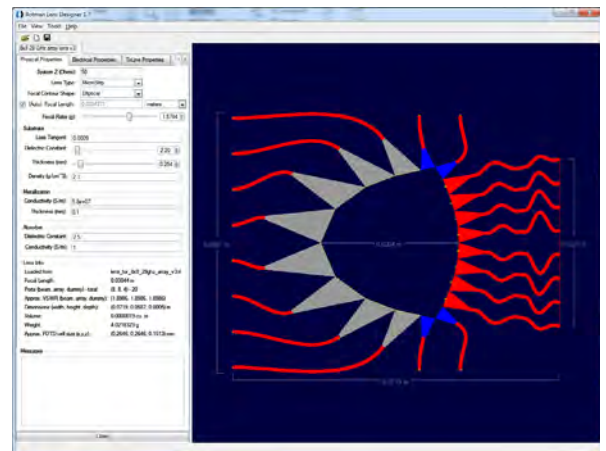


Figure 16: A Rotman Lens device suitable for use as the front end of the array is shown in Remcom's RLD software.

As an alternative to using the Butler Matrix equations and adjusting the phases in the software, it is also possible to use a true time delay device such as a Rotman Lens in the simulation to form the beams with this array. Using Remcom's Rotman Lens Designer® (RLD), a suitable lens (shown in Figure 16 in the RLD software) was designed to meet the criteria of the array. After exporting the CAD file of the lens from RLD and importing it into XFDTD, a complete geometry is made with eight input ports and four sidewall dummy ports (Figure 17). In the simulations the beams are created by feeding a single port at a time rather than adjusting the phasing over each port. Following eight simulations, each with a different port active, the eight beams formed by the array are visible in Figure 18. The coverage is similar to the Butler Matrix phasing shown previously in Figure 14.

## Example 4: EM Simulation of 28 GHz Series-Fed Patch Antenna Array for 5G

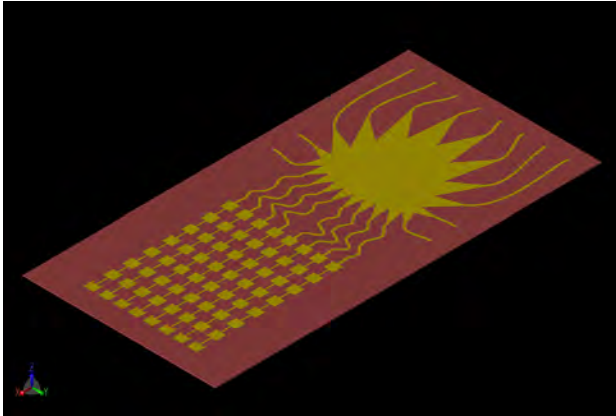


Figure 17: The resulting geometry of the array with the Rotman Lens beamforming stage are shown as a three-dimensional CAD file in XFDTD.

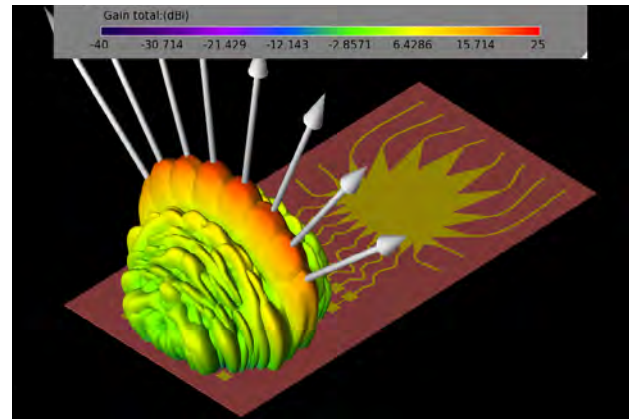


Figure 18: The eight possible beam patterns from the array generated by activating one of the ports of the Rotman Lens at a time are shown.

### Reference:

[1] M. K. Ishfaq, T. A. Rahman, Y. Yamada, and K. Sakakibara, "8x8 Phased Series Fed Patch Antenna Array at 28 GHz for 5G Mobile Base Station Antennas," 2017 IEEE-APS Topical Conference on Antennas and Propagation in Wireless Communications (APWC), pp. 160-162, 2017.

[Click to see the web version of this example](#)

Table of Contents

## Example 5: Throughput of a 5G New Radio FD-MIMO System in an Urban Area

*Summary: This example demonstrates how a custom beamforming table can be used to model downlink data rates from three MIMO base stations for 5G New Radio in a section of Boston.*

Wireless InSite's Communication Systems Analysis module is a set of post-processing routines that builds on the X3D model's high-fidelity MIMO calculations to predict system throughput and bit error rate. This example utilizes these routines to analyze throughput between three small-cell base stations employing Full Dimension (FD) MIMO beamforming to User Equipment (UE) moving along a route, using 5G New Radio (NR) in a dense urban environment.

### Project Description

The building and foliage geometry was imported from a high resolution shapefile of geometry for a section of downtown Boston, MA. The imported city model, foliage, and the terrain contain a total of 6,452 faces. The buildings and terrain are assigned concrete material properties with conductivity of 0.484 S/m and permittivity of 5.31 taken from ITU data for concrete at 28 GHz [1], [2], while foliage is modeled using a foliage penetration loss model by Weissberger [3].

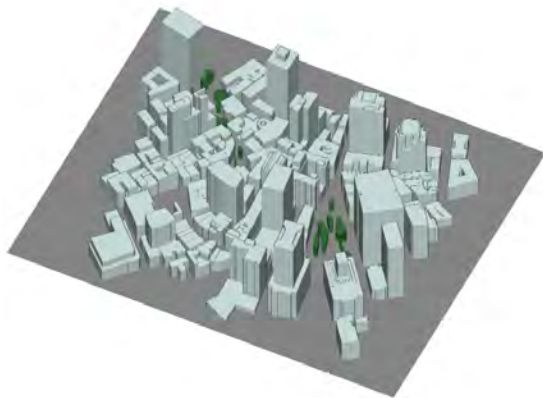


*Figure 1: Isometric and overhead view of project geometry in Wireless InSite.*

Each transmitter represents a base station and uses an 8x8 dual polarized patch array consisting of a total of 128 elements. Cross-polarized isotropic antennas are used at receiver locations along the route. Wireless InSite's GPU-accelerated X3D model was used to provide high fidelity propagation results which include reflections from the buildings and terrain and diffractions from building edges. The combination of high resolution geometry and high fidelity propagation modeling is necessary to achieve accurate results at 5G NR frequencies. The propagation model calculates the H-matrix from each element of the three transmitters to the receiver locations ( $128 \times 2 = 256$  entries per tx-rx pair).

### Communication Systems Analyzer

Wireless InSite's Communication Systems Analyzer provides capabilities for predicting throughput, bit error rate, and other outputs from multiple transmitters by post-processing the high-fidelity H-matrix results from the propagation simulation. Within a communication system, users can set input parameters for:

- Selecting transmitter and receiver sets to be included in the analysis
- Designating transmitters as base stations or interference sources
- Setting uniform noise and interference levels
- Optionally including interference between base stations
- Selecting BER or throughput analysis
- Selecting transmitter beamforming options
- Setting diversity options for MIMO receiving antennas

In this example, a communication system is defined, specifying analysis of throughput between three base stations and a UE traveling along a mobile route. The communication system properties window defines a custom beamforming table for the base stations, the use of selection combining by the UE, and a custom throughput table based on 3GPP specifications to be used in calculating the throughput for the link.

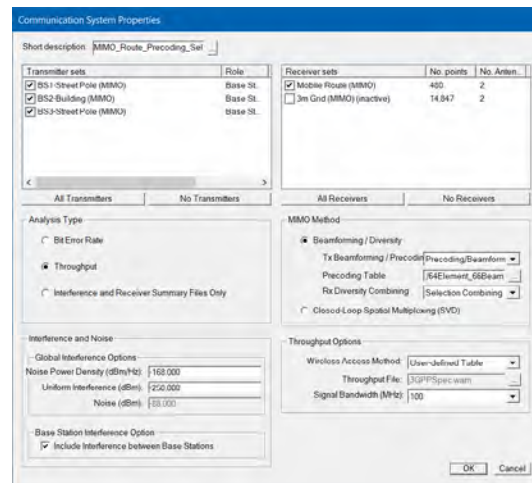


Figure 2: Communication system properties window for calculating throughput for a MIMO system.

### Custom Beamforming with a Precoding Table

The user-defined precoding table is a text file containing antenna element weightings for the transmitting MIMO antenna. Each record in the file represents a beam that the antenna elements are capable of producing. This example uses a table that describes 66 antenna beams that allow the transmitter to scan horizontally from -50 to 50 degrees and vertically from -10 to +40 degrees in 10 degree increments, by varying the phase of each antenna element. Base stations will select the antenna beam that maximizes the power at the receiver for each position of the UE.

### Custom Throughput Analysis for a 5G NR Device

The throughput for the 5G NR device at the receiver also uses a custom file, mapping SINR at the device to an achievable downlink data rate. Throughput values for this table were calculated using the equation published in 3GPP TS 38.306 v15.2, which calculates data rates for 5G NR for each potential modulation and coding scheme (MCS) and takes into account overhead for signaling and control and differences between uplink and downlink transmission [4] [5]. Estimates were for a single component carrier with a 100 MHz bandwidth and assumed similar relationships between the achievable MCS and the SINR as has been observed for LTE.

## Results

### Receiver Diversity

Three communication systems were created to analyze the effects of selection combining, equal gain combining, and maximal ratio combining for the 5G NR user equipment (UE). Results in Figures 3 and 4 show that in this scenario and configuration, there is not a substantive difference between the three diversity methods for SINR or throughput. The remainder of this example will use selection combining for the UE and custom beamforming at the base stations.

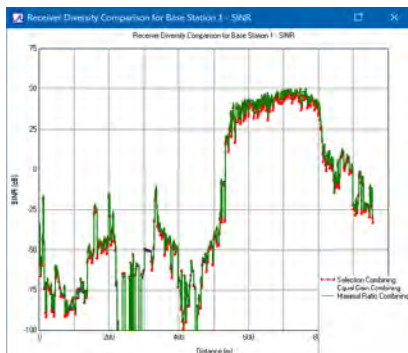


Figure 3: SINR comparison of receiver diversity methods for base station 1.

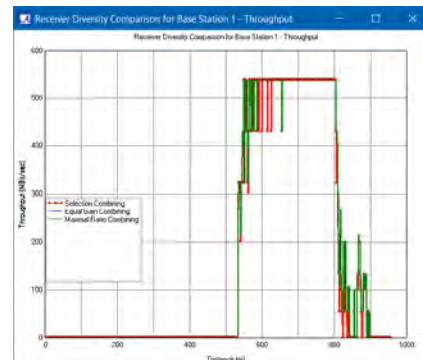


Figure 4: Throughput comparison of receiver diversity methods for base station 1.

### SINR and Throughput for Custom Beamforming and Selection Combining

SINR and throughput results are provided for each individual base station and for all three base stations working together. In this example, the 5G NR will establish a link with the base station that provides the highest SINR value. The red line in Figures 5 and 6 represents the overall performance of the three base stations to the UE, according to the base station that achieves the highest SINR at each point along the route. The blue line represents the contribution of base station 1 to the SINR and throughput. In regions where the blue and red lines overlap, the receiver establishes a link with base station 1. Contributions from the other two base stations are also plottable but were omitted for clarity of the graphs.

## Example 5: Throughput of a 5G New Radio FD-MIMO System in an Urban Area

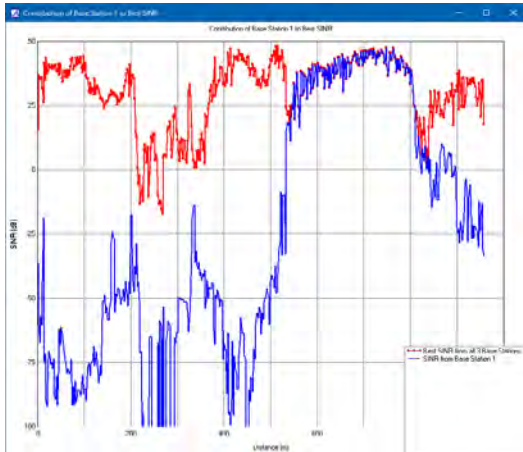


Figure 5: Total SINR (red) and SINR from Base Station 1 to UE (blue).

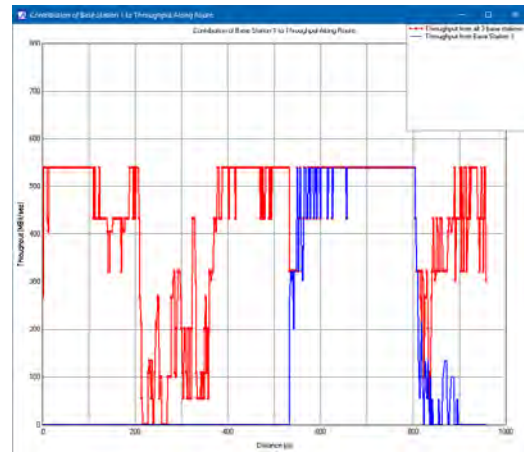


Figure 6: Total throughput (red) and throughput from Base Station 1 to UE (blue).

### Evaluation of the Beamforming Table vs. Maximum Ratio Transmission

Maximum Ratio Transmission beamforming calculates an optimal beam to each receiver location. In Figures 7 and 8, the SINR and throughput results using a custom beamforming table (blue) are compared against MRT (red). In most locations the predefined beams from the custom beamforming table are able to achieve nearly the same SINR and throughput as MRT (a more optimal, adaptive technique), but there are sections where adding more targeted beams would improve the results. Between 225 and 350 m along the route, the SINR values are too low to allow adequate throughput values with both beamforming methods. To improve coverage in this location, it would be necessary to add an additional base station.

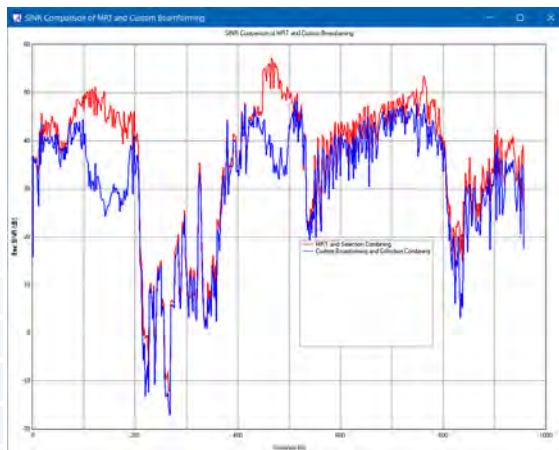


Figure 7: Comparison of SINR for custom (blue) and MRT (red) beamforming.

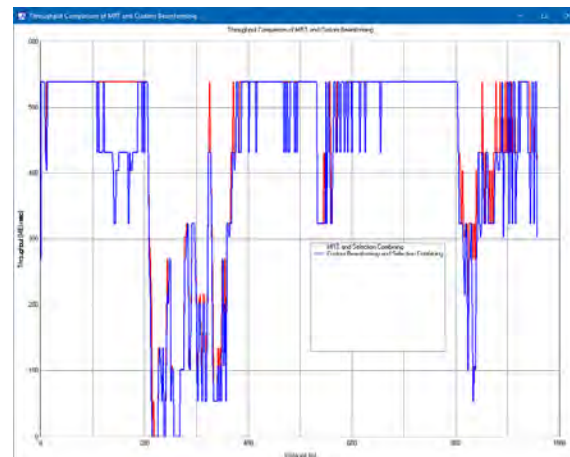


Figure 8: Comparison of throughput along the UE route from all three base stations for MRT (red) and custom beamforming (blue).

## Example 5: Throughput of a 5G New Radio FD-MIMO System in an Urban Area



Figure 9: SINR coverage for custom beamforming and selection combining.

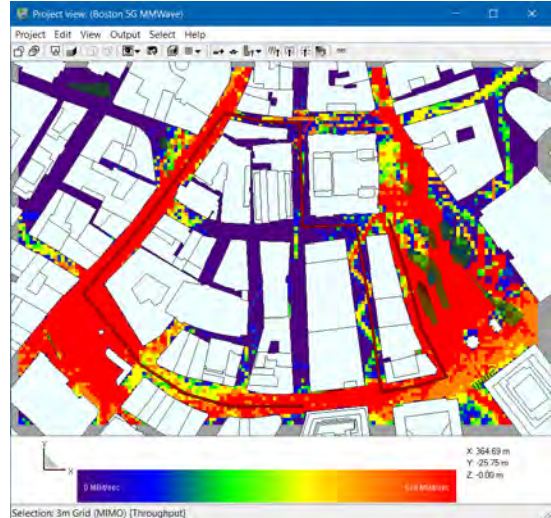


Figure 10: Throughput coverage for custom beamforming and selection combining.

## Conclusion

Wireless InSite's Communication Systems Analyzer can be used to calculate throughput, SINR and other system level quantities for realistic MIMO systems, including both transmit beamforming and receiver diversity.

This example demonstrates how a custom beamforming table can be used to model the dynamic behavior of three MIMO base stations in a section of Boston. A custom throughput table was used to model downlink data rates for 5G New Radio. Wireless InSite's X3D high fidelity ray tracing and MIMO capabilities allowed for efficient calculation of SINR and throughput.

This example also demonstrates how built-in theoretical beamforming and receiver diversity options allow quick comparison of the throughput coverage provided by custom techniques.

Remcom's Communication Systems Analyzer provides network planners and equipment designers with the tools needed to evaluate base station location and estimate the throughput in realistic scenarios. With the ability to incorporate custom beamforming and throughput rates, users have the flexibility to design and assess new equipment and network configurations.

## Example 5: Throughput of a 5G New Radio FD-MIMO System in an Urban Area

### References:

- [1] “Electrical characteristics of the surface of the earth,” Recommendation ITU-R P.527-3, 1992.
- [2] “Effects of building materials and structures on radiowave propagation above about 100 MHz,” Recommendation ITU-R P.2040-1, pp. 22–23, July 2015.
- [3] M. Weissberger, “An Initial Critical Summary of Models for Predicting the Attenuation of Radio Waves by Trees,” 1982, Electromagnetic compatibility analysis center, Annapolis, Maryland. Final report. <https://apps.dtic.mil/dtic/tr/fulltext/u2/a118343.pdf>
- [4] 3GPP TS 38.306 V15.2.0 [10] for 5G NR was used to calculate peak throughput based on the modulation order and coding rate.
- [5] G. Skidmore, “[Using Modeling and Simulation to Assess Challenges and Solutions for 5G Fixed Wireless Access.](#)”

[Request project files for this example](#)

[Click to see the web version of this example](#)

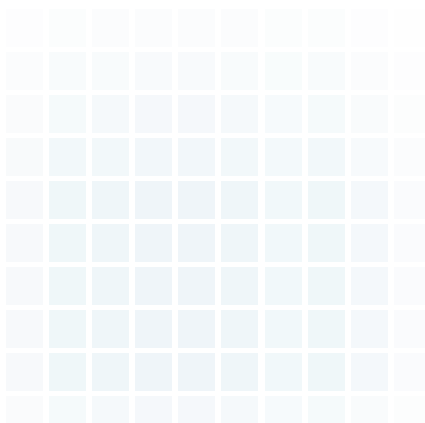


[Table of Contents](#)

## Example 6: Combined 5G/4G Antenna Analysis in a Smartphone using EM Simulation

*Summary: A proposed smartphone design that includes a 4G antenna operating at 860 MHz and a 5G array at 28 GHz is analyzed in XFDTD to determine operating characteristics and any mutual coupling. A brief study of configurations is performed to find the best positioning for each antenna.*

### Introduction

This example uses XFDTD® EM Simulation Software to analyze the performance and interaction of two antenna systems operating at 4G (860 MHz) and 5G (28 GHz) in close proximity in a smartphone design. The 4G antenna is intended to produce a broad pattern for wide coverage while the 5G array should produce narrow beams that can be steered by varying the phasing between elements. The 4G antenna is an inverted-L design and is located at the top of the phone. The 5G antenna array consists of four Yagi-Uda elements that are near the 4G antenna but offset by a conducting block. The antenna designs used in this example are from the paper [1].

### Device Geometry

The example's geometry is based on a simplified smartphone PCB. A 150x70x1 mm sheet of copper is used as the ground plane for the system with the antenna structures mounted on one end, as shown in Figure 1. The 4G antenna is placed directly over the ground plane in an inverted-L shape that has a 1x1 mm cross section and lengths of 6 mm on the short leg and 70 mm on the long leg. It is fed by a voltage source between the ground plane and the end of the short leg. The 5G array is comprised of four identical Yagi-Uda elements shown in Figure 2. The elements are mounted on a 0.3 mm thick substrate (dielectric constant = 3.6, loss tangent = 0.006) which is separated from the ground plane by a conducting block 2.2 mm thick. There is also a horizontal element of the Yagi-Uda antenna on the back side of the substrate which is visible in Figure 3. Each 5G element is fed by a Nodal Waveguide source.

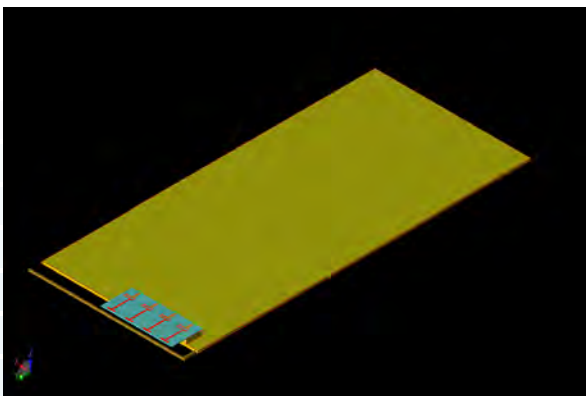


Figure 1: The smartphone design is shown in a three-dimensional CAD representation with the 4G antenna and 5G array structures visible at the left on one end of the large ground plane.

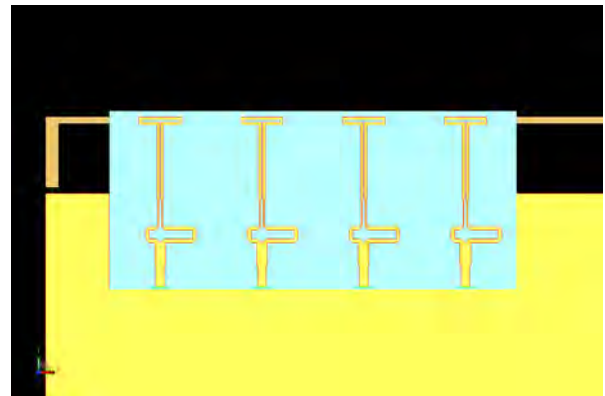


Figure 2: A CAD view of the 5G array showing the four Yagi-Uda elements on a dielectric substrate with the 4G inverted L antenna behind.

## Example 6: Combined 5G/4G Antenna Analysis in a Smartphone using EM Simulation

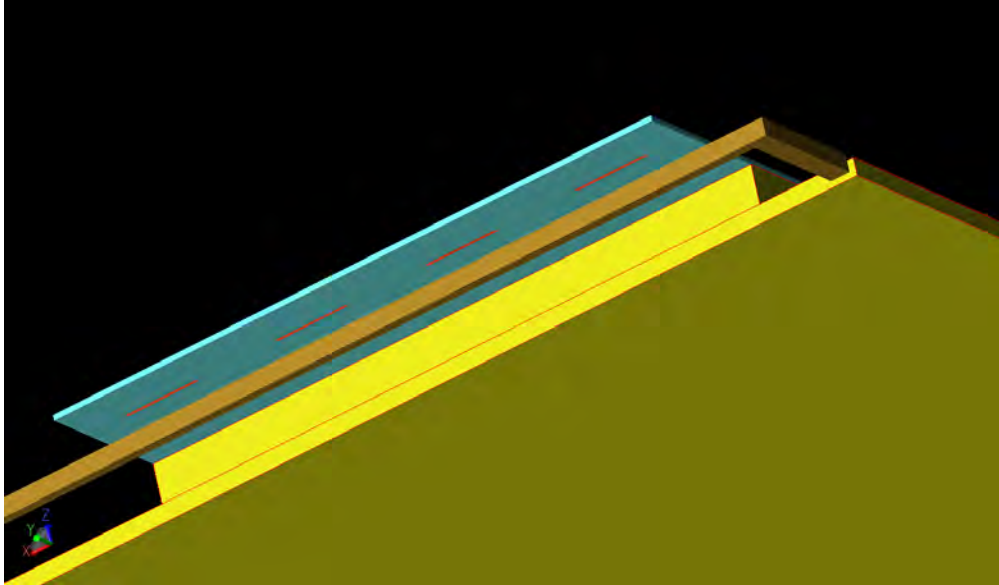


Figure 3: An underside view of the antenna array shows the separation of the 4G and 5G elements and the back side of the substrate.

The structure is meshed using the PrOGrid Project Optimized Gridding® feature of XFDTD with a base setting of 30 FDTD cells per wavelength. Minimum feature sizes are defined to ensure the substrate has five FDTD cells of thickness and the smallest conductor features are five cells across. Automatic fixed points are also applied to all parts to ensure grid lines are placed on all the edges of the geometry.

### Results

The 4G antenna is fed by a broadband source which is initially represented as a 50-ohm voltage source attached between the ground plane and the antenna base. The antenna is not a good match to the 50-ohm source resulting in poor return loss. After an initial simulation to determine the impedance of the antenna load, a matching circuit can be defined to improve the antenna performance. In this case, a lowpass-PI matching network consisting of two capacitors and an inductor is selected for use and component values are determined using analytic matching circuit calculators. The matching network components are defined in a SPICE netlist format and then imported into XFDTD as a sub-circuit as shown in Figure 4. This sub-circuit can then be added to an XFDTD voltage source as a matching circuit (Figure 5). During the execution of the program, a co-simulation of the FDTD full wave calculation and a circuit solver takes place for each time step at the cell edge containing the matching circuit. A normal full wave FDTD simulation takes place for the remainder of the calculation space. The resulting return loss plots for the unmatched and matched 4G antenna are shown in Figure 6 and the marked improvement from the matching circuit is visible. The gain of the 4G antenna is shown in Figure 7 and can be seen to provide broad coverage with a peak gain of 2.7 dBi.

## Example 6: Combined 5G/4G Antenna Analysis in a Smartphone using EM Simulation

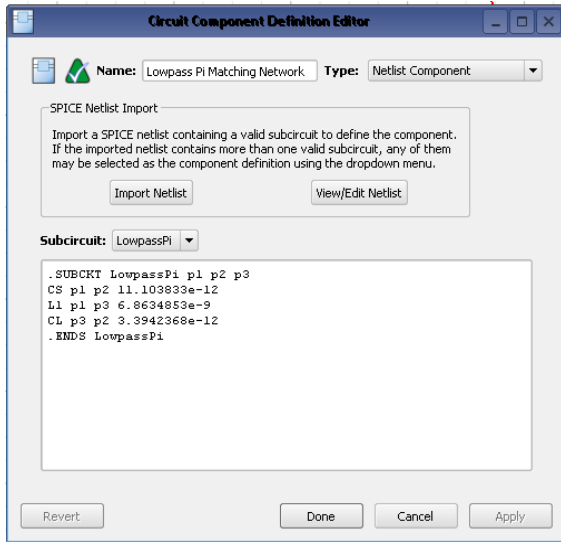


Figure 4: The menu for the netlist of the matching circuit used in the 4G antenna is shown. The netlist contains two capacitors and one inductor.

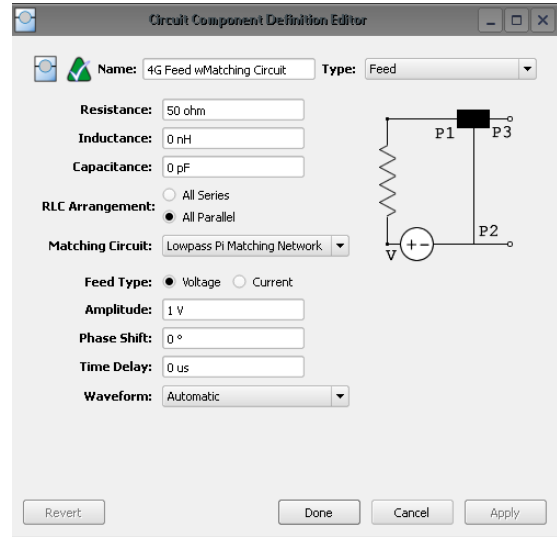


Figure 5: Shown is the voltage source menu in XFDTD for the port with the matching circuit that is used for the 4G antenna.

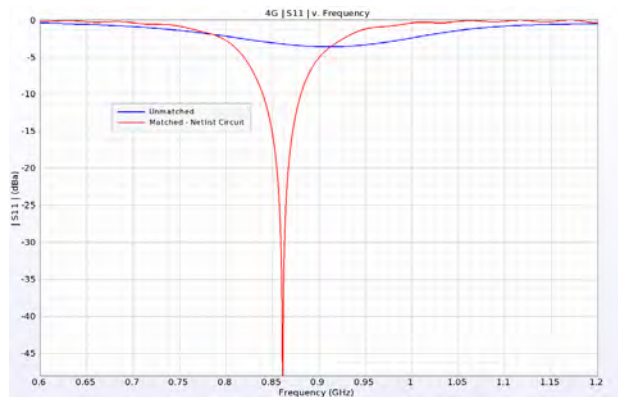


Figure 6: Return loss comparison for the unmatched and matched 4G antenna.

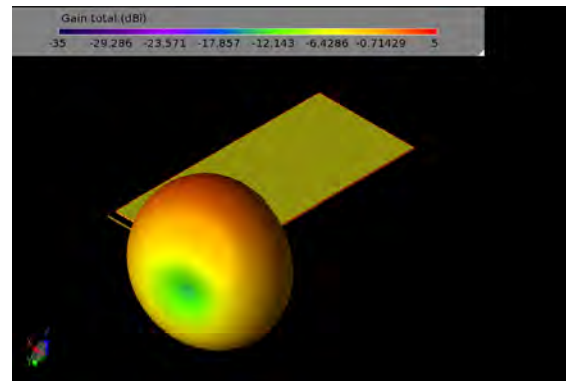


Figure 7: The 3D gain pattern of the 4G antenna shows fairly uniform coverage around the device and a peak gain of 2.7 dBi.

The orientation of the 5G antenna array relative to the 4G antenna is varied to determine the impact of the positioning on the performance of each antenna. Three configurations are considered and are shown in Figure 8: shift the 5G array so the tops of the 5G antennas are 2 mm below the top of the 4G antenna, keep the tops of the 5G and 4G antennas at the same level, or shift the 5G array up by 2 mm. In these initial cases, the phase shift between the 5G array elements is kept at zero. The impact of the offset is displayed in Figure 9 and Figure 10 where it can be seen that the offset of the 5G array down by 2 mm has a noticeable impact on the gain pattern in both the XY and YZ planes. Moving the 5G array up by 2 mm produces a pattern similar to when the 4G antenna is completely removed from the geometry. When the tops of the 4G and 5G antennas are aligned, there is a slight impact to the 5G antenna pattern. In all cases, the 4G antenna pattern is only slightly impacted, as can be seen in Figure 11.

## Example 6: Combined 5G/4G Antenna Analysis in a Smartphone using EM Simulation

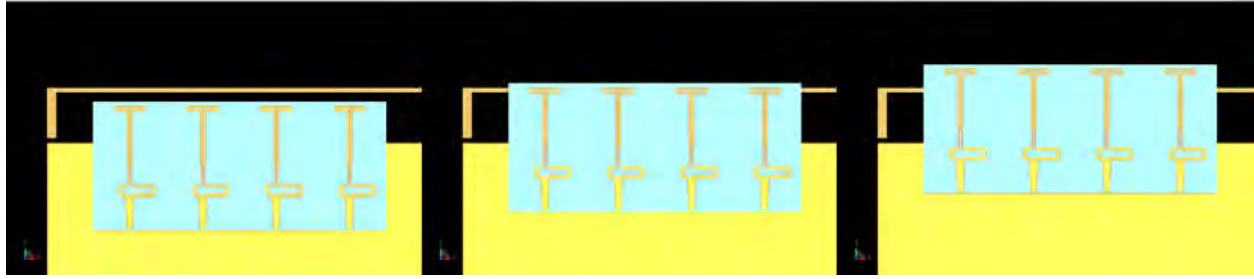


Figure 8: Three different configurations of the 5G array relative to the 4G antenna are considered (left to right): an offset of the top of the 5G antennas 2 mm below the 4G antenna, even alignment between the top of the 5G antennas and the 4G antenna, and an offset of the top of the 5G antennas of 2mm above the 4G antenna.

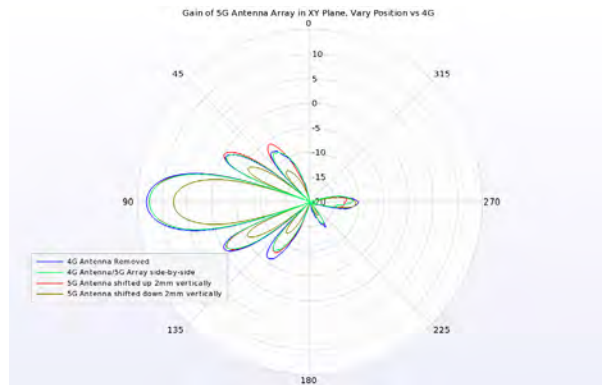


Figure 9: Plots of the gain pattern in the XY plane of the 5G array with zero phase shift between elements are shown. It can be seen that with the 5G array offset by 2 mm above the 4G antenna, the pattern is similar to when the 4G antenna is removed from the geometry. Similar patterns are found when the tops of the 4G and 5G antennas are aligned. When the 5G antennas are offset 2 mm below the 4G antenna, the 5G pattern is significantly affected.

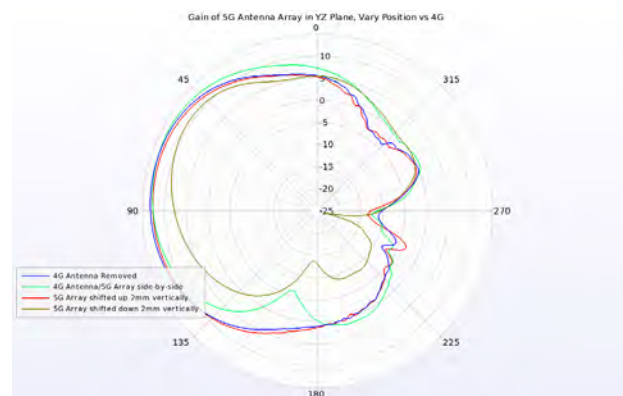


Figure 10: Plots of the gain pattern in the YZ plane of the 5G array with zero phase shift between elements show similar results for the 2mm above offset to the case of the 4G antenna removed. There is some impact on the 5G array pattern when the tops of the antennas are aligned and a larger impact when the 5G antennas are shifted 2 mm below the 4G antenna.

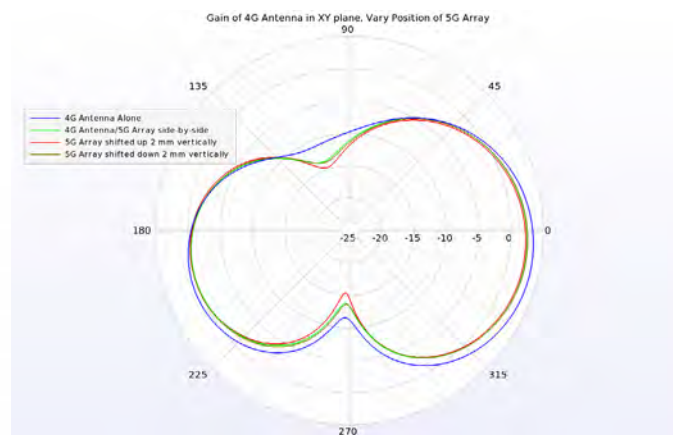


Figure 11: The gain pattern of the 4G antenna in the XY plane is only slightly impacted by the movement of the 5G antenna array.

## Example 6: Combined 5G/4G Antenna Analysis in a Smartphone using EM Simulation

Next, the 5G antenna array is fed by a 28 GHz sinusoidal source with equal amplitude and a variable phase shift across the elements for the configuration where the 5G array is positioned 2 mm above the 4G antenna. With the array fed with all elements in phase, the pattern produced has a peak gain of about 12.5 dBi with a 3 dB beamwidth of 17 degrees and a peak sidelobe level below 0 dBi (Figure 12). After applying a phase shift of 120 degrees between each element of the 5G array, the beam is scanned 24.5 degrees to one side as shown in Figure 13. Applying phase shifts of -180, -120, -60, 0, 60, and 120 degrees to the feeds produces a series of beams from the array, shown in Figure 14 where all beams are plotted at the same time.

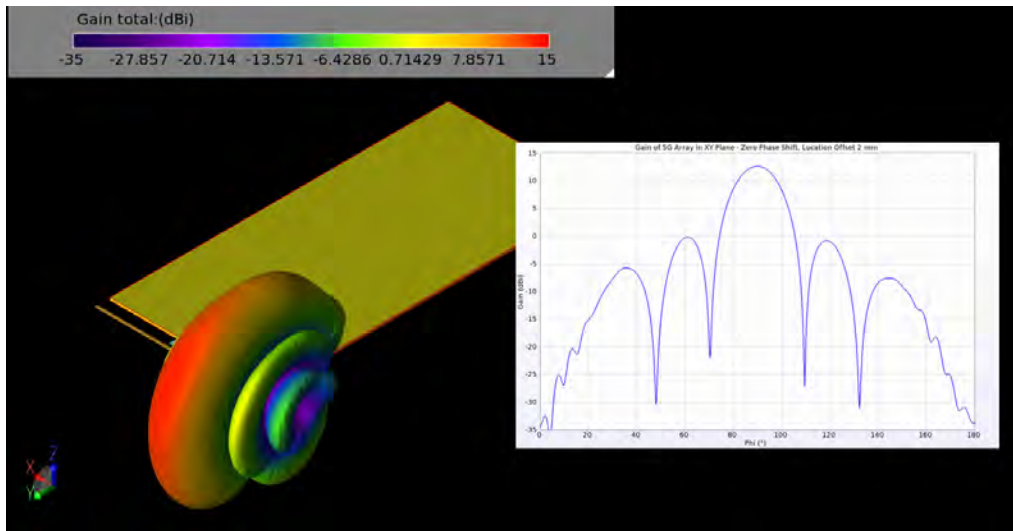


Figure 12: The gain pattern of the 5G array with zero phase shift between elements shows a beam with peak gain of 12.5 dBi and a beamwidth of 17 degrees in the XY plane.

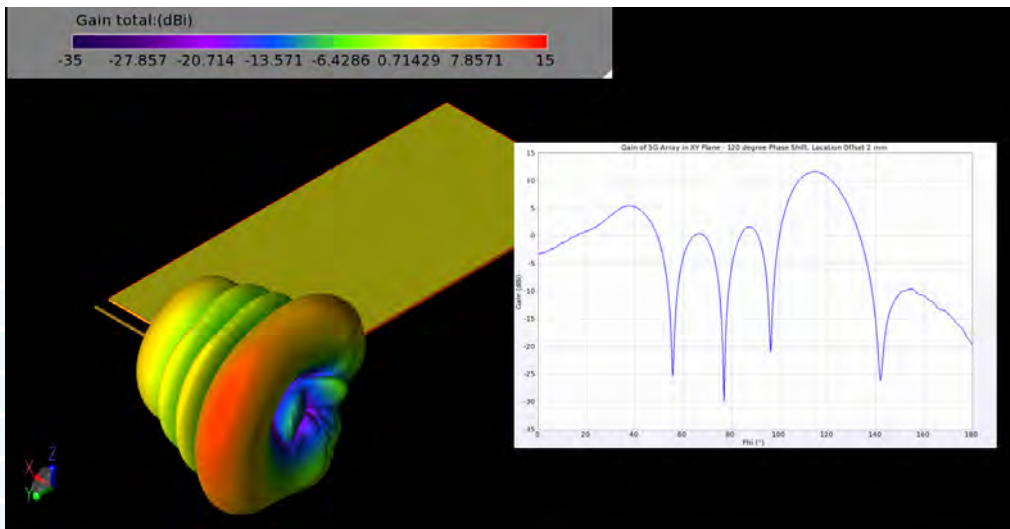


Figure 13: The gain pattern of the 5G array with a 120 degree phase shift between elements shows a beam tilted 24.5 degrees in the XY plane.

## Example 6: Combined 5G/4G Antenna Analysis in a Smartphone using EM Simulation

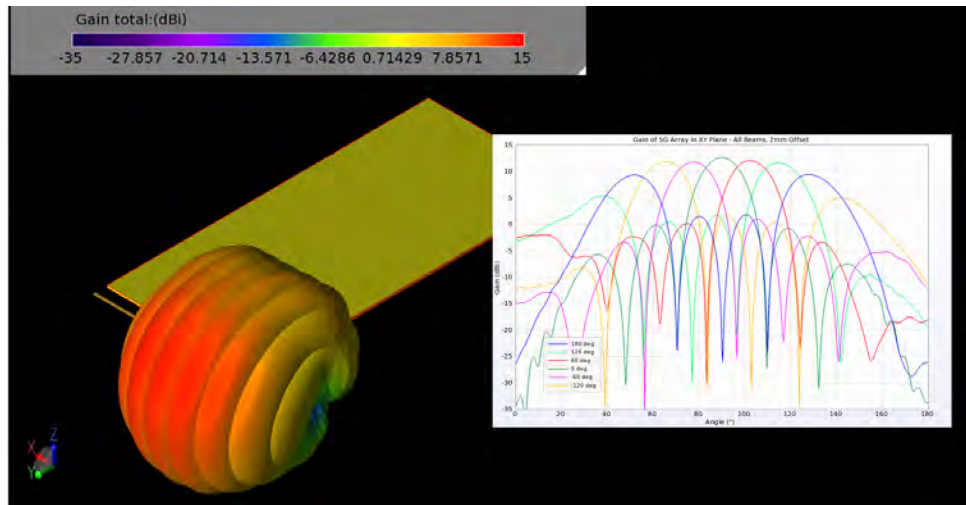


Figure 14: Six possible beams of the 5G array are shown in 3D and 2D gain patterns for the cases of a phase shift between elements of 180, 120, 60, 0, -60, and -120 degrees.

### Conclusion

A simplified smartphone device with a 4G antenna combined with a 5G array at 28 GHz is evaluated for different configurations of the 5G array relative to the 4G antenna. A best-case configuration with the 5G antenna offset 2 mm vertically relative to the 4G antenna was found with results that indicate there is nearly no interaction between the 4G and 5G elements.

### Reference:

[1] T. Yamagajo, Y. Koga, M. Kai, T. Tonooka, H. Sumi, and M. Hoshino, "A Nobel 4G and 5G Antenna Solution for Future Smartphones," IEEE Antennas and Propagation Society Int. Symp., pp. 1785-1786, 2018.

[Request project files for this example](#)

[Click to see the web version of this example](#)

Table of Contents

## Example 7: Beamforming for an 8x8 Planar Phased Patch Antenna Array

*Summary: An 8x8 planar antenna array creates narrow beams capable of scanning large sectors in front of the antenna. This example focuses on displaying typical simulation results for beams and possible plots of coverage from the full array and combinations of sub-arrays.*

### Antenna Setup

The antenna geometry consists of a 52.5 x 52.5 mm sheet of dielectric material (dielectric constant = 2.2, loss tangent 0.0009, thickness 0.254 mm) that is backed by a conducting ground plane and topped with 64 patch elements in an 8x8 configuration. Each patch is 3.4025 mm square and is spaced a half-wavelength at 28 GHz (approximately 5.36 mm) apart. A view of the patch layout on the dielectric sheet is visible in Figure 1. The feed point for each antenna is offset from the center of the patch by 0.75 mm in the horizontal direction as this was found to be the location of the best return loss result. A 28 GHz sinusoidal waveform is used at each patch with an adjustable phase offset that is determined based on the desired direction of the main beam. A widely-used formula for determining the phasing of the elements for a beam focused at a direction of  $\theta_d$ ,  $\varphi_d$  is

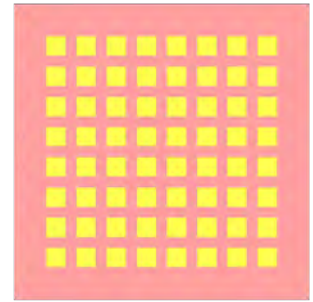


Figure 1: A top view of the antenna geometry showing the layout of the 8x8 array of patches.

$$W_n = \exp\{-j(2\pi/\lambda) \sin(\theta_d)[x_n \cos(\varphi_d) + y_n \sin(\varphi_d)]\}$$

where  $x_n$  and  $y_n$  are the locations (in meters) of the feeds at each patch referenced to the initial patch in the lower left corner of the array, and  $w_n$  is the phase shift for the element located at  $(x_n, y_n)$ . In XFDTD, these phases were assigned to each feed element through the use of parameters as shown in Figure 2, where the phase shift is defined by a parameter name.

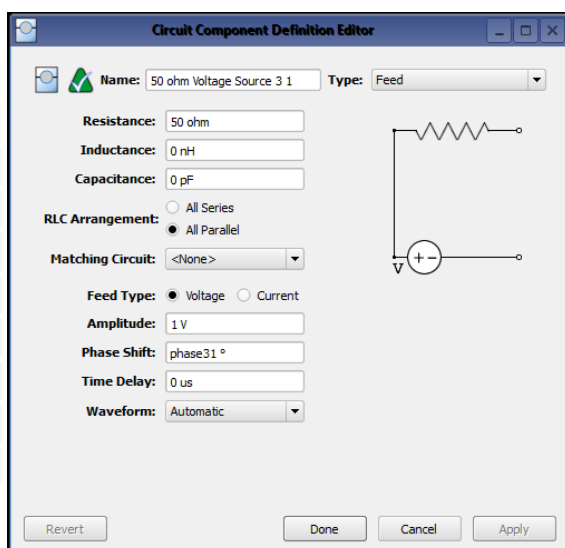


Figure 2: An example of one of the source definitions for the patch feeds, showing the phase shift set as a variable which may be adjusted depending on the desired beam direction.

## Example 7: Beamforming for an 8x8 Planar Phased Patch Antenna Array

### Results

Simulations were performed on the array to determine the gain pattern possible for different phasing conditions. An initial test set all phases equal so all elements are radiating toward the  $(0^\circ, 0^\circ)$  direction. This resulted in a maximum gain of just over 23 dBi and a 3 dB beamwidth of just over 12 degrees as shown in a line plot through one of the principal planes in Figure 3. The same pattern is shown over the CAD drawing of the antenna in three dimensions in Figure 4. With the phases adjusted to direct a beam toward  $(20^\circ, 90^\circ)$  the result is a slight drop in peak gain to 22.9 dBi and a broadening of the beamwidth to about 13.2 degrees, shown in three dimensions in Figure 5. Sweeping the beam to a corner of the array at direction  $(45^\circ, 40^\circ)$  reduces the peak gain down to 21.7 dBi and broadens the beam a moderate amount (Figure 6). As the phasing is changed to steer the beam toward the horizon, the array reaches a limit due to the patterns of the original patch antennas, and a gain plot with large side lobes forms. In Figure 7 several beam patterns are shown together to illustrate the steering of the beam from normal down to 50 degrees in 10-degree steps.



Figure 3: A line plot of the gain in a cross-sectional cut of the array pattern for the case where all patches are fed in-phase with equal amplitudes. The peak gain is just over 23 dBi and the 3 dB beamwidth is about 12 degrees.

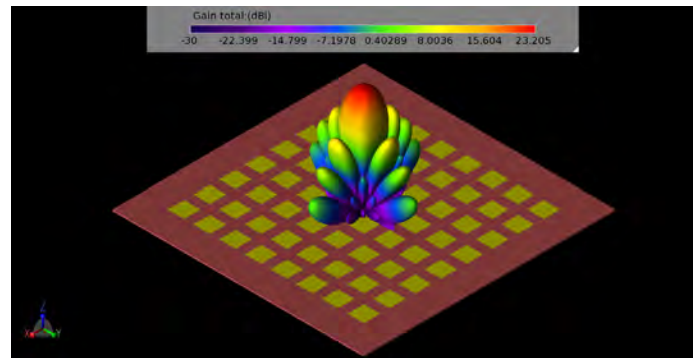


Figure 4: The three-dimensional gain pattern for the 8x8 array when all patches are fed in-phase with equal amplitudes.

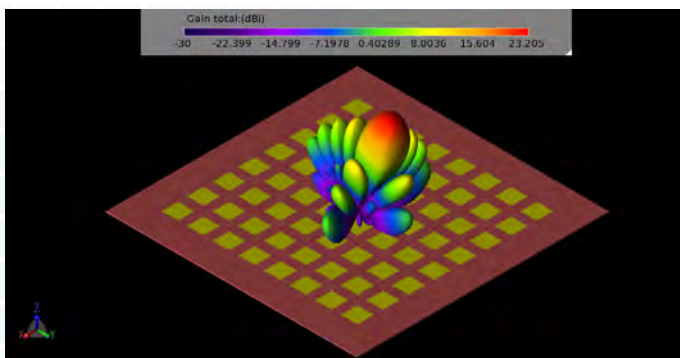


Figure 5: The three-dimensional gain pattern for the 8x8 array when the patches are phased to direct the main beam toward  $(20^\circ, 90^\circ)$ .

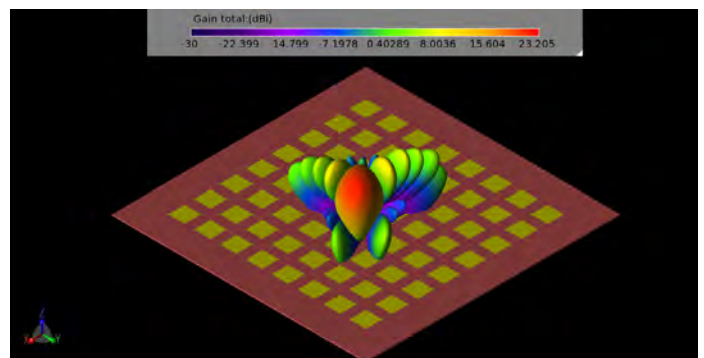


Figure 6: The three-dimensional gain pattern for the 8x8 array when the patches are phased to direct the main beam toward  $(40^\circ, 45^\circ)$ .

## Example 7: Beamforming for an 8x8 Planar Phased Patch Antenna Array

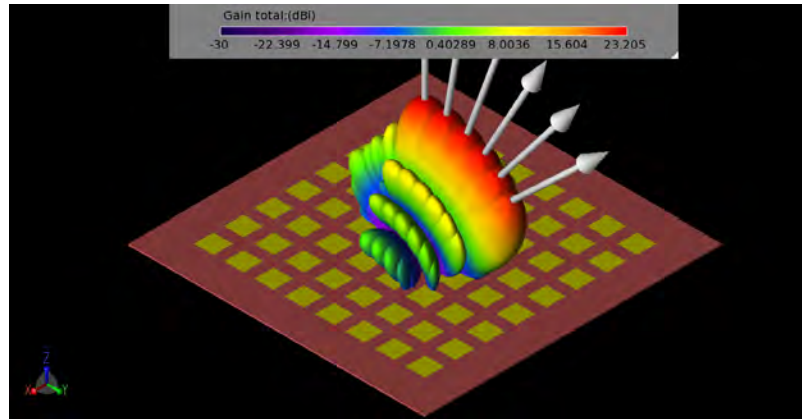


Figure 7: Three-dimensional gain patterns for six gain patterns from the 8x8 array for phasing set to direct the beam to  $(0^\circ, 90^\circ)$  to  $(50^\circ, 90^\circ)$  in 10-degree increments.

Simulations for return loss were run for each port and were found to have values below -30 dB indicating the patches were properly tuned. Radiation efficiency varied from about 78% up to more than 90% over the array, with patches near the edges of the array generally having higher efficiencies.

To examine the performance of sub-arrays, a few simple cases were simulated to find typical results for 4x4, 2x2, and 1x2 arrays of elements. All these simulations were performed with the patches fed with equal phase signals. The patterns for 4x4 and 2x2 sub-arrays in a corner of the main array are shown in Figure 8 and Figure 9. Two locations on the array, one near an edge and one near the center, were simulated as 1x2 sub-arrays and there were only minor differences in their results. A typical pattern for a 1x2 sub-array defined near the center of the main array is shown in Figure 10.

It is inefficient to simulate all possible phasing combinations to determine the overall performance of the array. However, a macro program in XFtd is available that allows a full examination of the gain levels at all angles from the array by sweeping the phasing of the individual elements. The result is a plot showing the cumulative distribution function (CDF) of the effective isotropic radiated power (EIRP).

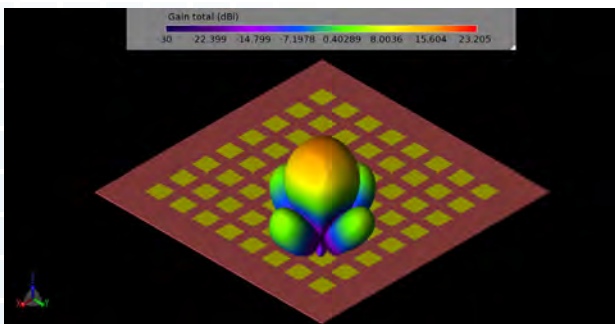


Figure 8: The three-dimensional gain pattern for a 4x4 sub-array of elements in one quadrant of the main array.

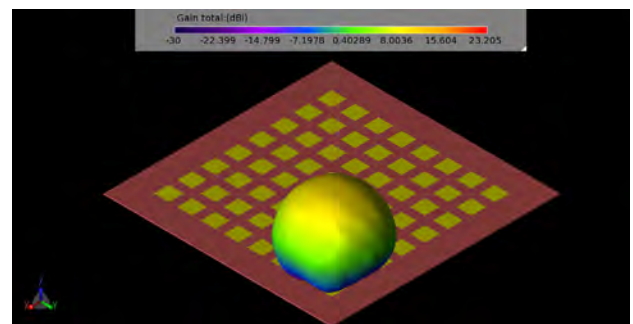


Figure 9: The three-dimensional gain pattern for a 2x2 sub-array of elements in one corner of the main array.

## Example 7: Beamforming for an 8x8 Planar Phased Patch Antenna Array

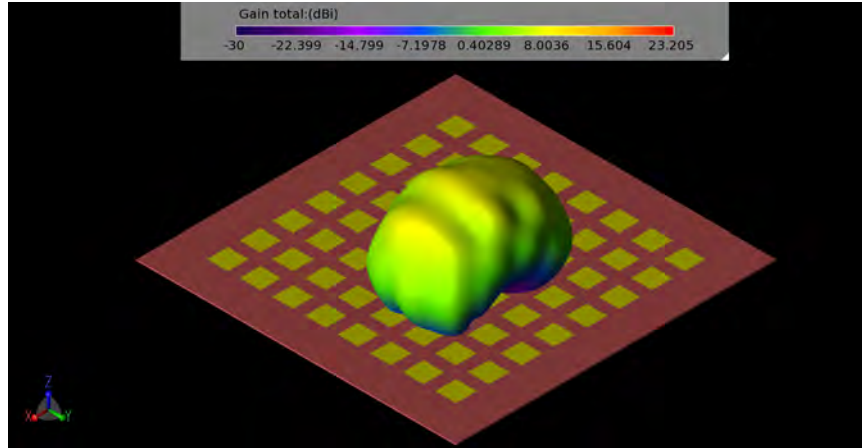


Figure 10: The three-dimensional gain pattern for a 1x2 sub-array of elements near the center of the main array.

The EIRP is an indication of the power an antenna can radiate in a given direction compared to an isotropic radiator. This plot may be used to determine the fractional area of the far-zone sphere that has gain above 0 dBi for a given input power level. Generally speaking, a power level of 23 dBmW is used as the input level for mobile devices. When the CDF for the entire 8x8 array is generated, it is found that the 23 dBmW level is about 0.225 fractional area (Figure 11), meaning that  $(1 - 0.225 = 0.775)$  77.5% of the far-zone sphere can be illuminated with gain above 0 dBi. The 4x4 sub-array (Figure 12) has 64.3% coverage at 23 dBmW input power. Similar plots are shown for the 2x2 sub-array (Figure 13, 50%), and a 1x2 sub-array near the center of the main array (Figure 14, 40.2%). Many other sub-arrays beyond those shown here are possible and may be of value depending on the needs of the system.

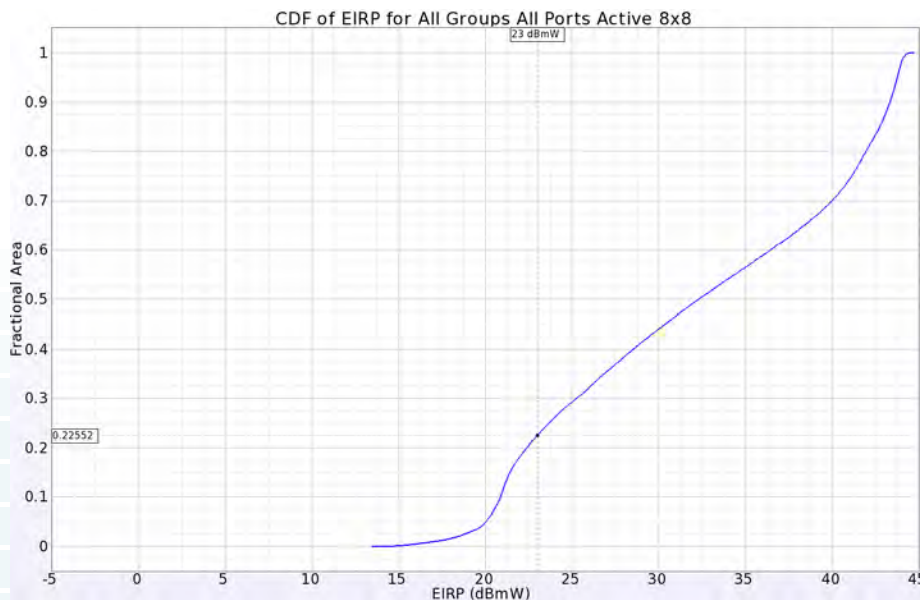


Figure 11: The CDF of EIRP plot for the full 8x8 array shows positive gain over 77.5% of the far-zone sphere for an input power of 23 dBmW.

## Example 7: Beamforming for an 8x8 Planar Phased Patch Antenna Array

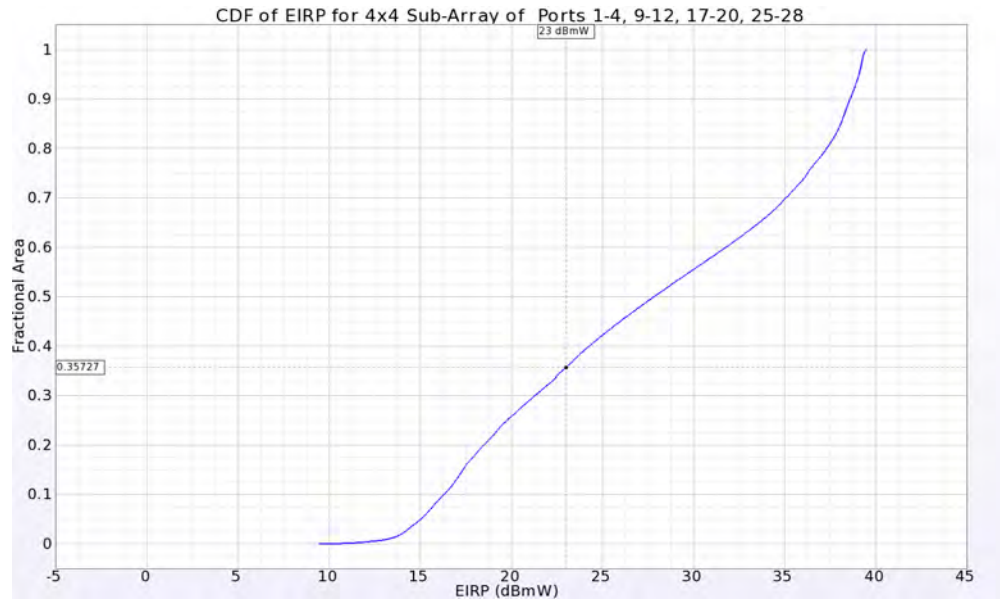


Figure 12: The CDF of EIRP plot for a 4x4 sub-array located in one quadrant of the main array showing positive gain over 64.3% of the far-zone sphere for an input power of 23 dBmW.



Figure 13: The CDF of EIRP plot for a 2x2 sub-array located in one corner of the main array showing positive gain over 50% of the far-zone sphere for an input power of 23 dBmW.

## Example 7: Beamforming for an 8x8 Planar Phased Patch Antenna Array



Figure 14: The CDF of EIRP plot for a 1x2 sub-array located in near the center of the main array showing positive gain over 40.2% of the far-zone sphere for an input power of 23 dBmW.

[Click to see the web version of this example](#)

Table of Contents

## Example 8: 28 GHz Beamforming System and Antenna Array for 5G

*Summary: This example describes a more developed 28 GHz antenna array capable of forming multiple beams for use in applications such as 5G network base stations.*

### Introduction

This example describes a more developed 28 GHz antenna array capable of forming multiple beams for use in applications such as 5G network base stations. The system consists of three parts: a Rotman lens beamformer with seven input ports and eight output ports, a series of stripline Wilkinson power dividers to split each Rotman output into eight equal signals, and an 8x8 patch antenna array. The system will create seven focused beams with 3dB beamwidth of approximately 14.5 degrees and greater than 17 dBi Fggain that cover a +/- 30 degree area.

The design process consists of three separate stages: the creation of the Rotman lens beamformer, the design of the 1 to 8 Wilkinson power divider, and the 8x8 patch antenna array. The Rotman lens is designed as a microstrip device using Remcom's [Rotman Lens Designer® \(RLD\) software](#). The power divider and the patch array are designed in [XFDTD®](#).

This example will describe the creation of each stage of the device and evaluate the performance of the individual stages and the full device.

### Device Design

The Rotman lens beamformer is desired to operate at 28 GHz and to be able to scan seven beams +/- 30 degrees through eight array ports. A 50-ohm microstrip design is chosen which uses a circular contour shape and an overall width that is just under 5 wavelengths. The sidewalls are curved and include four dummy ports per side for absorbing any reflected fields. A suitable dielectric is chosen for the substrate with a relative permittivity of 2.94 and a thickness of 0.254 mm. The basic design is shown in Figure 1 where the RLD software used to create the lens is shown.

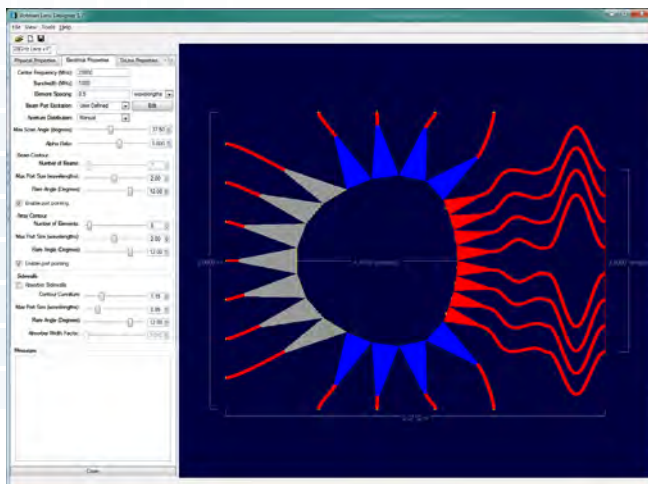


*Figure 1: The initial Rotman lens design is shown in the RLD software. The seven beam ports are at the left and the eight array ports are at the right.*

## Example 8: 28 GHz Beamforming System and Antenna Array for 5G

The beam ports (input) are at the left of the image in grey while the array ports (output) are at the right in red. The output ports at the ends of the transmission lines are spaced a half-wavelength apart. The transmission lines are of varying lengths as determined by the equations of the Rotman lens. The Rotman lens is generally used with one or more beam ports active to produce a linear phase shift across the array ports due to the time delay in the signal propagation to reach the output. These devices are often referred to as “true time delay” systems and do not rely on phase shifters to steer beams.

Following tuning of the lens shape, the seven output beams, one per input port, are plotted in Figure 2 to verify the position of the beams and the sidelobe levels. The beams are present at  $\pm 30$ ,  $\pm 20$ ,  $\pm 10$  and 0 degrees of scan angle. A uniform aperture distribution array ports is intended.

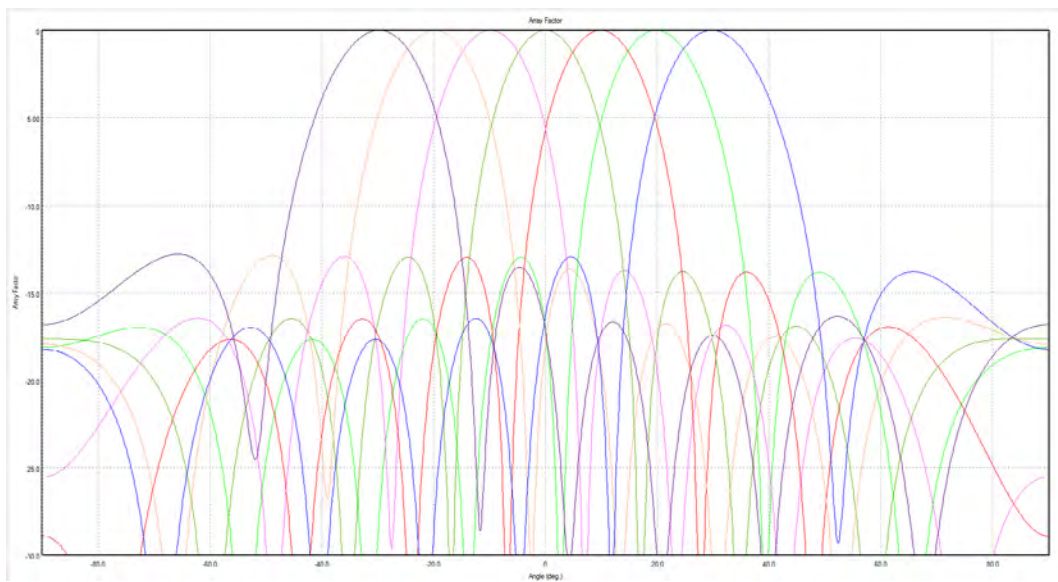


*Figure 2: The Array Factor, a measure of the expected radiation pattern produced by a beam port due to the phase across the array ports, is shown for all seven beams of the Rotman lens designed in RLD.*

The Rotman lens design from RLD was exported into an SAT format CAD file for use in XFDTD. Following importation into XFDTD, the resulting geometry of Figure 3 was developed where all ports are terminated with a 50-ohm load. The return loss for each beam port was computed as shown in Figure 4 where acceptable values below -10 dB are found at 28 GHz. Via a script in XFDTD, the output complex voltages across the transmission lines connected to the array ports are used to compute the beam pattern for each input port which are shown in Figure 5. As can be seen, these are quite similar to the beams from the original RLD design.

## Example 8: 28 GHz Beamforming System and Antenna Array for 5G

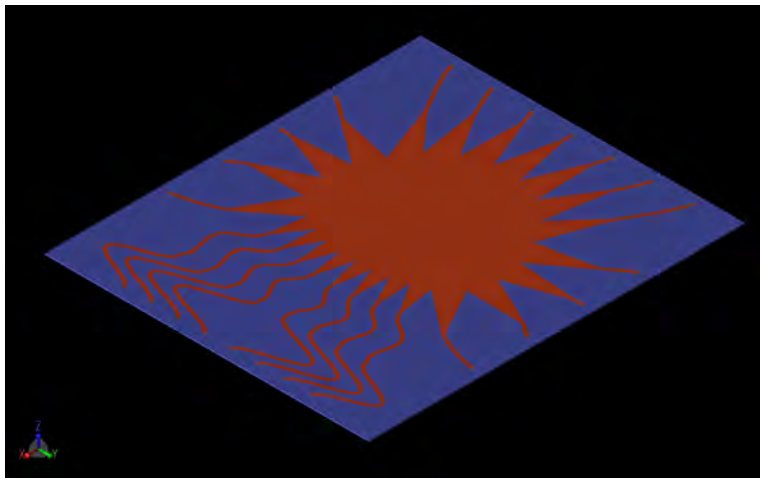


Figure 3: The Rotman lens design is shown in XFDTD following importation of a CAD file that was generated by the RLD software program. The lens is done in microstrip on a 0.254 mm substrate with permittivity of 2.94.

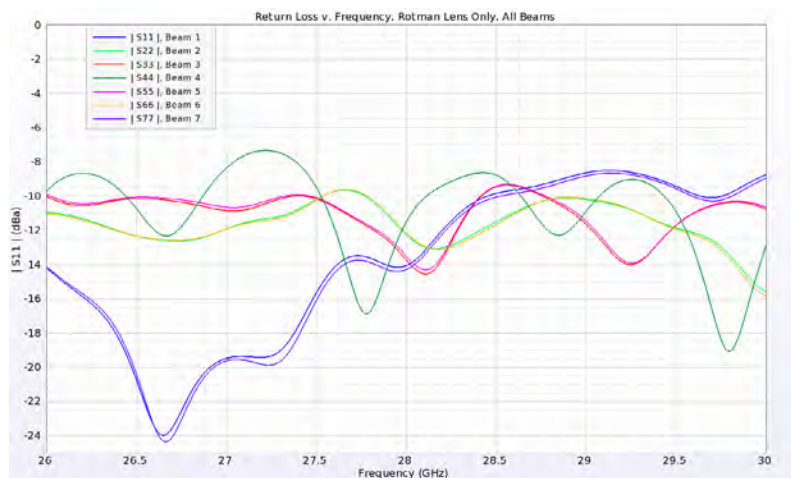


Figure 4: The return loss for each beam port of the Rotman lens is plotted over a frequency range around 28 GHz.

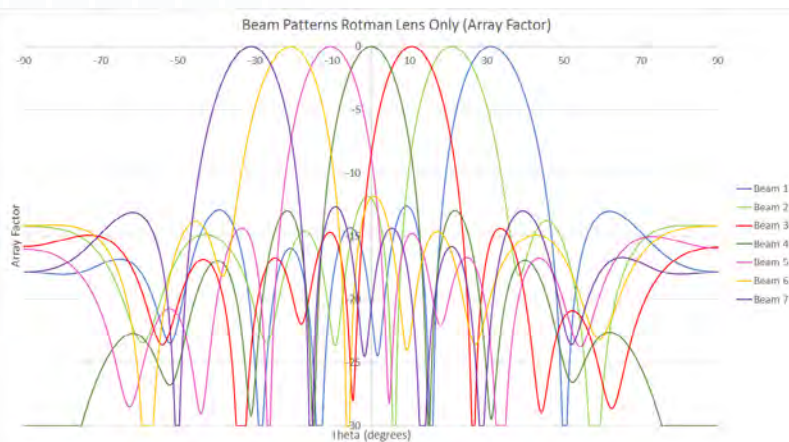


Figure 5: This figure shows the Array Factor for the Rotman lens as simulated by XFDTD. The complex voltage at the terminal end of each transmission line connected to the array ports was used to produce the Array Factor for each input port, and it can be seen that these beam patterns are very similar to those from RLD shown in Figure 2.

## Example 8: 28 GHz Beamforming System and Antenna Array for 5G

An analysis of the S-parameter data across the array ports shows that the magnitude has variations from -11 to -15 dB which are slightly more significant than the desired uniform distribution (Figure 6). The phase variations across the array ports show near linear variations, as desired, for each of the seven beams (Figure 7). In Figure 7 the phase is adjusted to put zero phase on array port 4 for comparison. The phase variation resulting from the Rotman lens between array ports is  $\pm 90$ ,  $\pm 60$ ,  $\pm 30$ , and 0 degrees for the seven beams.

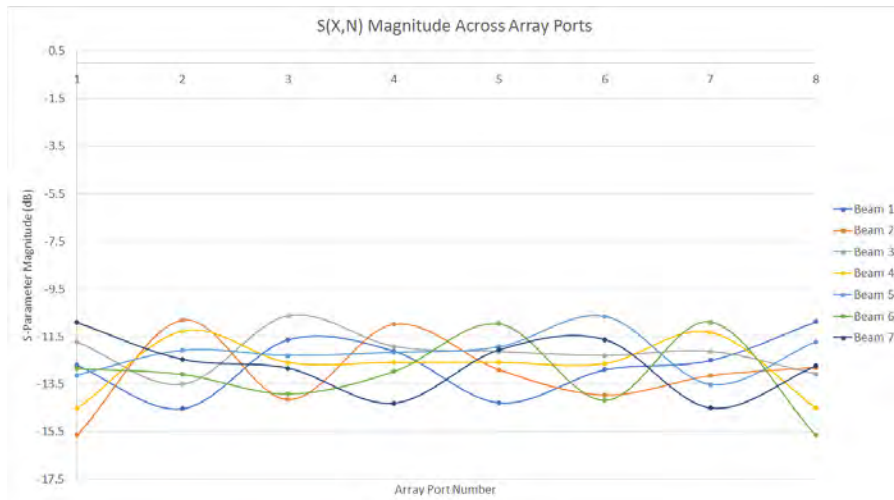


Figure 6: A uniform distribution across the array ports of the Rotman lens was desired in the design. In the XFDTD simulation, it can be seen that there is some variation in the actual distribution.

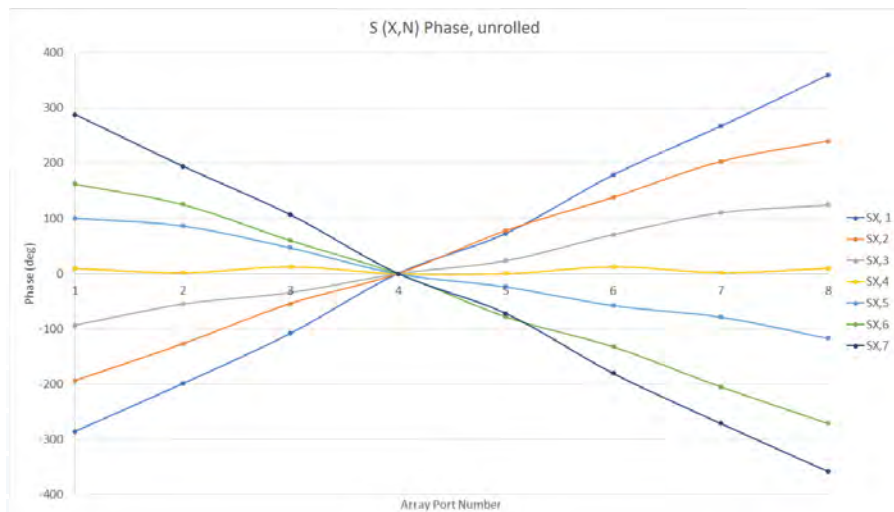


Figure 7: The phase variation across the array ports is plotted for each input beam port. The expected phase for the designed system should be linear with a slope ranging from  $+90$  degrees between output ports to 0 degrees to  $-90$  degrees depending on which input port is active. Here the phase variations can be seen to be nearly linear with slopes close to the desired values.

## Example 8: 28 GHz Beamforming System and Antenna Array for 5G

The stripline Wilkinson power divider is designed using the same dielectric ( $\epsilon = 2.94$ ) as for the Rotman lens. The thickness of the stripline substrate is 0.508 mm and the traces are 50 ohms. The design splits one input into eight equal and in-phase outputs in three stages. The output of each port of the Wilkinson is connected via a short coaxial cable to the input of a patch antenna. The patch antenna array consists of eight 1x8 subarrays where each subarray is connected to one Wilkinson. The patch array has a substrate of the same dielectric with 0.254 mm thickness. The patches are spaced a half-wavelength (at 28 GHz) apart and are tuned for best performance with a patch size slightly larger than a quarter wavelength and a feed offset by 0.9 mm from the center of the patch. The combined Wilkinson-Array parts are shown in Figures 8 and 9.

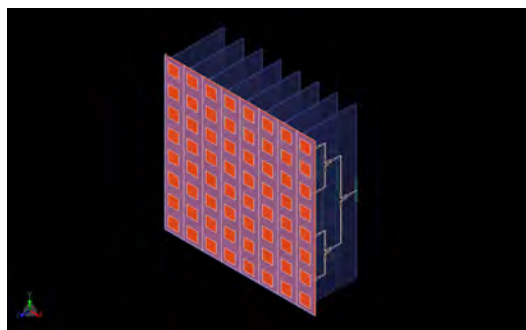


Figure 8: Shown in the figure is the three-dimensional CAD representation of the 8x8 patch antenna array and the eight Wilkinson power dividers that attach to the antennas. Here the Rotman lens has been replaced by eight input waveguide ports on the first stage of the Wilkinson power dividers.

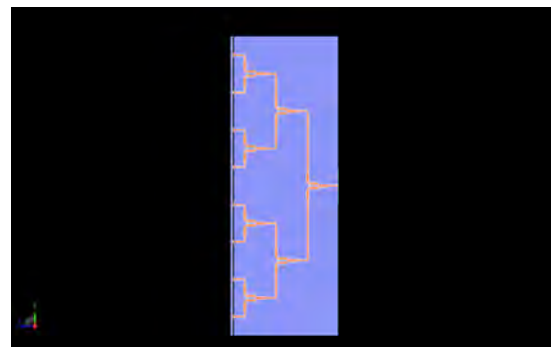


Figure 9: A side view of the Wilkinson power divider is shown which clearly displays the three stages of dividing the signal.

The combined Wilkinson-Array part was simulated with waveguide ports added to each of the eight Wilkinson inputs. The resulting return loss plots for each subarray are shown in Figure 10 and good performance is seen at 28 GHz. The ports are fed with phase shifts varying from +90 degrees between elements (beam 1) to -90 degrees between elements (beam 7) in 30 degree increments to produce seven distinct beams. The beam patterns (plotted as gain rather than Array Factor) are shown in Figure 11. In Figure 11 there is some slight variation in the peak gain, but the beam locations are well distributed at the desired angles which are a close match to the original RLD design. Figures 12 and 13 show the beams in three dimensions along side the geometry structure. The large white arrows indicate the direction of peak gain.

## Example 8: 28 GHz Beamforming System and Antenna Array for 5G

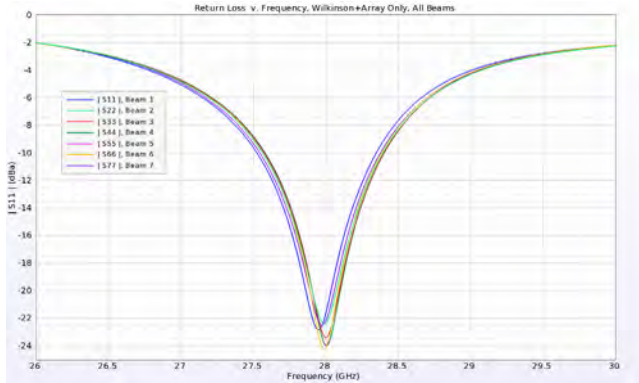


Figure 10: The return loss for each of the eight ports attached to the Wilkinson power dividers shows good performance at 28 GHz. There is only slight variation between the different 1x8 subarrays attached to each power divider.

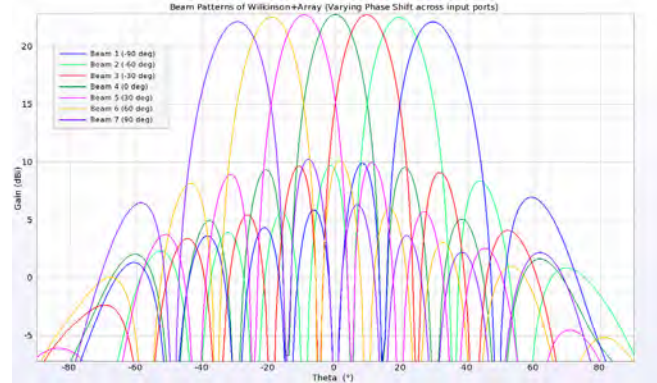


Figure 11: The beam patterns for the combined Wilkinson and antenna array are plotted as gain (rather than Array Factor) for the device of Figure 8. Here the phase relationships that would be produced by the Rotman lens have been replaced by phase shifts across the input ports attached to the Wilkinson power dividers. The beams can be seen to be in the correct angular position with nearly equal gain.

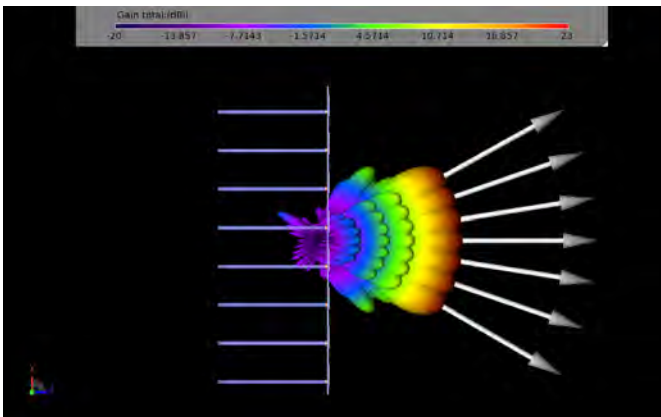


Figure 12: This figure shows the seven beams as a three-dimensional pattern rather than a line plot like Figure 11. The large white arrows depict the direction of the peak gain for each beam.

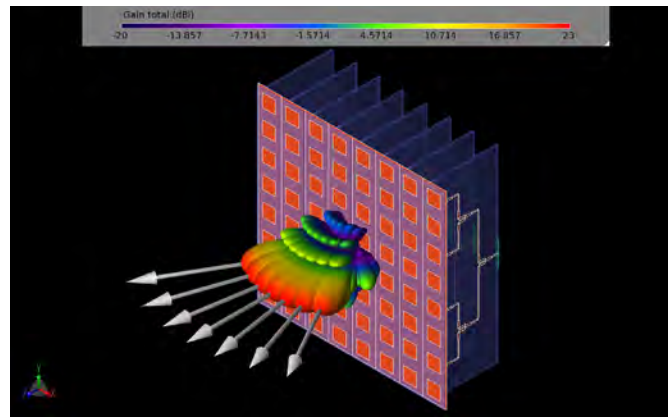


Figure 13: This is an alternate view of the three-dimensional beam patterns of the seven beams generated by the array.

The final step of the design is to combine the Rotman lens beamformer with the power divider/antenna array. This structure is shown as a three-dimensional CAD model in Figures 14, 15, and 16. Here, waveguide ports matched to 50 ohms are used at all open connections including the seven beam ports and eight dummy ports for reflection reduction in the lens.

## Example 8: 28 GHz Beamforming System and Antenna Array for 5G

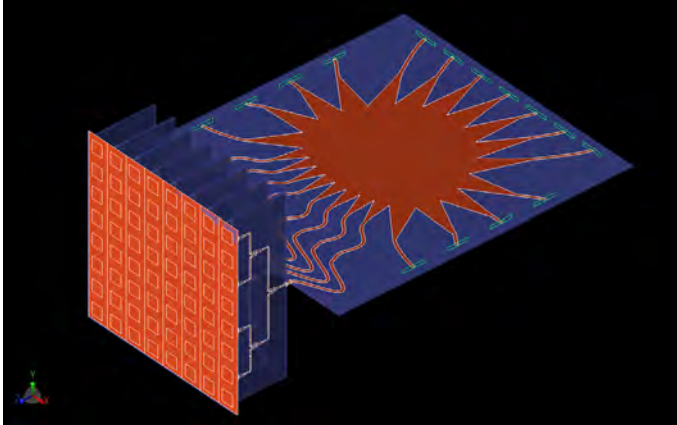


Figure 14: Here the complete system of the Rotman lens input, Wilkinson power divider stage, and 8x8 patch antenna array are shown as a three-dimensional CAD model.

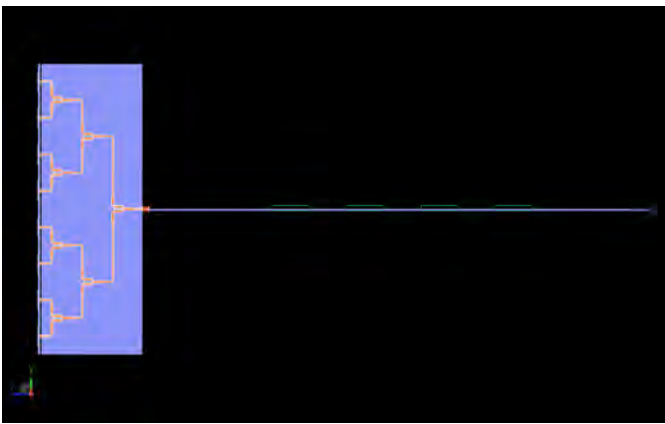


Figure 15: This is a side view of the entire system where the three stage Wilkinson power divider is more clearly visible.

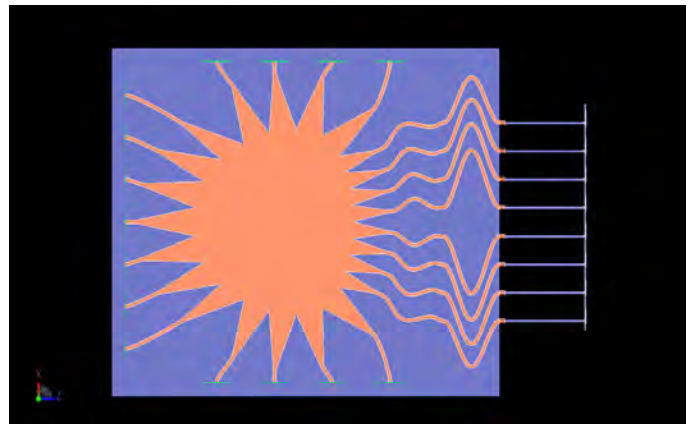


Figure 16: This is a top view of the entire system where the Rotman lens and array transmission lines are more clearly visible.

Following simulations with a broad band pulse at each beam port input, a plot of the return loss versus frequency is shown in Figure 17. The return loss for all ports is good and near -16 dB with the exception of the central port (beam 4) which has a higher return loss, perhaps due to the symmetrical location and reflections that are not well absorbed in the dummy ports.

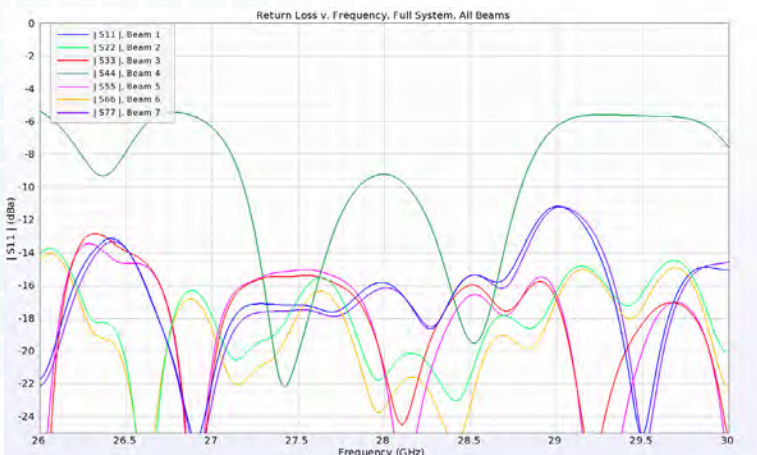


Figure 17: Plotted here is the return loss from each of the seven input ports of the Rotman lens when connected to the entire system of power dividers and antennas. The results are generally good with values below -10 dB for all ports except the center beam (port 4) which has some mismatch likely due to reflections not well absorbed by the sidewalls.

## Example 8: 28 GHz Beamforming System and Antenna Array for 5G

The beam patterns at 28 GHz for the full device are shown in Figure 18 and can be seen to be properly located in angle with somewhat higher variations in peak gain compared to the simulations of the array without the Rotman lens. This is due to the less-than-perfect phase and magnitude variations across the Rotman lens array ports that feed the Wilkinson power divider. The results are consistent with the previous beam patterns generated in earlier simulations shown in Figures 2, 5, and 11 despite showing more variation in the beam magnitudes.

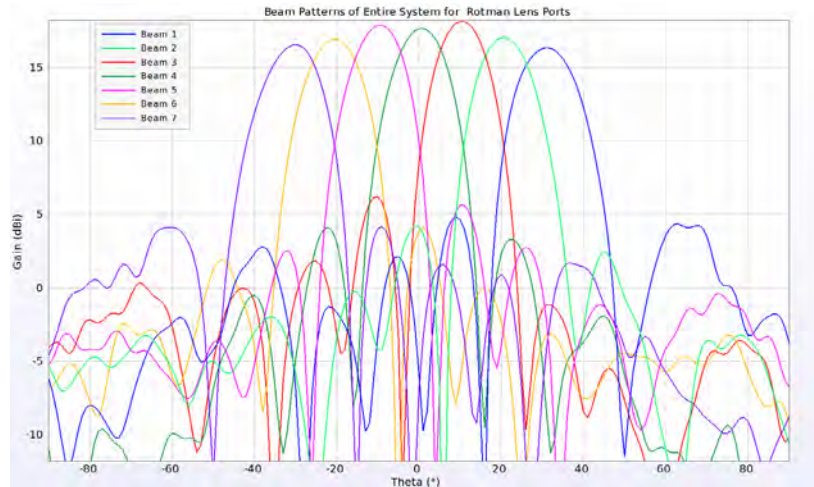


Figure 18: The resulting beams from the entire system are plotted as gain patterns and can be seen to be similar to the other beam pattern plots, with beams spaced 10 degrees apart from -30 to 30 degrees and near equal magnitude.

Three-dimensional views of the beams give a clearer image of the performance of the device including the presence of sidelobes and their levels. In Figures 19, 20, 21, and 22, the first four beams of the device are shown in relation to the device structure. Beams five, six and seven would be similar to three, two and one, respectively. In Figure 23, all seven beams are displayed in three dimensions to show the full range of coverage of the device. Figure 24 shows the same seven beams from a different viewing direction located above the device along the Y axis.

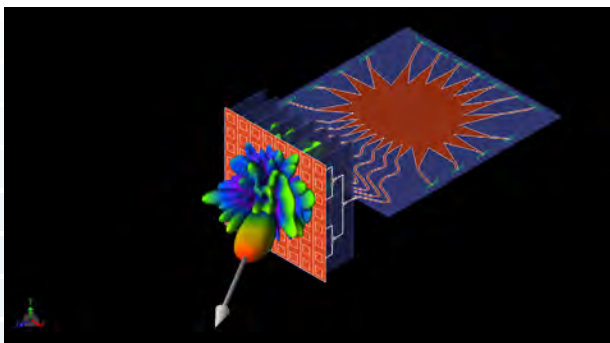


Figure 19: Shown in this figure is a three-dimension view of the beam pattern from input port 1 of the Rotman lens generated by the entire system.

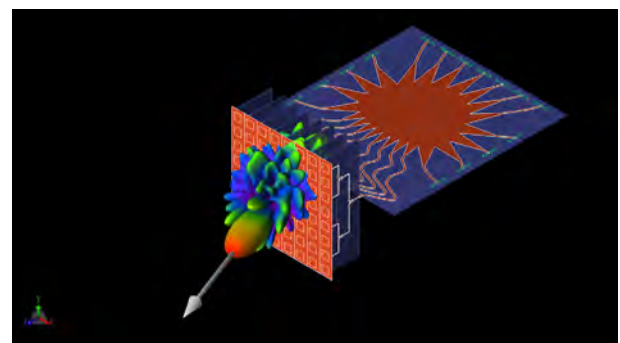


Figure 20: Shown in this figure is a three-dimension view of the beam pattern from input port 2 of the Rotman lens generated by the entire system.

## Example 8: 28 GHz Beamforming System and Antenna Array for 5G

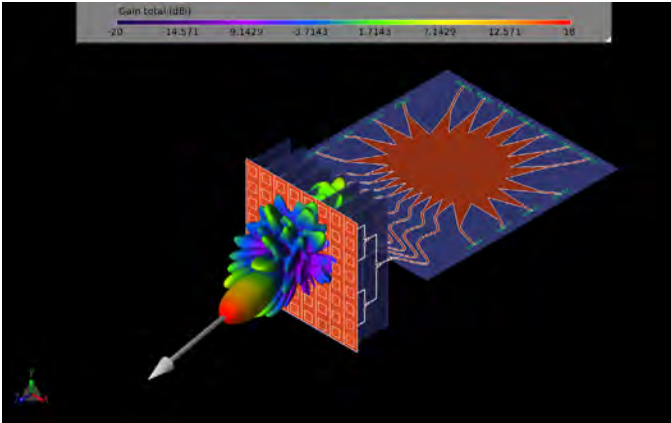


Figure 21: Shown in this figure is a three-dimension view of the beam pattern from input port 3 of the Rotman lens generated by the entire system.

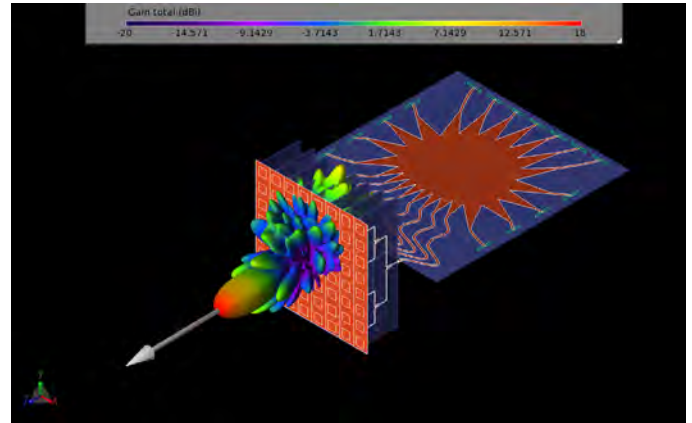


Figure 22: Shown in this figure is a three-dimension view of the beam pattern from input port 4 of the Rotman lens generated by the entire system.

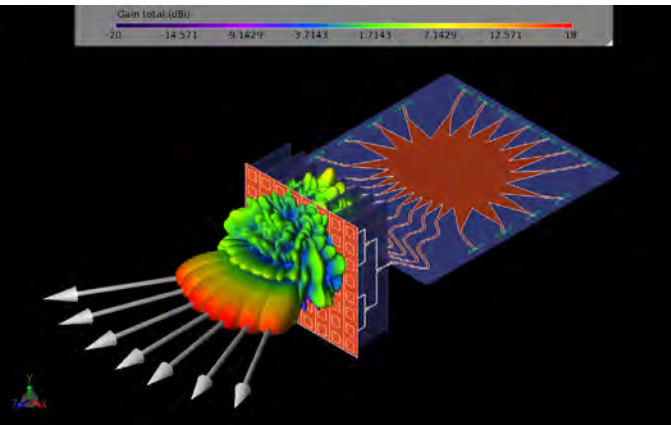


Figure 23: This figure shows all seven beams of the entire system as three-dimensional gain patterns.

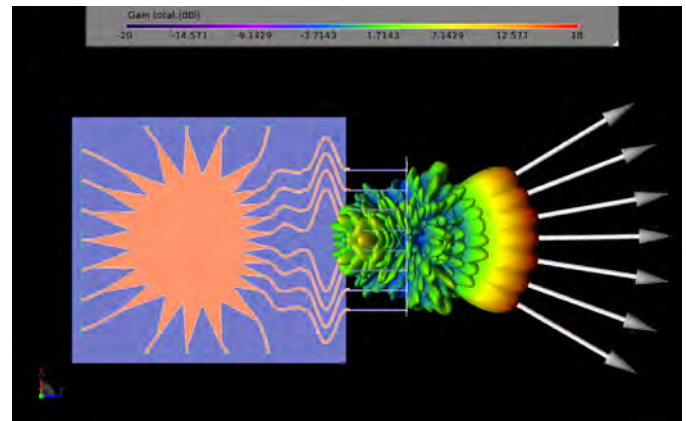


Figure 24: The seven beams generated by each input port of the Rotman lens are shown in three dimensions from a top view.

The visualization of the propagation of conduction currents on the device is a useful tool for ensuring that all connections between stages are good (no unconnected parts) and that the propagation speed to the arrays is the same. It is important for the transmission lines from the Rotman lens to the power dividers be the correct lengths to maintain the phase relationship of the wave front. In Figure 25, the current is seen propagating from the center beam port across the lens. By Figure 26 the current has just reached the output of the array ports and is entering the transmission lines. Figure 27 shows the current fully through the transmission lines and entering the power dividers. In Figure 28, the geometry display is disabled to better visualize the currents as they propagate through the first power divider stage and are still in good phase relation. Finally, in Figure 29 the currents have just reached the feeds of the patch antennas and are still in phase with each other.

## Example 8: 28 GHz Beamforming System and Antenna Array for 5G

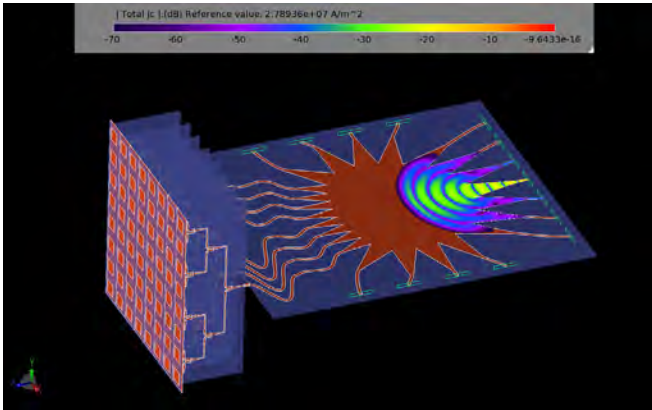


Figure 25: This figure shows the propagation of conduction currents from beam port 4 into the Rotman lens.

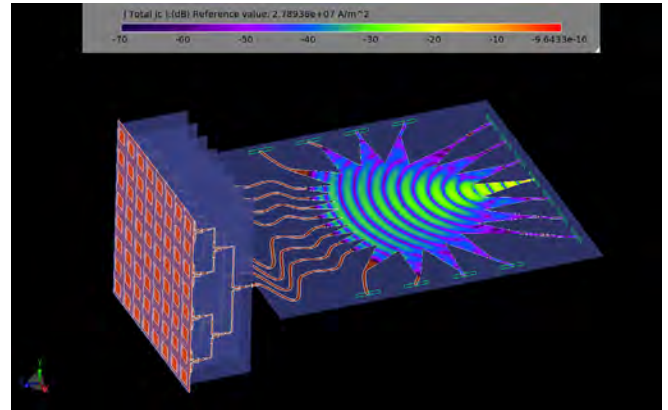


Figure 26: In this figure, the propagation of conduction currents from beam port 4 of the Rotman lens has just reached the array ports of the lens.

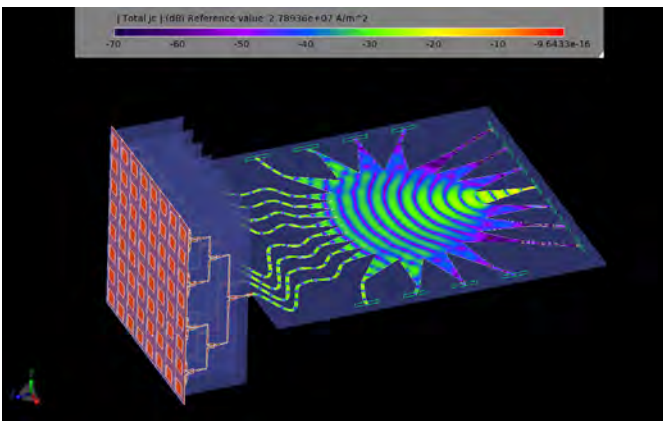


Figure 27: The propagation of the conduction currents has reached the ends of the array transmission lines and is entering the Wilkinson power divider elements. All currents appear to be in phase as they are arriving at the same location at the same time.

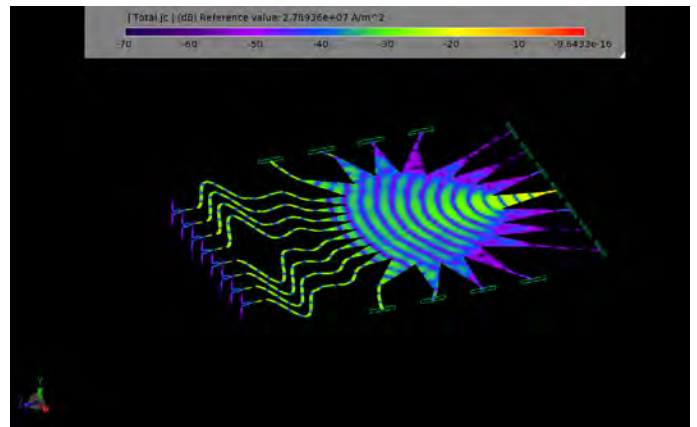


Figure 28: Here the display of the geometry has been disabled and only the conduction currents on the metal surfaces are shown. The fields are beginning to split in the first stage of the Wilkinson power divider.

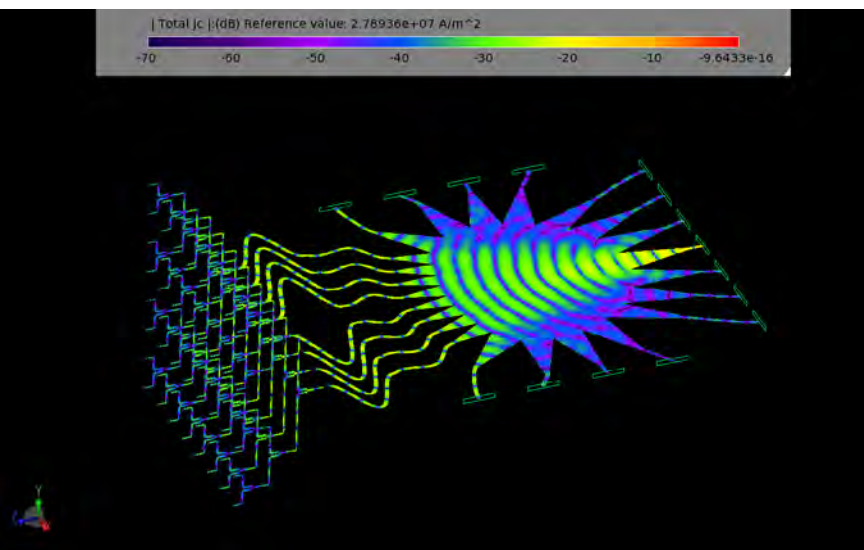


Figure 29: The currents have finally propagated across the entire structure and have reached the input ports of the antennas.

## Example 8: 28 GHz Beamforming System and Antenna Array for 5G

### Conclusion

This example demonstrates one process for generating and analyzing a 28 GHz steerable array for 5G applications. Here the requirements were for beam coverage from -30 to 30 degrees in seven beams which was realized using a Rotman lens beamformer, eight 1 to 8 Wilkinson power dividers, and an 8x8 array of patch antennas.

[Click to see the web version of this example](#)

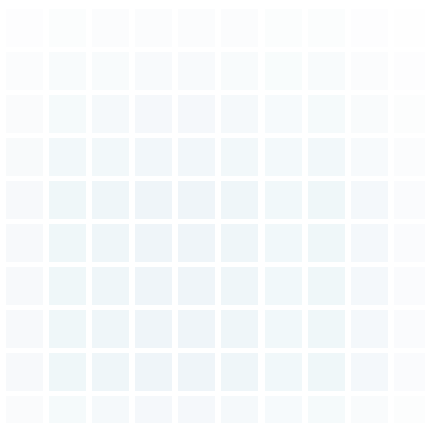


Table of Contents

## Example 9: 5G Antenna Array Simulation for mmWave Wireless Virtual Reality Headsets

*Summary: A 60 GHz antenna array design is simulated in XFDTD to demonstrate suitability for use on wireless Virtual Reality headsets. The antenna array is comprised of elements each containing two patches and a parasitic element. The resulting array produces a fan beam which may be steered by varying the phasing between the elements resulting in broad coverage. The final design is simulated mounted on a section of a virtual reality visor.*

### Introduction

This example demonstrates an antenna array for 5G 60 GHz applications of wireless communication for wearable devices such as virtual reality headsets. The antenna design for this example is from the paper [1] by Hong and Choi of Hanyang University. The array is composed of four elements which each have two patches and a parasitic element. The parasitic element aids in producing a wider beam in one dimension to give better coverage. The beams may be steered by varying the phase shift between elements to provide near hemispherical coverage.

### Device Design and Simulation

The proposed array design is shown in Figure 1 where the red material represents the substrate (Taconic TLY, relative permittivity of 2.2 and loss tangent of 0.0009) and the green material is Copper. The bottom layer of the antenna is the substrate with a ground plane underneath. This layer is topped by 50-ohm feed lines which then go through impedance matching before reaching the first patch, then a 70-ohm line connects to the second patch. Those patch elements are covered by another substrate layer which is topped by parasitic elements that are perpendicular to the 70-ohm lines. The second layer is visible in the three-dimensional view of the structure in Figure 2. The elements are spaced a half wavelength apart and are fed by Nodal Waveguide ports with variable phase.

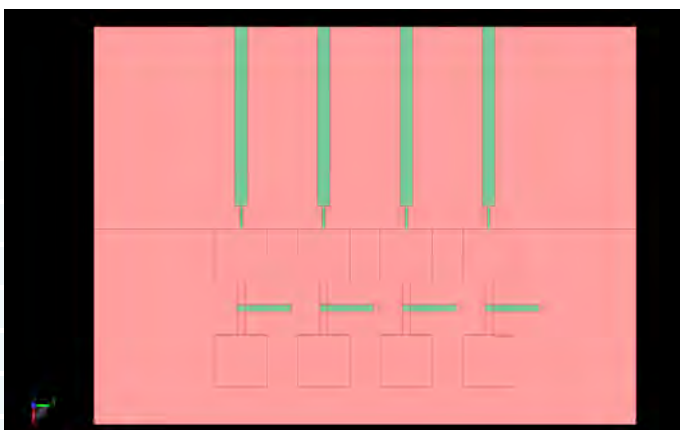


Figure 1: Shown is a top view of the antenna array with the substrate layers shown in red and the metal feed lines and parasitic elements in green. The patches are shown as outlines because they are covered by a second substrate layer.

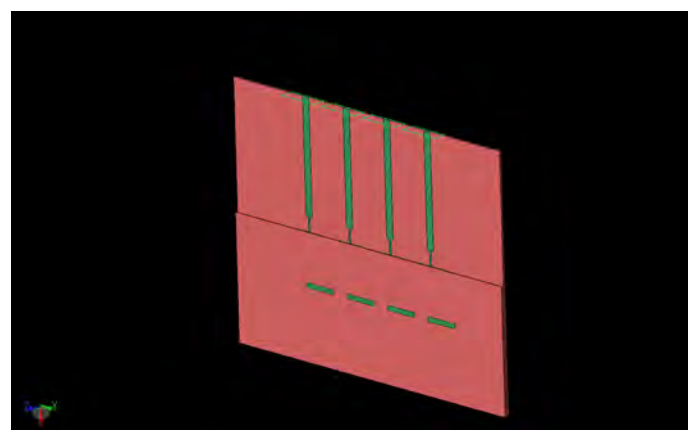


Figure 2: The antenna array is shown in three dimensions with the edge of the top substrate layer more visible over the patches. The four nodal waveguide feed ports are visible on the top of the array.

## Example 9: 5G Antenna Array Simulation for mmWave Wireless Virtual Reality Headsets

Initially the antenna array is simulated alone for return loss and gain pattern analysis. For computing S-parameters, each port is simulated individually with the others terminated in a 50-ohm load. The resulting return loss for each port is shown in Figure 3 and the response from each port is quite similar to the others. The simulations are also performed without the parasitic elements to demonstrate the impact of including them on the return loss. As can be seen in Figure 3, the parasitic elements shift the resonance of the antenna higher in frequency and reduce the depth of the S11 null. When the antenna is simulated with all ports active and in phase, the broadside gain pattern is computed as shown in Figure 4. Here it can be seen that without the parasitic element the pattern has deep nulls around +/- 40 degrees which are undesirable. By including the parasitic elements, the nulls are reduced and the array produces a wide fan beam. This beam is better shown in three dimensions in Figure 5 where the pattern can be seen to be broad in the vertical direction and narrow (3-dB beam width of 24 degrees) in the horizontal direction.

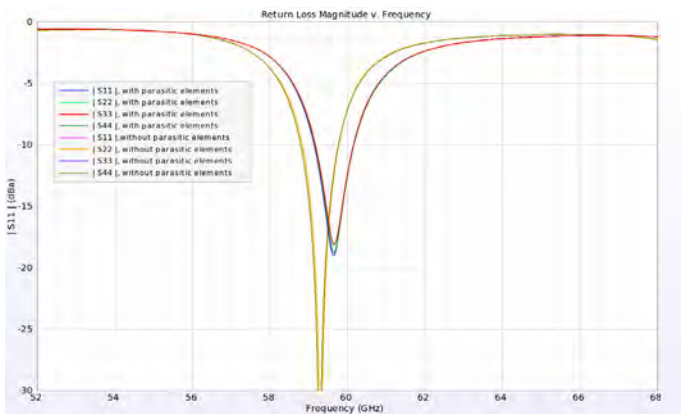


Figure 3: The return loss for each element of the array is quite similar. The addition of the parasitic element shifts the response higher in frequency and reduces the null depth.

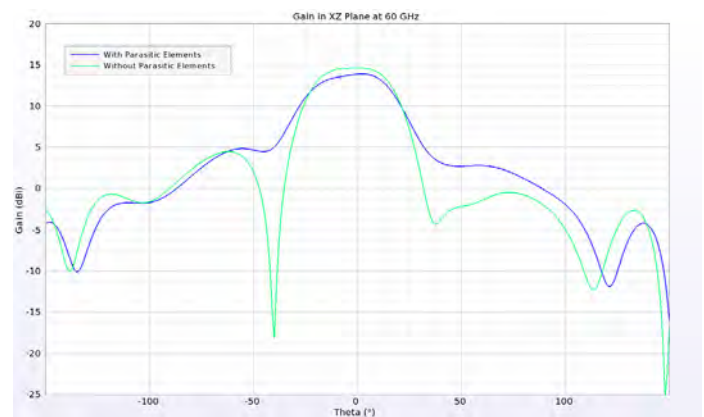


Figure 4: The gain pattern broadside of the array is fairly wide with the parasitic elements included. Without the parasitic elements there are undesired nulls present in the pattern.

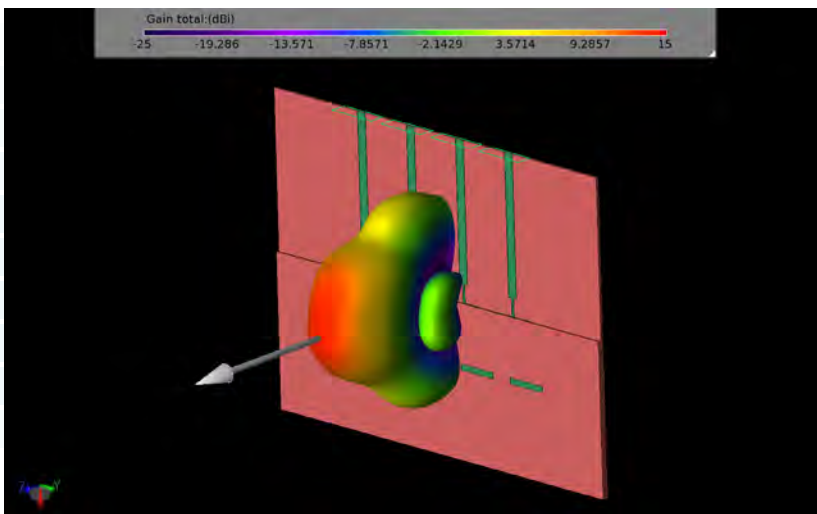


Figure 5: The three-dimensional gain pattern for the equal phase case shows peak gain to the side with a fan shaped pattern.

## Example 9: 5G Antenna Array Simulation for mmWave Wireless Virtual Reality Headsets

Beam steering is possible with this array by varying the phasing between the elements. In Figure 6, the array is shown with a beam steered about 30 degrees in the horizontal by applying a phase shift of 90 degrees between the elements. In Figure 7, seven possible beams are shown by varying the phase shift from -90 to 90 in 30-degree steps.

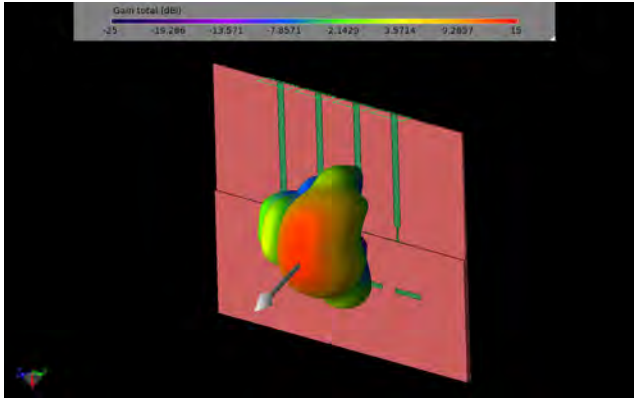


Figure 6: With a phase shift of 90 degrees between the antenna elements the beam shifts about 30 degrees to the side.

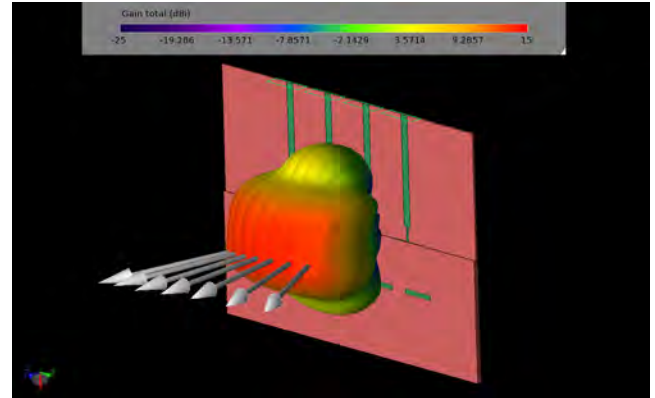


Figure 7: Sweeping the phase shift from -90 to 90 degrees in 30 degree increments generates seven beams that cover a broad area.

The antenna array is next mounted on a virtual reality headset on a phantom head to demonstrate a possible application, shown in Figure 8. Due to the very large size of the head at 60 GHz, a portion of the total problem space, shown in Figure 9, is actually simulated for this demonstration. In Figure 10 the primary beam of the array (all elements in phase) is shown compared to the headset and phantom. When a phase shift of 90 degrees is applied between the elements, the beam shifts to one side by about 30 degrees as shown in Figure 11. Figure 12 demonstrates both beams at the same time.

The dissipated power on the surface of the phantom is also of interest in these applications, and it can be computed by [XFDTD](#). In Figure 13, the dissipated power from the headset-mounted array on the evaluated surface of the phantom model is shown.

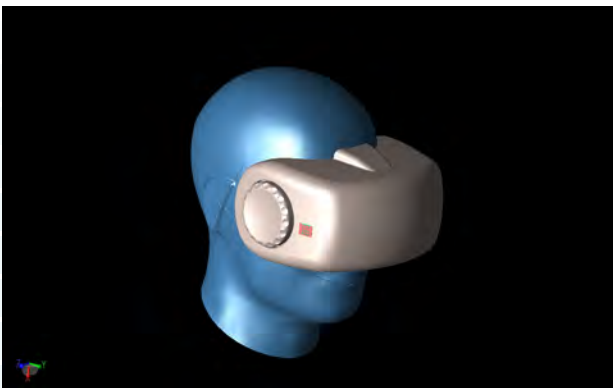


Figure 8: The antenna array is shown mounted on a virtual reality headset. The headset is attached to a phantom head model.

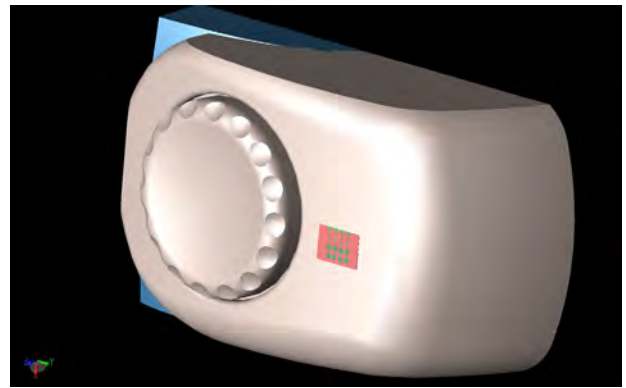


Figure 9: Due to the large size of the problem space, a section of the headset/head model is used for the actual simulations.

## Example 9: 5G Antenna Array Simulation for mmWave Wireless Virtual Reality Headsets

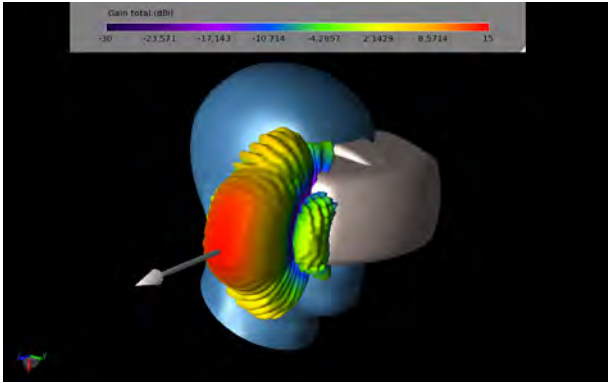


Figure 10: The computed gain pattern for the case of all elements in phase is shown with a strong gain of nearly 15 dBi and a fan-shaped beam.

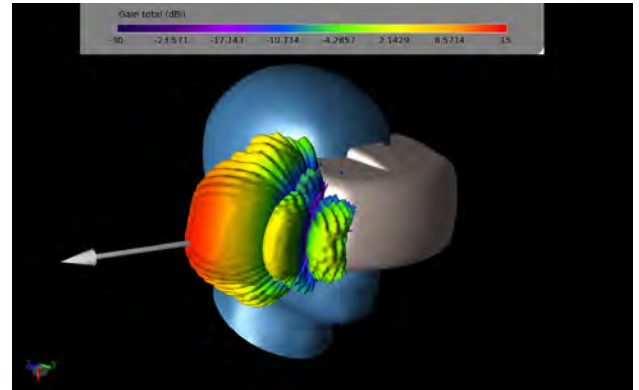


Figure 11: After applying a 90-degree phase shift between the elements the beam is shifted about 30 degrees to the side.

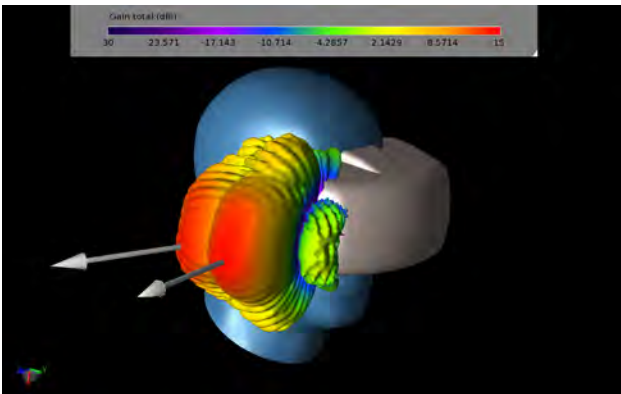


Figure 12: Both beams with 0- and 90-degree phase shifts are shown in this image.

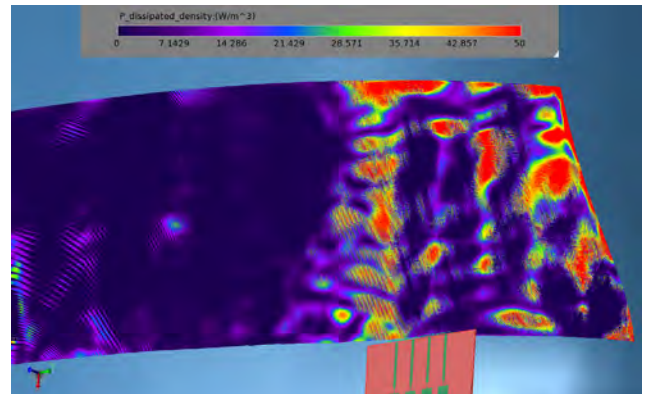


Figure 13: The dissipated power on the surface of the head phantom from the radiating array is computed by the software and displayed.

### Reference:

- [1] Y. Hong and J. Choi, "60 GHz Array Antenna for mm-Wave 5G Wearable Applications," 2018 IEEE International Symposium on Antennas and Propagation and UNSC/URSI National Radio Science Meeting, pp. 1207-1208, 2018.

[Click to see the web version of this example...](#)

[Request a free trial...](#)

[Request project files...](#)

[Table of Contents](#)

# Contact Remcom



**sales@remcom.com**  
**www.remcom.com/contact**



**<https://www.facebook.com/remcomsoftware/>**



**<https://twitter.com/remcomsoftware>**



**<https://www.linkedin.com/company/remcom-inc>**



**<https://www.youtube.com/user/remcomsoftware/>**

Visit **www.remcom.com** for more information

Remcom, Inc.  
315 S. Allen St., Suite 416  
State College, PA 16801 USA

+1.888.7.REMCOM (US/CAN)  
+1.814.861.1299 phone  
+1.814.861.1308 fax

**sales@remcom.com**